The Influence of Hydrophobic Mismatch on Structure and Dynamics of Transmembrane Helices and Lipid Bilayers

By

Taehoon Kim

Submitted to the graduate degree program in Bioinformatics
and the Graduate Faculty of the University of Kansas
in partial fulfillment of the requirements for the degree of
Doctor of Philosophy.

_____
Chairperson: Wonpil Im, Ph. D.

_____
Eric Deeds, Ph. D.

_____
John Karanicolas, Ph. D.

_____
Krzysztof Kuczera, Ph. D.

_____
Ilya Vakser, Ph. D.

Date Defended: 10/28/2011

The Dissertation Committee for **Taehoon Kim**

certifies that this is the approved version of the following dissertation:

The Influence of Hydrophobic Mismatch on Structure and Dynamics of Transmembrane Helices and Lipid Bilayers

_____

Chairperson: Wonpil Im, Ph. D.

Date approved: 10/28/2011

Abstract

Membrane proteins with one or a few transmembrane (TM) helices are abundant and often involved in important TM-included signaling and regulation through formation of hetero- and homo-oligomers. Especially, solid-state NMR (SSNMR) is a powerful technique to describe the orientations of membrane proteins and peptides in their native membrane bilayer environments. However, it is still challenging to obtain the structural information of membrane protein. Since protein-lipid interaction and bilayer regulation of membrane protein functions are largely controlled by the hydrophobic match between the TM domain of membrane proteins and the surrounding lipid bilayer, the interplay between the structure and the energetics of lipid and protein components of biomembranes is one of long-standing interests in biophysics. Structural and dynamic changes of the TM helices in response to a hydrophobic mismatch as well as molecular forces governing such changes remain to be fully understood at the atomic level.

In this dissertation, to systematically characterize responses of a TM helix and lipid adaptations to a hydrophobic mismatch, I have performed a total of 5.8-μs umbrella sampling simulations and calculated the potentials of mean force (PMFs) as a function of TM helix tilt angle under various mismatch conditions. Single-pass TM peptides called WALP were used in two lipid bilayers with different hydrophobic thicknesses to consider hydrophobic mismatch caused by either the TM length or the bilayer thickness.

The deuterium (^{2}H) quadrupolar splitting (DQS), one of the SSNMR observables,

has been used to characterize the orientations of various single-pass TM helices using a semi-static rigid-body model such as the geometric analysis of labeled alanine (GALA) method. However, dynamic information of these TM helices, which could be related to important biological function, can be missing or misinterpreted with the semi-static model. The result in Chapter 3 demonstrates that SSNMR ensemble dynamics provides a means to extract orientational and dynamic information of TM helices from their SSNMR observables and to explain the discrepancy between molecular dynamics simulation and GALA-based interpretation of DQS data.

Finally, this dissertation describes the influence of hydrophobic mismatch on structure and dynamics of TM helices and lipid bilayers through molecular dynamics simulation of Gramicidin A (gA) channel in various lipid bilayers. The structure and dynamics of the gA channel as well as important lipid properties were investigated to address the influence by various hydrophobic mismatch conditions.

It is with pride that I dedicated this thesis to my wife Juwon and my parents; without them this thesis would not exist.

Acknowledgements

First and foremost, it was a great pleasure to do my Ph.D. study under the guidance of Prof. Wonpil Im. I would like to sincerely appreciate Prof. Wonpil Im for providing me with the knowledge and skills to be complete my research, teaching me how to approach scientific questions, and inspiring me as a scientist as well as an independent researcher. He has been a great mentor, a great source of guidance, and a wonderful collaborator. I deeply appreciate his patience and encouragement regarding my scientific view and skills as well as his constant and kind support to my family for past 5 years.

I want to thank my former advisor Prof. Youndgo Won, who inspired me to become a scientist. It was he who taught me the way to be a scientist. Also, he gave me a chance as a research assistant during my undergraduate study.

I would also like to express my gratitude to my graduate committee, consisting of Dr. Ilya Vakser, Dr. John Karanicolas, Dr. Eric Deeds, and Dr. Krzysztof Kuczera for careful reading of this thesis and useful comments. I am also grateful to Dr. Jang Zhang and Dr. Gennady Verkhivker for helpful comments on my pre-doctoral examination.

The work presented in the chapters below would not have been possible without the help of a number of coauthors and collaborators. I would next like to thank to Dr. Jinhyuk Lee for initial effort on free energy simulation (Chapter 2). He has done an excellent job in providing me the computational skills and techniques. Without his help, I

couldn't finish this project. Also, he gave me a lot of help at the beginning of Ph.D. study. Dr. Roger E. Koeppe II (University of Arkansas) gave me helpful comment for SSNMR-ED project (Chapter 3). Sunhwan Jo in Im's group implemented SSNMR-ED in CHARMM. He gave me a lot of help in computational skill and gave me valuable advices. There are also many people who helped on the gramicidin A project (Chapter 4). Special thanks to Dr. Olaf S. Andersen (Cornell University) for giving me a chance to explore a new world of Gramicidin A. Dr. Richard W. Pastor (NIH/NHLBI) and Dr. Jeffery B. Klauda (University of Maryland) helped me for understanding how to investigate the lipid properties in molecular dynamics simulation.

I also thank my colleagues in the Im group, past, present, and rotators: Jinhyuk Lee, Thenmalarchelvi Rathinavelan, Vidyashankara G Iyer, Huan Rui, Sunhwan Jo, Xi Cheng, Kyuil Lee, Soohyung Park, Huisun Lee, Emilia L. Wu, Kevin Song, Phillip Morris, Danielle Stuhlsatz, John Kim, and Jacob Wilson. They have made the Im lab a wonderful place to work and I have enjoyed their company immensely.

Finally, I thank my family. My wife Juwon has been always with me since I started my Ph.D. study. None of these works were possible without her selfless support. I would like to acknowledge my father Sukchang Kim, mother Kyungsook Park, and sister Jungmee Kim, who have provided me with endless love and support throughout my graduate studies and in each step my life. I think my father- and mother-in-law for the support they have given Juwon and I.

Membrane Proteins... the Final Frontier.

These are the voyages of Taehoon Kim during 5 year Ph.D. Studies. Its continuing mission: to explore strange new worlds, to seek out new phenomenon and new methods, ***to boldly go where no one has gone before.***

October, 2011
Taehoon Kim
University of Kansas

Table of Contents

List of Tables

List of Figures

Chapter I

Introduction

1.1. Membrane Proteins and Hydrophobic Mismatch

A biological membrane represents complex, highly heterogeneous combinations of various components such as lipids, cholesterol, peptides and proteins. The heterogeneity of membrane is mostly observed in the presence of integrated proteins which have one or several segments spanning across lipid bilayers. Membrane proteins play important roles in many vital cellular processes, such as transmembrane (TM) signaling (1, 2), transport of ions and small molecules (3-7), energy transduction (8, 9), and cell-cell recognition (10). Therefore, it is not surprising that they make up about 30 % of the protein-encoding regions of known genomes (11). In spite of their obvious importance, knowledge on the structural properties of membrane proteins is still relatively sparse. As shown in Figure 1.1, the TM domain of most membrane proteins consists of one or multiple helices, and their interactions with surrounding lipids are important determinants for membrane protein structure and function. Understanding of membrane protein functions thus requires not only the protein structural information, but also information on how the lipid environments affect protein structure and organization.

The match between the hydrophobic length of the TM domain (L_{TM}) and that of the lipid bilayer (L_{LIP}) in Figure 1.2 has been recognized as a central feature in protein-lipid interactions and bilayer regulation of membrane protein functions (12).

$$\text{Hydrophobic Mismatch} = \left| L_{TM}\cos\tau - L_{LIP} \right| \tag{1.1}$$

where τ represents a tilt angle of TM helix (τ is defined as the angle between the helical principal axis and the unit vector along the *Z*-axis (13)). Hydrophobic mismatch occurs if the L_{TM} of the membrane protein does not match the L_{LIP} of the membrane. The activity of membrane proteins depends strongly on the hydrophobic thickness of the bilayer and is often decreased in nonmatching situations (12, 14). As shown in Figure 1.2, this hydrophobic mismatch can lead to stretching or compression of lipid bilayers and proteins within the membrane or to tilting of TM helices to decrease the hydrophobic height.

Due to the large size of membrane proteins, the response of the tilt angles (τ) of TM segments to hydrophobic mismatch has been studied by using smaller membrane-spanning α-helical peptides for particular experiments. A hydrophobic mismatch has been systematically investigated by changing the hydrophobic length of TM helices or the hydrophobic thickness of lipid bilayers. In particular, to minimize the interaction between TM helices, single-span peptides, such as WALP ($GWW(LA)_nLWWA$) and KALP ($GKK(LA)_nLKKA$) containing poly-leucine/alanine flanked by tryptophan or lysine, have been extensively used both in experimental (12, 15-20) and computational (21-26) studies to characterize a main response to a hydrophobic mismatch as well as the role of peptide-lipid interactions. However, in most cases this response was not sufficient to fully compensate for mismatch. For example, ^2H NMR experiment suggested that the tilt angle for WALP23 peptides increased from 5.2° in di-C14:0PC (DMPC) to 8.1° in di-C12:0PC (DLPC) (17). Considering geometrics, this change in tilt angle would be too

small to compensate for the changes in bilayer thickness. Furthermore, these tilt angles differ significantly from much larger tilt angles (~30°) observed in molecular dynamics (MD) simulations (22, 24, 25, 27, 28).

The interplay between the structure and the energetics of lipid and protein components of biomembranes is of long-standing interest in biophysics. Structural and dynamic changes of the TM domain in response to a hydrophobic mismatch as well as molecular forces governing such changes remain to be fully understood at the atomic level. In particular, given the abundance of membrane proteins with a single-pass TM helix and their association and conformational changes involved in TM-induced signaling (29, 30), it is important and challenging to understand such properties quantitatively.

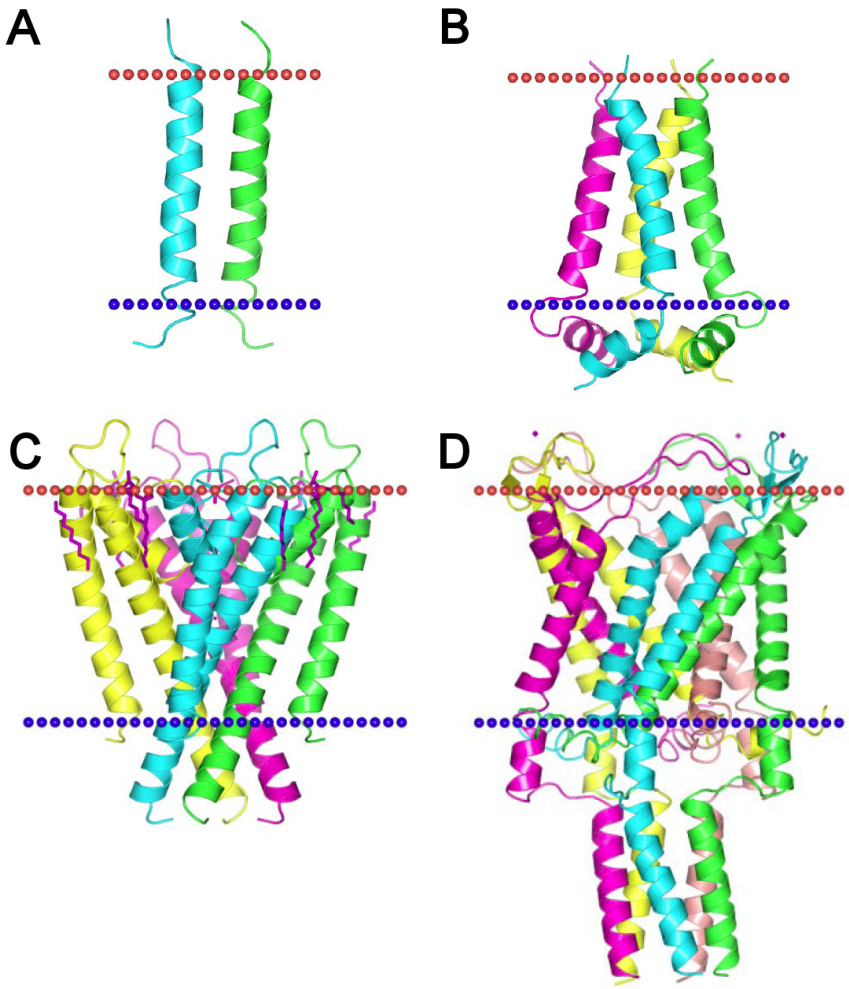

[1]**Figure 1.1.** Various membrane proteins. (A) Dimer of T cell receptor (PDB: 2HAC), (B) M2 proton channel of influenza A (PDB: 2KWX), (C) Potassium channel KcsA (PDB: 1R3J), and (D) Mechanosensitive channel MscL (PDB: 2OAR)

[1] From OPM database (http://opm.phar.umich.edu)

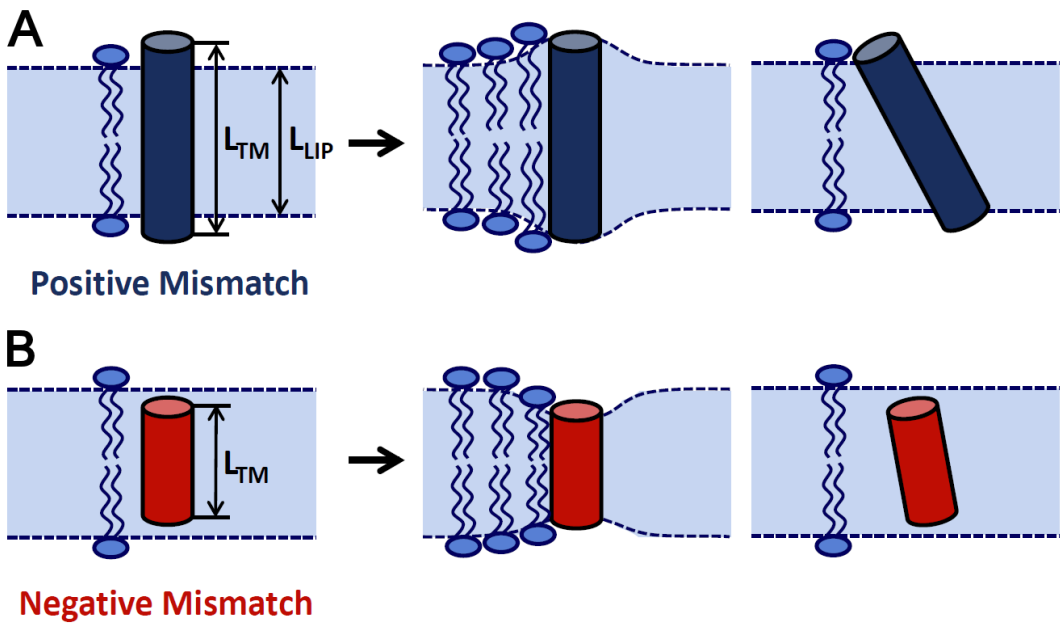

Figure 1.2. Schematic representation of possible hydrophobic mismatch conditions and its lipid adaptations. (A) Positive mismatch condition. (B) Negative mismatch condition. L_{TM} represents the length of hydrophobic segment in TM helix. L_{LIP} represents hydrophobic thickness of lipid bilayer

1.2. Outline of Thesis

This dissertation mainly focused on understanding of the influence of hydrophobic mismatch on structure and dynamics of TM helices and lipid bilayers. In Chapter 2, through an umbrella sampling MD simulation, PMFs and trajectory analyses provide in-depth understanding of detailed interplays of specific helix-lipid interactions in TM helix tilting and lipid adaptations under various hydrophobic mismatch conditions.

In Chapter 3, the TM helix dynamics that is possibly embedded in solid-state NMR (SSNMR) deuterium (^{2}H) quadrupolar splitting (DQS) measurements is determined and the long-standing discrepancy between MD simulation and experimental interpretation on TM helix orientation and dynamics will be reconciled. The results in Chapter 3 will demonstrate how to extract the orientational and dynamic information of TM helices from their SSNMR observables.

Finally, in the last chapter, to explore the influence of hydrophobic mismatch on the structure and dynamics of gramicidin A (gA) bilayer-spanning dimers (channels) and channel-forming subunits as well as the lipids in the vicinity of the channel or subunit, I undertook MD simulations on gA channels and monomers embedded in just one leaflet in bilayers of different thickness. The simulations were done in the bilayers of different hydrophobic thickness such as dilaurylphosphatidyl-choline (DLPC), dimyristoylphosphatidyl-choline (DMPC), dioleoylphosphatidyl-choline (DOPC), and palmitoyloleoylphosphatidyl-choline (POPC). The results show that the channel structure

varied little as the bilayer thickness is varied, meaning that the channel is relatively rigid, and that lipid bilayer adapts to the bilayer-spanning channel. The lipid organization in the vicinity of the dimer was unexpectedly complex, however, in the sense that the bilayer thickness did not vary monotonically as function of distance from the channel.

Chapter II

Hydrophobic Mismatch with Free Energy Simulation Studies of Transmembrane Helix's Tilt and Rotation[1]

[1] Reused from *Biophysical Journal*, Taehoon Kim and Wonpil Im, **99**. 2010. pp 175-183. Copyright (2010). with permission from Elsevier Science.

Summary

Protein-lipid interaction and bilayer regulation of membrane protein functions are largely controlled by the hydrophobic match between the transmembrane (TM) domain of membrane proteins and the surrounding lipid bilayer. To systematically characterize responses of a TM helix and lipid adaptations to a hydrophobic mismatch, we have performed a total of 5.8-μs umbrella sampling simulations and calculated the potentials of mean force (PMFs) as a function of TM helix tilt angle under various mismatch conditions. Single-pass TM peptides called WALP*n* (*n* = 16, 19, 23, and 27) were used in two lipid bilayers (dimyristoylphosphatidyl-choline and palmitoyloleoylphosphatidyl-choline) with different hydrophobic thicknesses to consider hydrophobic mismatch caused by either the TM length or the bilayer thickness. In addition, different flanking residues, such as alanine, lysine, and arginine, instead of tryptophan in WALP23 were used to examine their influence on TM helix orientation.

The PMFs, their decomposition, and trajectory analyses demonstrate that 1), tilting of a single-pass TM helix is the major response to a hydrophobic mismatch; 2), TM helix tilting up to ~10° is inherent due to the intrinsic entropic contribution arising from helix precession around the membrane normal even under a negative mismatch; 3), the favorable helix-lipid interaction provides additional driving forces for TM helix tilting under a positive mismatch; 4), the minimum-PMF tilt angle is generally located where there is the hydrophobic match and little lipid perturbation; 5), TM helix rotation is

dependent on the specific helix-lipid interaction; and 6), anchoring residues at the hydrophilic/hydrophobic interface can be an important determinant of TM helix orientation.

2.1. Introduction

The transmembrane (TM) domain of most membrane proteins consists of one or multiple helices, and their interactions with surrounding lipids are important determinants for membrane protein structure and function. Understanding of membrane protein functions thus requires not only the protein structural information, but also information on how the lipid environments affect protein structure and organization. The match between the hydrophobic length of the TM domain and that of the lipid bilayer has been recognized as a central feature in protein-lipid interactions and bilayer regulation of membrane protein functions (12). Responses to an energetically unfavorable hydrophobic mismatch include conformational changes of the TM domain, lipid adaptations by changes in bilayer thickness and lipid chain order, and TM helix association (31). In particular, the changes in TM helix tilt, kink, and rotation angles to relieve any mismatch are often considered key conformational changes implicated in a switch between active and inactive conformations of membrane proteins (32-34). However, structural and dynamic changes of the TM domain in response to a hydrophobic mismatch as well as molecular forces governing such changes remain to be fully understood at the atomic level. In particular, given the abundance of membrane proteins with a single-pass TM helix and their association and conformational changes involved in TM-induced signaling (29, 30), it is important and challenging to understand such properties quantitatively.

Mainly due to experimental difficulties associated with membrane proteins of

multiple TM helices, our understanding of hydrophobic mismatch effects is mostly based on studies using various single-pass TM helices in model lipid bilayers. The responses to a hydrophobic mismatch have been systematically investigated by changing the hydrophobic length of TM helices or the hydrophobic thickness of lipid bilayers. In particular, designed TM helical peptides, such as WALP and KALP containing poly-leucine/alanine flanked by tryptophan or lysine (Table 2.1), have been extensively used both in experimental (12, 15-20) and computational (21-26) studies to characterize a main response to a hydrophobic mismatch as well as the role of peptide-lipid interactions. In the case of a single-pass TM helix, helix tilting is generally considered the main response to a hydrophobic mismatch with minimum perturbation of lipid bilayers (26, 35). Recently, based on the potential-of-mean-force (PMF) calculation as a function of WALP19's tilt angle in a dimyristoylphosphatidyl-choline (DMPC) bilayer, Lee and Im (26) have provided novel insights (to our knowledge) into the driving forces of TM helix tilting in the lipid bilayer: a thermally accessible tilt region of a single-pass TM helix is governed by the intrinsic entropic contribution arising from helix precession (area) around the membrane normal and the helix-lipid interactions that could be TM sequence- and length-specific.

The aim of this work is to provide in-depth understanding of detailed interplays of specific helix-lipid interactions in TM helix tilting and lipid adaptations under various hydrophobic mismatch conditions. We have performed a total of 5.8-μs umbrella sampling molecular dynamics (MD) simulations (36) to calculate the PMFs of various

single-pass TM helices as a function of their tilt and rotation angles (13, 37) and analyzed the resulting PMFs by the free energy decomposition technique (13, 26).

First, we used WALP*n* (*n* = 16, 19, 23, and 27; Table 2.1) in DMPC bilayers to determine the influence of the TM hydrophobic length on TM helix orientation and lipid adaptations. Second, the results in DMPC were compared with those in palmitoyloleoylphosphatidyl-choline (POPC) bilayers to characterize the influence of the bilayer hydrophobic thickness on TM helix orientation and lipid adaptations. Third and finally, we used alanine, lysine, and arginine as a flanking residue instead of tryptophan in WALP23 in DMPC to examine the influence of various anchoring residues on TM helix orientation and lipid adaptations (19). The PMFs, their decomposition, and trajectory analysis are discussed and generalized in terms of responses of a TM helix and lipid adaptations to various hydrophobic mismatch conditions.

Table 2.1. Amino acid sequences of WALP*n* (*n* = 16, 19, 23, and 27) and *X*ALP23 (*X* = A, K, and R) peptides.

Peptide	Sequence[a]	TM hydrophobic length (Å)[b]
WALP16	GWW**LALALAL ALA**WWA	15.0
WALP19	GWW**LALALAL ALALAL**WWA	19.5
WALP23	GWW**LALALAL ALALALALAL** WWA	25.5
WALP27	GWW**LALALAL ALALALALAL ALAL**WWA	31.5
AALP23	G**AALALALAL ALALALALAL AA**A	31.5
KALP23	GWW**LALALAL ALALALALAL** KKA	25.5
RALP23	GWW**LALALAL ALALALALAL** RRA	25.5

[a]The N terminus of each peptide is blocked by the acetyl group and its C terminus by the N-methyl amide group.

[b]The lengths are measured in the hydrophobic region (bold) with an assumption of an ideal α-helix.

2.2. Computational Methods

2.2.1. Defining the tilt and rotation angle

The orientation of a TM helix is defined by its tilt (τ) and rotation (ρ) angles. With the *Z*-axis parallel to the membrane normal, τ is defined as the angle between the helical principal axis and the unit vector along the *Z*-axis (13). To define ρ, both the internal and external references have to be defined (Figure 2.1). The internal reference is given by the vector pointing from the helical axis to Cα atom of Leu^{14} in all WALP peptides except WALP16/19. Because the position of Leu^{14} in WALP16/19 is too close to the C-terminus, the flexibility of which makes it difficult to define ρ, we instead used Ala^{7} (WALP16) and Leu^{10} (WALP19), which are at a similar position to Leu14 on the helical wheel projection. With the unit vector along the *Z* axis as the external reference, ρ is then defined as the angle between the projections of such reference vectors on the plane made by the second and third helical principal axes. Detailed expressions can be found in our previous works (13, 38).

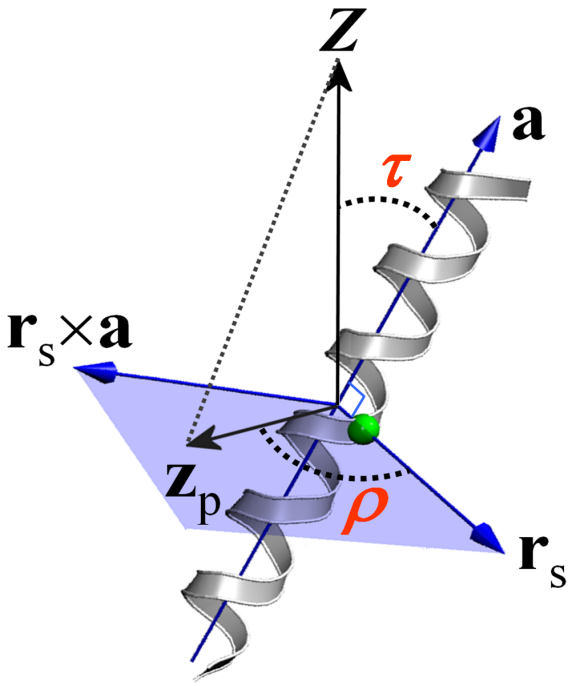

Figure 2.1. The definitions of helix tilt (τ) and rotation (ρ). The value r is defined as the angle between the perpendicular vector ($\mathbf{r_s}$) from the helical axis (**a**) to the selected Cα atom (*green circle*) and the projection vector ($\mathbf{z_p}$) of the Z-axis onto the plane (*light blue*) made by the second and third principal axes. The sign of the rotational angle becomes positive if $\mathbf{z_p} \times \mathbf{r_s}$ is in the opposite direction to **a**, or negative otherwise.

2.2.2. Umbrella sampling simulation

The sequence of each peptide studied in this work is given in Table 2.1. Using the input scripts from the *Membrane Builder* module (39, 40) in CHARMM-GUI (www.charmm-gui.org) (41), each peptide with an ideal α-helical conformation ($\phi = -57.8°$; $\psi = -47.0°$) was inserted into a pre-equilibrated lipid bilayer of 72 DMPC (or POPC) and water molecules with $\tau = 0°$ and its center at $Z = 0$. Four chloride ions were added to neutralize the KALP23 and RALP23 systems. To relax the uncorrelated initial systems, 400-ps equilibration was performed with harmonic restraints on heavy atoms. The number of individual components and each system size are listed in Table 2.2. The snapshots of each system at $\tau = 0°$ are shown in Figure 2.2.

To perform umbrella sampling MD simulations as a function of TM helix tilt, an initial structure at each window was generated by tilting the helix sequentially from 0° to a specific maximum angle by 1° every 100 ps. The total number of windows and the maximum τ are listed in Table 2.1. Each window was then subjected to 1-ns equilibration followed by 10- or 12.5-ns production. The force constants of the helix tilt restraint potential (13) were set to 2,000 and 6,000 kcal/(mol·rad^2) (26) for equilibration and production, respectively. All calculations were performed using the biomolecular simulation program CHARMM (42) with the all-atom parameter set PARAM22 for protein (43) including the dihedral cross-term corrections (44) and a modified TIP3 water model (45), as well as recently optimized lipid parameters (46). The cross-sectional areas

of DMPC and POPC were set to 60.7 Å^2 and 68.3 Å^2 at 303.15 K (47), respectively. Following the same protocol in the previous PMF calculation of WALP19 (26), a time-step of 2 fs was used with the SHAKE algorithm (48), and the constant temperature (303.15 K) and pressure (1 atm along the *Z*-direction) were maintained by the Nosé-Hoover method (49) and the Langevin-piston algorithm (50), respectively, for the NPAT (constant pressure, surface area, and temperature) dynamics. We used the same options for nonbonded interactions in the input scripts provided by the CHARMM-GUI *Membrane Builder* (39, 40).

The PMF, $W(\tau)$, as a function of τ was calculated by integrating the reversible work done by the mean force, $-\langle F(\tau)\rangle_\tau$, along τ;

$$\frac{dW(\tau)}{d\tau} = -\langle F(\tau)\rangle_\tau = \left\langle \frac{\partial U(\mathrm{r})}{\partial \tau} - k_B T \frac{\partial \ln |J|}{\partial \tau} \right\rangle_\tau \tag{2.1}$$

where $U(\mathbf{r})$ is the potential energy of the system, $|J|$ is the determinant of the Jacobian related to the transformation of the Cartesian coordinate into the generalized coordinate τ, and k_B is the Boltzmann constant. To examine the PMF convergence, the trajectory in each window was sequentially divided into every 1-ns duration. The PMFs were then calculated from each sub-trajectory. The largest standard deviation of the PMF occurs at either energetically unfavorable small or large tilt angle region (Figure 2.3). When the PMF was constructed using the last 8-ns trajectory, even the highest standard deviation does not exceed ±2.2 kcal/mol (in the RALP23/DMPC system), illustrating that the calculated PMFs are well converged.

Table 2.2. Detail information of each simulation system.

System Peptide/Lipid	Tilt Range (degs)	Number of Windows	Time (ns)	Number of Water (ion)
WALP16/DMPC	0 ~ 40	41	10	2,056
WALP19/DMPC	0 ~ 40	41	10	2,075
WALP23/DMPC	0 ~ 50	51	12.5	2,062
WALP27/DMPC	0 ~ 70	71	12.5	2,507
WALP16/POPC	0 ~ 40	41	10	2,537
WALP19/POPC	0 ~ 40	41	10	2,524
WALP23/POPC	0 ~ 50	51	10	2,662
WALP27/POPC	0 ~ 50	51	12.5	2,711
AALP23/DMPC	0 ~ 50	51	10	2,062
KALP23/DMPC	0 ~ 40	41	10	2,062 (4)
RALP23/DMPC	0 ~ 40	41	10	2,062 (4)

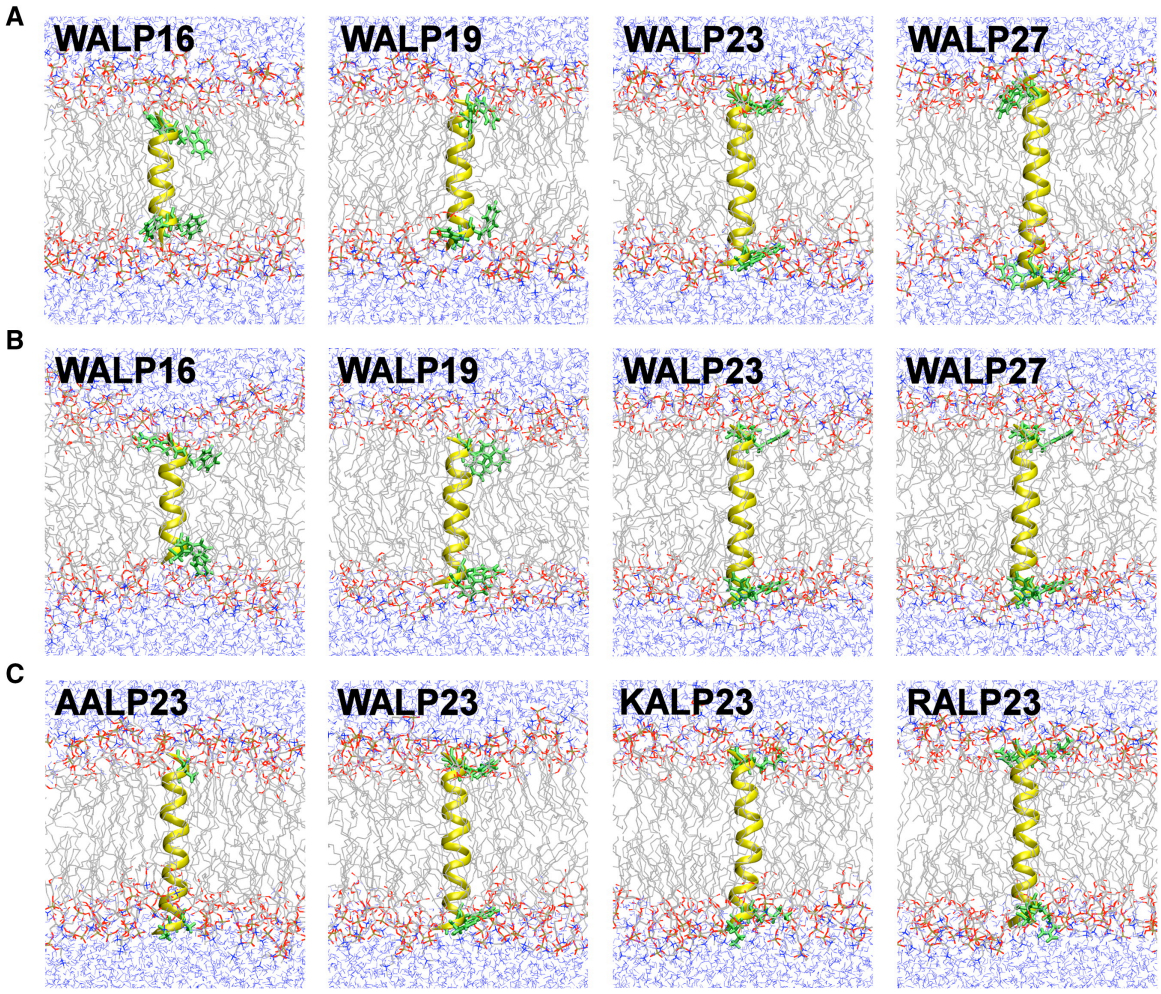

Figure 2.2. Molecular graphic view of the last snapshot in (A) WALP*n* (*n* = 16. 19, 23, and 27) in DMPC bilayers, (B) WALP*n* in POPC bilayers, and (C) *X*ALP23 (*X* = A, W, K, and R) in DMPC bilayers at $\tau = 0°$ (the helix in *yellow*, anchoring residues in *green*, lipid tails in *gray*, and water molecules in *blue*).

2.3. Results and Discussion

2.3.1. Influence of hydrophobic length of TM helices

Tilting of a TM helix in a bilayer is affected by its TM hydrophobic length (L_{TM}) and the bilayer hydrophobic thickness ($L_{bilayer}$) whose difference can cause either positive ($L_{TM} > L_{bilayer}$) or negative ($L_{TM} < L_{bilayer}$) hydrophobic mismatch. In a DMPC bilayer with $L_{bilayer} \approx 23$ Å (16), WALP16/19 and WALP23/27 at $\tau = 0°$ are under negative and positive mismatch conditions, respectively (see L_{TM} in Table 2.1). Figure 2.3 (A) shows the total PMFs of the WALP*n*/DMPC systems as a function of τ. The detailed information about the minimum-PMF tilt angle (τ_{min}) and the free energy change from $\tau = 0°$ to τ_{min}, $\Delta W(0 \rightarrow \tau_{min})$, in each system is summarized in Table 2.3. As L_{TM} increases, τ_{min} increases, $\Delta W(0 \rightarrow \tau_{min})$ decreases, and the thermally-accessible tilt region becomes wider, clearly illustrating that it is energetically more favorable for TM helices of longer L_{TM} to have larger τ_{min} in order to maximize the hydrophobic match. In the case of WALP23, its τ_{min} is similar to the average tilt ($\tau = 33.5°$) from the recent multiple MD trajectories (24).

Also, although the lipid types are different, the large τ_{min} from the PMF appears to be consistent with the recent fluorescence spectroscopy experiment (35) that shows much larger tilt angle of WALP23 ($\tau = 24° \pm 5°$) in a DOPC membrane than the tilt angle (τ = 4.4°~8.2°) estimated from solid-state ^{2}H-NMR quadrupolar splitting measurements (17, 19).

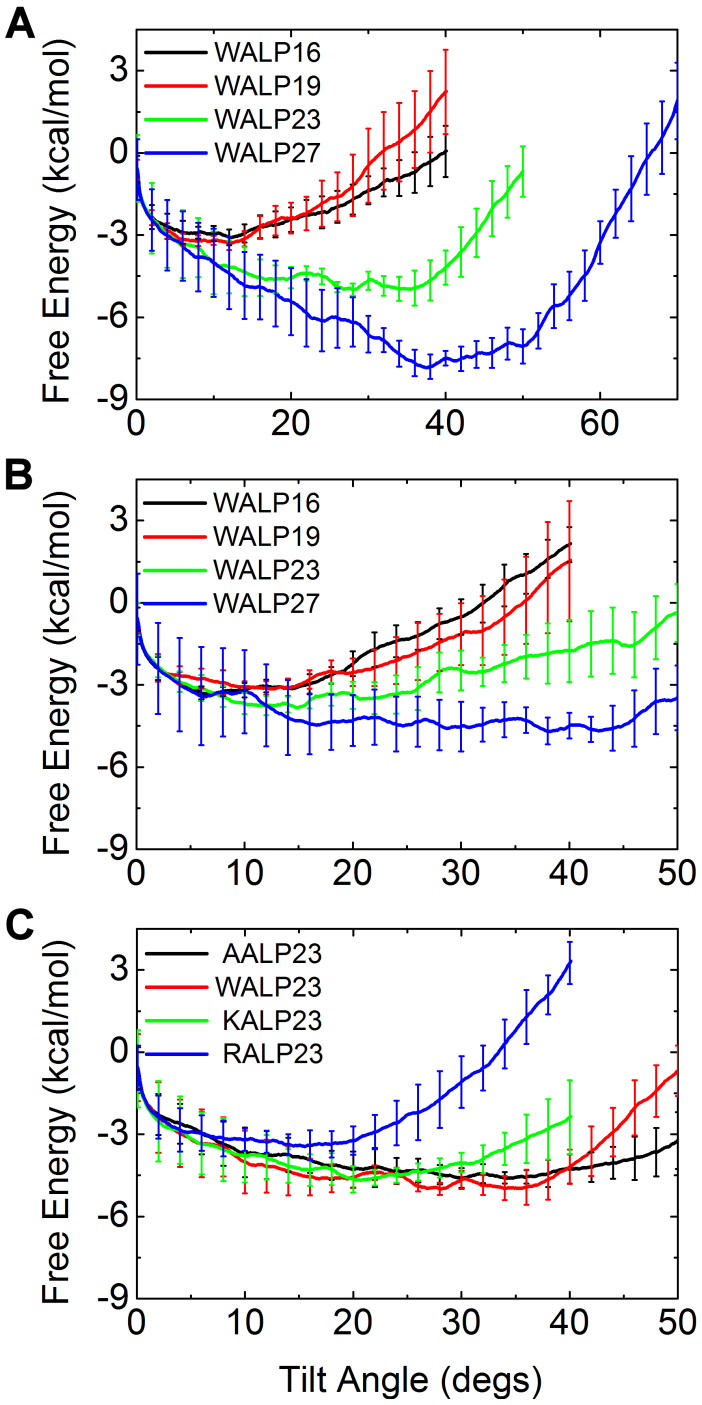

Figure 2.3. The total PMFs as a function of τ in (A) WALP*n* in DMPC bilayers, (B) WALP*n* in POPC bilayers, and (C) *X*ALP23 in DMPC bilayers.

Table 2.3. The summary of the PMF in each system.

System Peptide/Lipid	minimum-PMF Tilt Angle / $\Delta W(0 \rightarrow \tau_{min})$ (kcal/mol)	Thermal-Accessible Tilt Range
WALP16/DMPC	12.1° / −3.09 ± 0.27	2.6° ~ 19.4°
WALP19/DMPC	12.1° / −3.30 ± 0.24	3.1° ~ 16.1°
WALP23/DMPC	28.1° / −4.99 ± 0.21	14.4° ~ 39.0°
WALP27/DMPC	43.3° / −7.45 ± 0.51	32.3° ~ 50.7°
WALP16/POPC	6.4° / −3.33 ± 0.21	3.3° ~ 17.4°
WALP19/POPC	12.5° / −3.14 ± 0.29	2.7° ~ 19.9°
WALP23/POPC	14.9° / −3.83 ± 0.28	6.7° ~ 25.6°
WALP27/POPC	38.2° / −4.70 ± 0.49	13.7° ~ 46.3°
AALP23/DMPC	34.2° / −4.60 ± 0.19	16.5° ~ 44.5°
KALP23/DMPC	20.7° / −4.68 ± 0.41	13.6° ~ 29.3°
RALP23/DMPC	15.6° / −3.44 ± 0.53	4.0° ~ 22.4°

TM helix tilting is governed by the intrinsic entropic contribution ($W_{entropy}$) arising from helix precession (area) around the membrane normal and the specific helix-lipid interactions (W_{int}) (26). To determine detailed interplays of underlying molecular forces in TM helix tilting in the WALP*n*/DMPC systems, the total PMF of each system was decomposed into W_{int} and $W_{entropy}$ based on Equation (2.1). It should be noted that W_{int} also includes the helix conformational changes resulted from the helix-lipid interactions. As shown in Figure 2.4, (A) and (B), under the negative mismatch condition such as the WALP16/19 systems, it is evident that tilting up to τ_{min} is driven by $W_{entropy}$. After τ_{min}, W_{int} makes the dominant contribution to the increase of the PMFs. These results clearly explain the microscopic driving forces of previous MD simulation observations that a short TM helix can tilt up to ~10° in a membrane even under a negative mismatch condition (23). As L_{TM} increases, such as WALP23/27 in Figure 2.4, (C) and (D), the W_{int} contribution to the total PMF becomes more significant to maximize the hydrophobic match and provides additional driving forces for TM helix tilting.

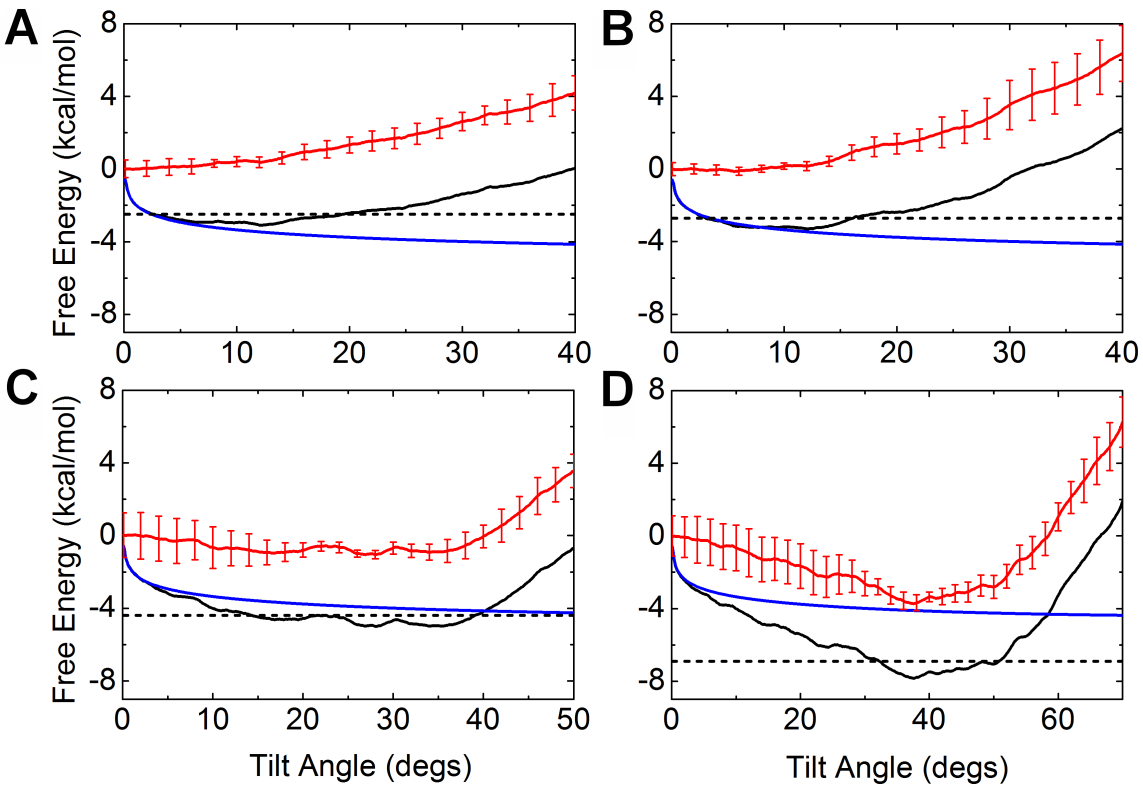

Figure 2.4. Decomposition of the total PMF (black) into the helix-lipid interaction (W_{int}: *red*), the entropic contribution ($W_{entropy}$: *blue*), and the thermally-accessible region (*black dashed*) in (A) WALP16, (B) WALP19, (C) WALP23, and (D) WALP27 in DMPC bilayers.

The W_{int} contribution can be further characterized in terms of lipid adaptations, hydrophobic match, and helix conformational changes as a function of τ. In particular, it has been postulated that the lipids in the vicinity of an integral membrane protein would change their hydrophobic length or the protein itself undergoes conformational changes to maximize the hydrophobic match (i.e., to minimize the energy penalty of exposing nonpolar residues to aqueous solution) (51). The present umbrella sampling simulation trajectory provides an excellent resource to quantify such changes at the atomic level, which would be difficult to measure in normal MD simulations because of limited sampling along TM helix orientations. In this study, the local lipid adjustment is quantified by $\Delta L^{\text{adaptation}} = \left\langle L_{\text{bilayer}}^{\text{contact}} \right\rangle - \left\langle L_{\text{bilayer}}^{\text{bulk}} \right\rangle$, where $\left\langle L_{\text{bilayer}}^{\text{contact}} \right\rangle$ and $\left\langle L_{\text{bilayer}}^{\text{bulk}} \right\rangle$ are the average hydrophobic thicknesses of contact and bulk lipid bilayers, respectively. L_{bilayer} is defined as an average distance between the acyl chain C2 carbon atoms in both leaflets (16). A lipid molecule that has any of its heavy atoms within 4 Å from the helix heavy atoms is classified as a 'contact' lipid, otherwise as a 'bulk' one. Therefore, the negative $\Delta L^{\text{adaptation}}$ indicates a local membrane thinning and the positive $\Delta L^{\text{adaptation}}$ a local membrane thickening with respect to the bulk lipid bilayer. $\Delta L^{\text{adaptation}}$ as a function of τ in Figure 2.5 (A) clearly shows that the local lipids response differently to different hydrophobic mismatch conditions. For WALP16/19 that are under the negative mismatch ($L_{\text{bilayer}} > L_{\text{TM}}$) at $\tau = 0°$, the local membrane thinning ($\Delta L^{\text{adaptation}} < 0$) is apparent and $\Delta L^{\text{adaptation}}$ slightly decreases as τ increases. In contrast, for WALP23/27 that are under the positive mismatch ($L_{\text{bilayer}} < L_{\text{TM}}$) at $\tau = 0°$, the local membrane thickening ($\Delta L^{\text{adaptation}} > 0$) occurs

at small tilt angles, but becomes reduced as τ increases and disappears around τ_{min} where there is little local lipid perturbation due to the hydrophobic match (see below). After τ_{min}, to maximize hydrophobic match, the contact lipids become thinner ($\Delta L^{adaptation} < 0$) because the effective L_{TM} is reduced as τ increases. Figure 2.6 schematically illustrates how the local lipid adaptations occur at $\tau = 0°$, $\tau \approx \tau_{min}$, and $\tau > \tau_{min}$, based on Figure 2.5 (A).

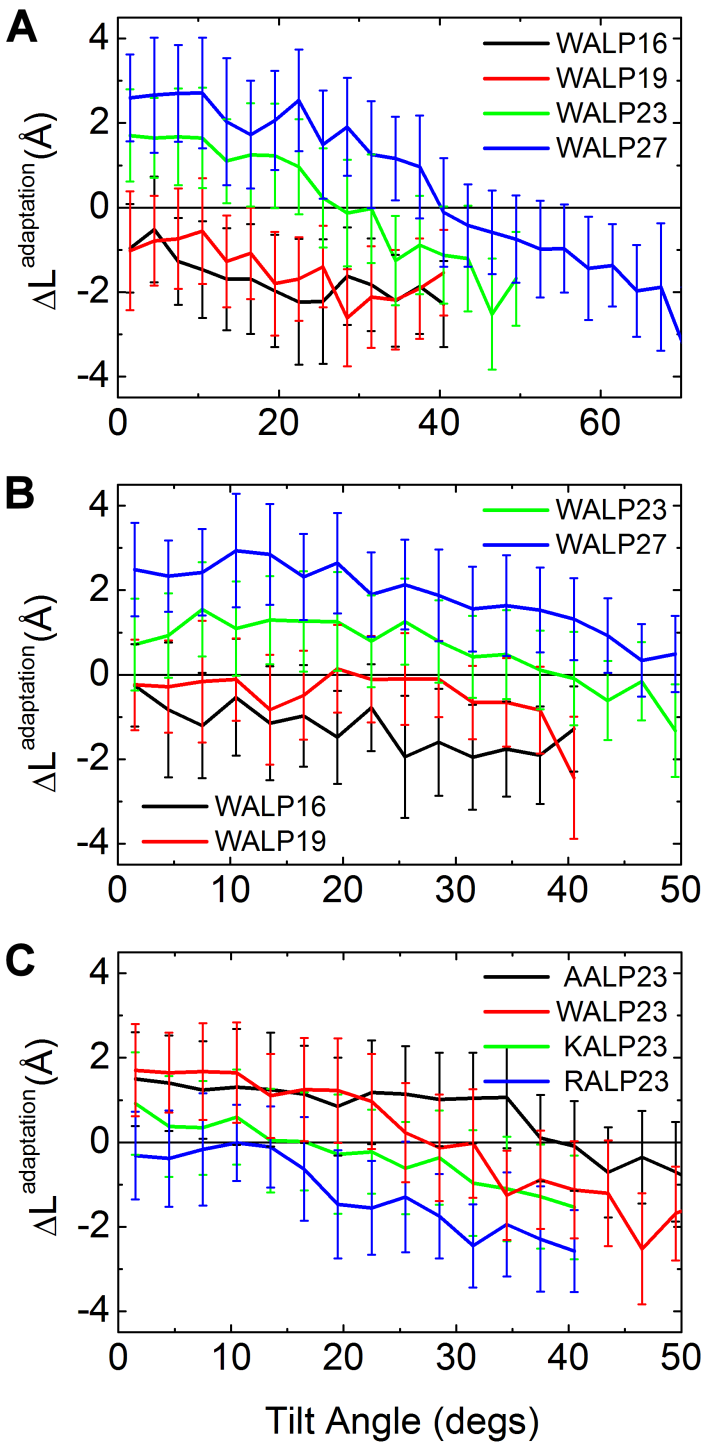
A
WALP16
WALP19
WALP23
WALP27
ΔL adaptation (Å)
4
2
0
-2
-4
0
20
40
60
B
WALP23
WALP27
WALP16
WALP19
ΔL adaptation (Å)
4
2
0
-2
-4
0
10
20
30
40
50
C
AALP23
WALP23
KALP23
RALP23
ΔL adaptation (Å)
4
2
0
-2
-4
0
10
20
30
40
50
Tilt Angle (degs)

Figure 2.5. Local lipid adjustment ($\Delta L^{\text{adaptation}}$) as a function of τ in (A) WALP*n*/DMPC, (B) WALP*n*/POPC, and (C) *X*ALP23/DMPC systems; $\Delta L^{\text{adaptation}} = \left\langle L_{\text{bilayer}}^{\text{contact}} \right\rangle - \left\langle L_{\text{bilayer}}^{\text{bulk}} \right\rangle$, where $\left\langle L_{\text{bilayer}}^{\text{contact}} \right\rangle$ and $\left\langle L_{\text{bilayer}}^{\text{bulk}} \right\rangle$ are the average hydrophobic thicknesses of contact and bulk lipid bilayers.

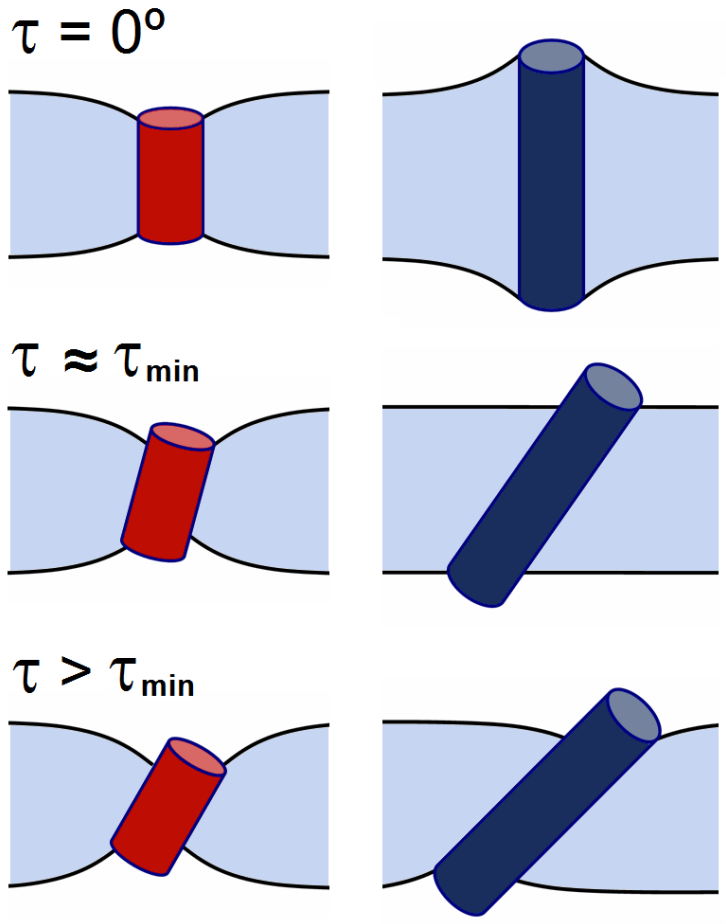

Figure 2.6. Schematic representation of the local lipid adjustment based on the Δ*L* change (Figure 2.5) under negative (left) and positive (right) hydrophobic mismatch conditions.

To quantify the extent of the hydrophobic match as a function of τ, we calculated the difference between the effective L_{TM} (17) and $\left\langle L_{bilayer}^{contact} \right\rangle$, i.e., $\Delta L^{mismatch} = L_{TM} \cos\tau - \left\langle L_{bilayer}^{contact} \right\rangle$ where both L_{TM} and $\left\langle L_{bilayer}^{contact} \right\rangle$ were calculated in two different ways: one from the simulation trajectory (solid lines in Figure 2.7) and the other from fixed values (L_{TM} in Table 1 and $\left\langle L_{bilayer}^{contact} \right\rangle$ = 23 Å (DMPC) or 26 Å (POPC)) (dotted lines in Figure 2.7). Since L_{TM} remained almost the same values as in Table 1 during the simulations, the difference in two lines represents the influence of the local lipid adaptations on $\Delta L^{mismatch}$. As shown in Figure 2.7 (A), for WALP16/19, despite of the local membrane thinning (Figure 2.5 (A)), the negative hydrophobic mismatch is apparent and slightly increases as τ increases (52). Therefore, it becomes clear that the W_{int} contribution is not favorable for tilting of WALP16/19 in DMPC bilayer (Figure 2.4, (A) and (B)) because of increased deformation of the lipid bilayer as τ increases. In contrast, for WALP23/27, τ at $\Delta L^{mismatch} \approx 0$ is well matched with τ_{min}, demonstrating that the local lipid adjustments toward $\Delta L^{mismatch} \approx 0$ (i.e., $\Delta L^{adaptation} \approx 0$ in Figure 2.5 (A)) provide the favorable W_{int} contribution for tilting of WALP23/27 toward τ_{min} (Figure 2.4, (C) and (D)) and relieve the deformation stress on the lipid bilayer. At $\tau > \tau_{min}$, however, bilayer deformation ($\Delta L^{adaptation} < 0$) causes stress on the lipid bilayer, making the W_{int} contribution unfavorable. While excessive stress on a lipid bilayer at extreme hydrophobic mismatch can induce helix deformations such as helix kink or bending, it becomes also apparent from the thermally-accessible tilt regions (Figure 2.3 (A) and

Table 2.3) that the membrane bilayer system can tolerate a certain extent of a hydrophobic mismatch by slight lipid adaptations.

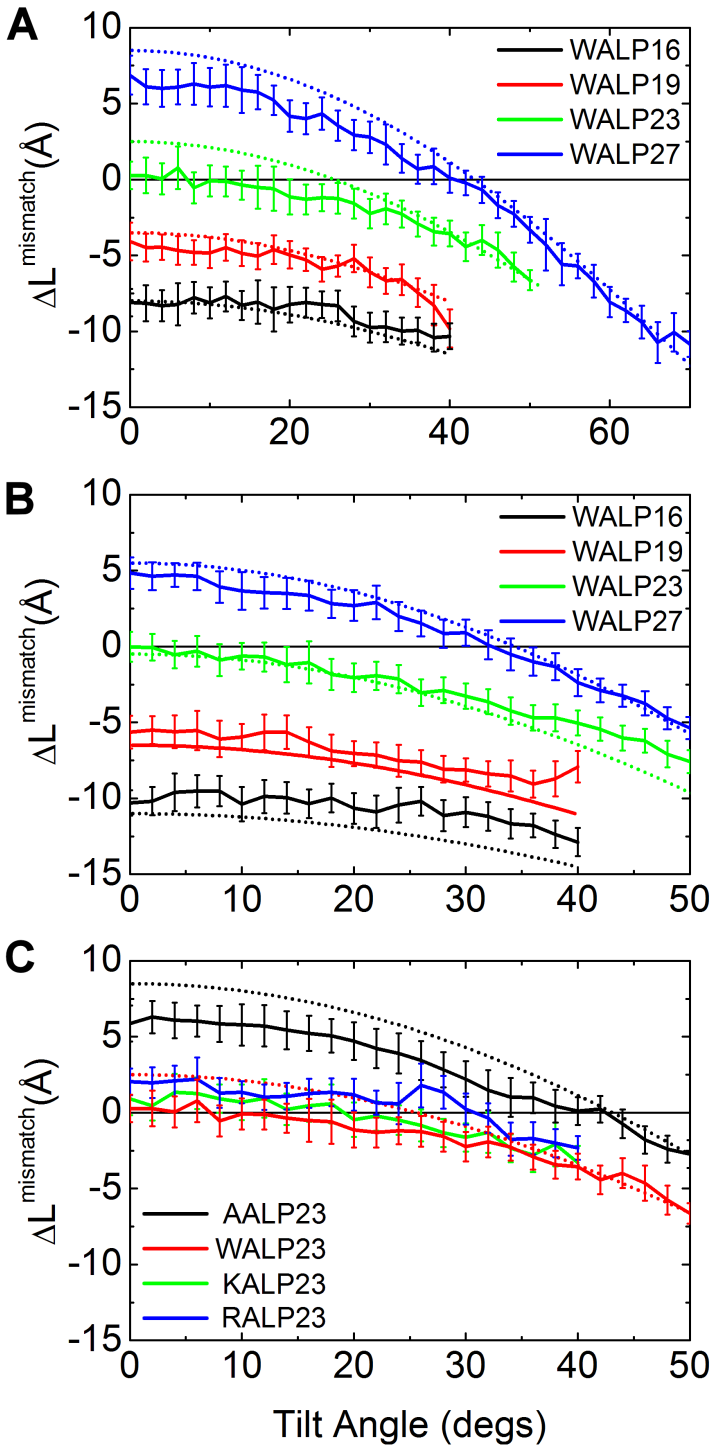
A
B
C
WALP16
WALP19
WALP23
WALP27
AALP23
WALP23
KALP23
RALP23
ΔL mismatch (Å)
Tilt Angle (degs)

Figure 2.7. Extent of the hydrophobic match ($\Delta L^{\text{mismatch}}$) as a function of τ in (A) WALP*n*/DMPC, (B) WALP*n*/POPC, and (C) *X*ALP23/DMPC systems; $\Delta L^{\text{mismatch}} = L_{\text{TM}} \cos\tau - \left\langle L_{\text{bilayer}}^{\text{contact}} \right\rangle$, where L_{TM} is the TM hydrophobic length and $\left\langle L_{\text{bilayer}}^{\text{contact}} \right\rangle$ is the average hydrophobic thicknesses of the contact lipids. Both L_{TM} and $\left\langle L_{\text{bilayer}}^{\text{contact}} \right\rangle$ were calculated from the simulation trajectory (solid lines) or they were set to fixed values (L_{TM} in Table 1 and $\left\langle L_{\text{bilayer}}^{\text{contact}} \right\rangle$ = 23 Å (DMPC) or 26 Å (POPC)) (dotted lines).

As shown in Figure 2.8 (A), the helicity of each helix is well maintained except at energetically unfavorable large τ. The previous study on WALP19 reveals that such helix deformation including helix bending at large τ is attributed to the existence of four Trp anchoring residues at the hydrophobic/hydrophilic interface (26). In other words, it is energetically more favorable for WALP19 to deform the helical conformation slightly at large τ in a DMPC bilayer, instead of having Trp sidechains inserted into the hydrophobic core (26). Figure 2.9 shows the center of mass of each Trp sidechain along the *Z*-axis (Z_{Trp}) as a function of τ. Similar to WALP19, Z_{Trp} of WALP16 is around the hydrophobic/hydrophilic interface of the lipid bilayer due to outward-facing of the Trp sidechains (see below), despite of their relatively short L_{TM}. However, the Trp sidechains of WALP23/27 appear to partition into the DMPC hydrophobic core region at large τ. Such difference arises from the following two reasons. First, since WALP16/19 are under the negative mismatch regardless of τ, the hydrophobic/hydrophilic interfacial matching becomes a dominant factor in optimizing their conformation during helix tilting. In contrast, WALP23/27 gain the favorable W_{int} contribution by optimizing the hydrophobic match, which becomes more dominant than the interfacial matching (at large τ). Second, the rotation angle of each helix during its tilting, determined by the helix-lipid interactions, also dictates the positioning of the Trp residues.

The direction of helix tilting (i.e., rotation angle, ρ) is also an important determinant of TM helix tilting. In our simulations, since the restraint forces are exerted

only on the Cα atoms that define the helical principal axis, the helix can rotate around the helical axis, depending on helix-environment (lipid or water) interactions (37). Figure 2.10 shows the change of ρ as a function of τ and also illustrates the tilting direction for each WALP*n*/DMPC system. In general, ρ shows large fluctuations at $\tau < 10°$ (due to ill-definition of ρ and low free energy barriers at small tilt angles), but converged to a specific angle with less fluctuation around τ_{min}. It becomes clear that Z_{Trp} in Figure 2.9 is related to the tilting direction. For example, WALP23/27 tilt in a direction between Trp2 and Trp3, so that the Trp residues partition into the membrane hydrophobic region at large τ.

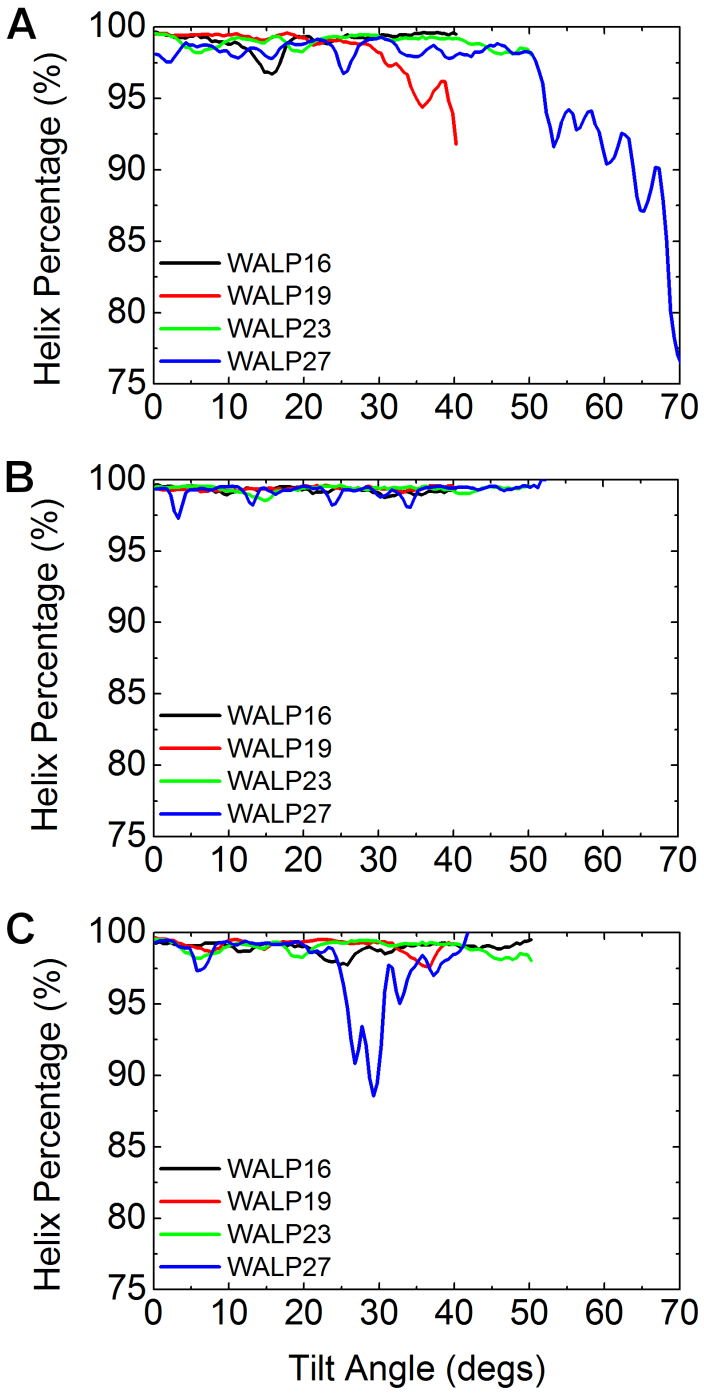
A
B
C
Helix Percentage (%)
100
95
90
85
80
75
0
10
20
30
40
50
60
70
WALP16
WALP19
WALP23
WALP27
Tilt Angle (degs)

Figure 2.8. Helicity of each helix as a function of tile (τ) in (A) WALP*n*/DMPC, (B) WALP*n*/POPC, and (C) *X*ALP23/DMPC systems. Helicity is measured based on the number of hydrogen bond between N−H (*i*) and C=O (*i* + 4) of backbone. A hydrogen bond (D−H···A) is defined by the H···A distance less than 2.8 Å and the D−H···A angle greater than 120°.

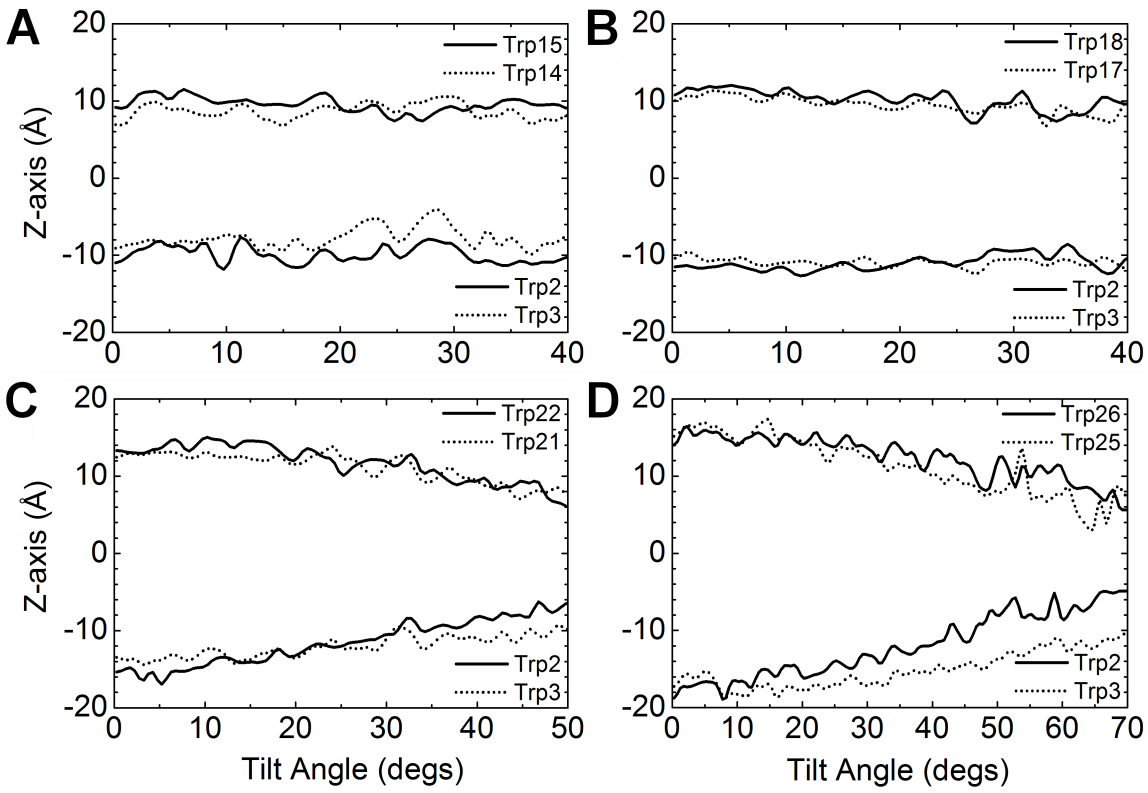

Figure 2.9. Average locations of Trp sidechains as a function of τ in (A) WALP16 (Trps 2, 3, 14, and 15), (B) WALP19 (Trps 2, 3, 16, and 17), (C) WALP23 (Trps 2, 3, 21, and 22), and (D) WALP27 (Trps 2, 3, 25, and 26) in DMPC bilayers.

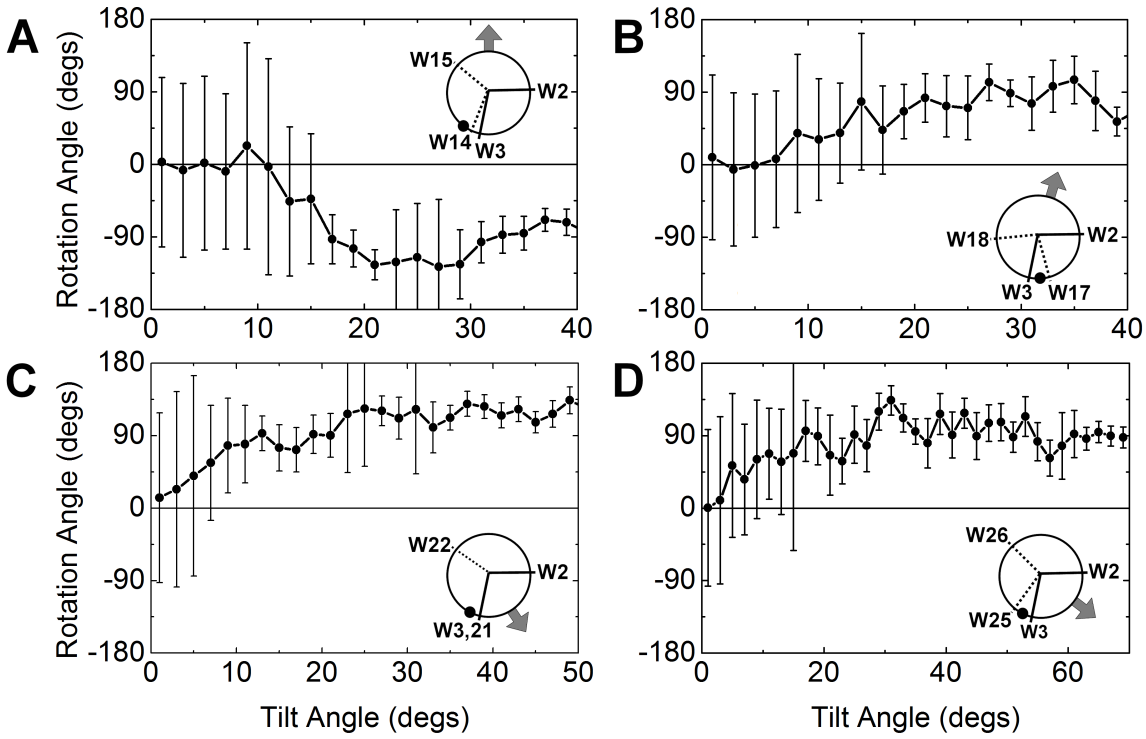

Figure 2.10. TM helix rotation angle (ρ) as a function of τ in (A) WALP16, (B) WALP19, (C) WALP23, and (D) WALP27 in DMPC bilayers. The reference atoms, such as Ala^{7} (for WALP16), Leu^{10} (for WALP19), and Leu^{14} (for others), and the tilting direction at τ_{min} are indicated by black circles and gray arrows on the helical view, respectively.

To verify that the helix follows the energetically favorable orientation during the tilting simulations, we have performed additional PMF calculations of WALP23 as a function of τ by restraining ρ at four distinct rotation angles, i.e., $\rho = -150°$, $-60°$, $30°$, and $120°$. As shown in Figure 2.11, the tilting energetics is largely dependent on ρ, and the lowest tilting PMF is found with $\rho = 120°$, which corresponds to ρ at $\tau = \tau_{min}$ ($120.8° \pm 18.5°$) in Figure 2.11 (C). This rotation is also well correlated with $\rho = 155°$ (using our definition) estimated from the solid-state ^{2}H-NMR study (19). Clearly, our results demonstrate that each helix prefers to tilt with a specific rotation based on hydrophobic or interfacial matching, and the helix adopts the energetically favorable orientation during the tilting simulations.

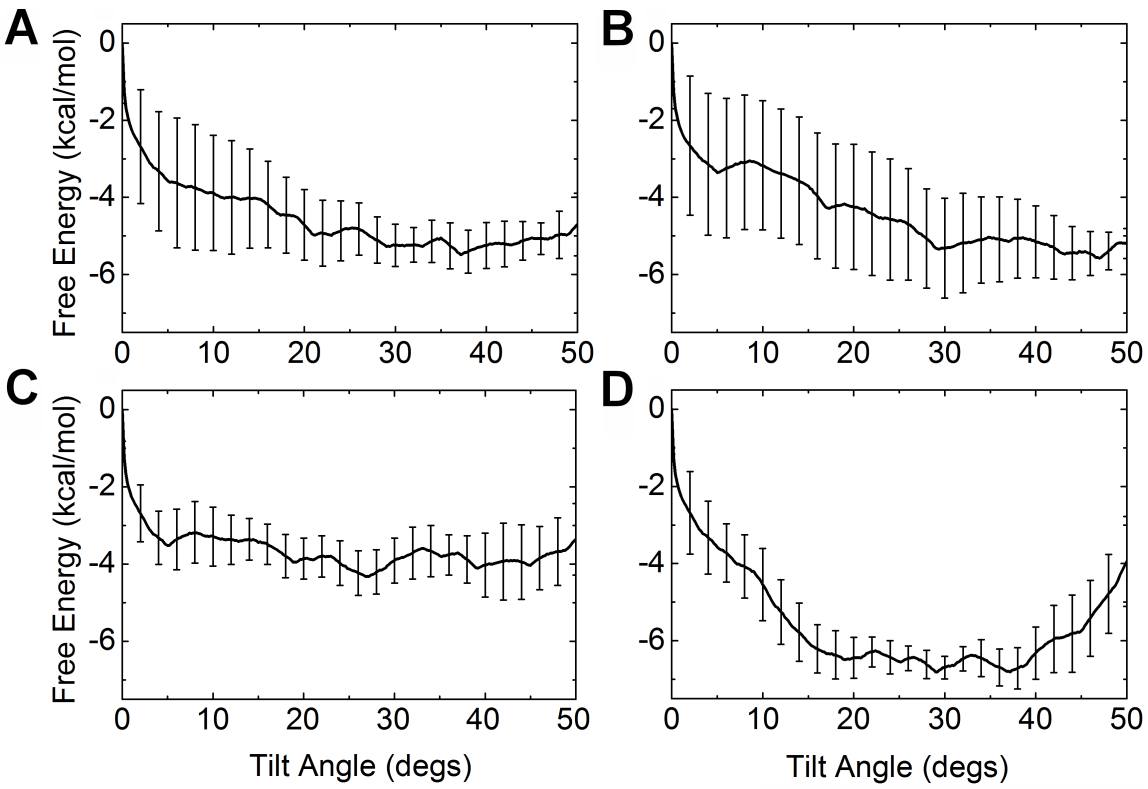

Figure 2.11. The total PMFs of the WALP23/DMPC system as a function of τ with ρ = (A) −150°, (B) −60°, (C) 30°, and (D) 120°. The 11-ns umbrella sampling was performed for each of 26 windows (from τ = 0° to 50° every 2°).

2.3.2 Influence of hydrophobic thickness of bilayers

In addition to L_{TM}, the TM helix orientation is also affected by $L_{bilayer}$. Experimental studies have also used various lipid bilayers with different $L_{bilayer}$ to induce different hydrophobic mismatch conditions (17, 19). To elucidate the effect of $L_{bilayer}$ on TM helix orientation and lipid adaptations, we used POPC bilayers ($L_{bilayer}$ = ~26 Å) (53) for the PMF calculations and compared the results with those in DMPC. In the WALP*n*/POPC systems, only WALP27 is under the positive mismatch condition at $\tau = 0°$. Similar to the DMPC cases, as shown in Figure 2.3 (B) and Table 2.3, τ_{min} increases and the thermally-accessible tilt region becomes wider as L_{TM} increases. However, each TM helix generally shows smaller τ_{min} and $\Delta W(0 \rightarrow \tau_{min})$, and broader thermally-accessible tilt region than in DMPC bilayers, illustrating that the TM helices do respond differently in POPC than in DMPC bilayers. The PMF decomposition in Figure 2.12 clearly shows that tilting up to τ_{min} is mostly driven by $W_{entropy}$ because all WALP peptides except WALP27 are under the negative mismatch condition in POPC bilayers. The increase in the total PMF after τ_{min} well correlates with W_{int}, but the W_{int} contribution appears to be less significant than in DMPC bilayers.

Because of the changes in the hydrophobic mismatch condition and thus in the helix-lipid interaction, the local lipid adjustment of the POPC bilayers is different from that of DMPC. As shown in Figure 2.5 (B), $\Delta L^{adaptation}$ in POPC bilayers generally shows less change than in DMPC bilayers for the same L_{TM}. Compared to DMPC, POPC has the

same head group, but the larger cross-sectional area because the unsaturated acyl chain makes the hydrophobic packing of lipid tails less tightly than the fully-saturated DMPC acyl chains (54). Its more flexible, dynamic nature is attributed to smaller local lipid adaptations in POPC bilayers, which, in addition to its larger $L_{bilayer}$, is sufficient to maximize the hydrophobic match even for WALP27 (Figure 2.7 (B)). Hence, the W_{int} contribution to the total PMF provides less additional driving force for WALP27 tilting than in DMPC bilayer.

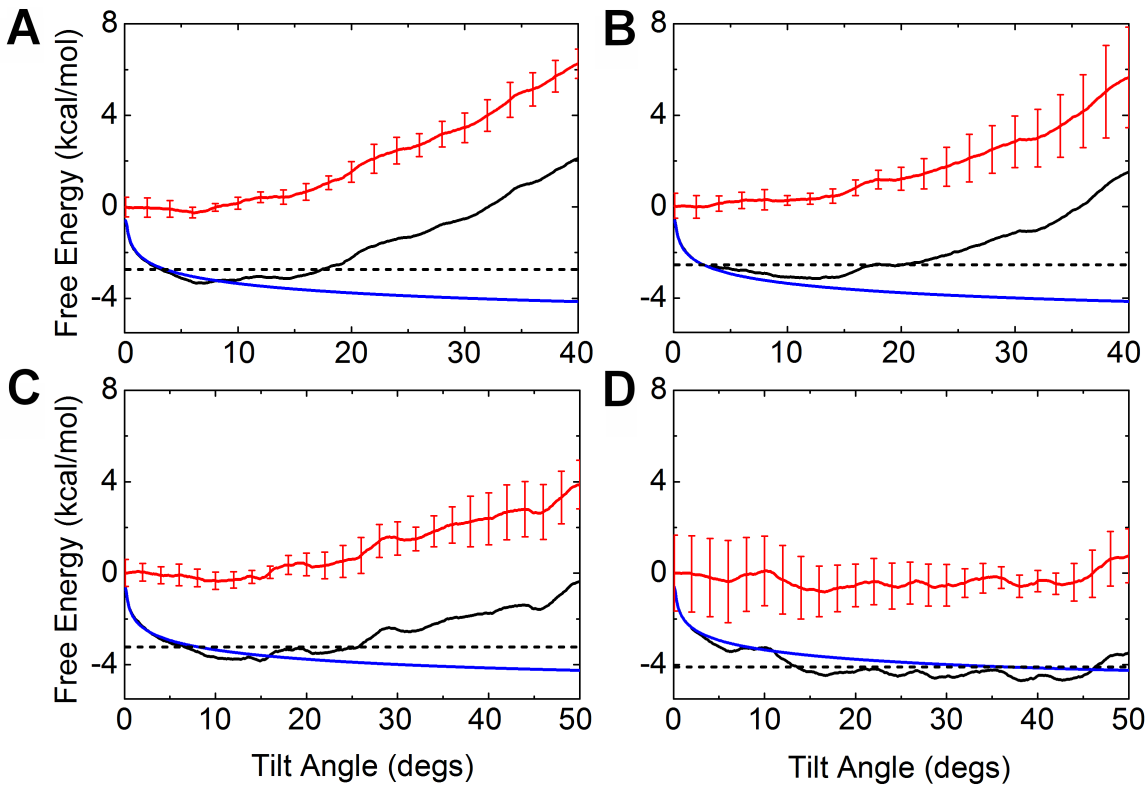

Figure 2.12. Decomposition of the total PMF (*black*) into the helix-lipid interaction (W_{int}: *red*) and the entropic contribution ($W_{entropy}$: *blue*), and the thermally-accessible region (*black dashed*) in (A) WALP16, (B) WALP19, (C) WALP23, and (D) WALP27 in POPC bilayers.

As shown in Figure 2.13, most Trp anchoring residues are positioned around the hydrophobic/hydrophilic interface of the POPC bilayers. Only one Trp residue of WALP16 is below the interface because of its relatively short L_{TM} in POPC bilayers with larger $L_{bilayer}$. Despite of the existence of four Trp anchoring residues at the interface, the WALP*n* peptides do not show any helical deformation probably due to the flexible nature of POPC acyl chains (see WALP19 in Figure 2.8, (A) and (B) for comparison). Z_{Trp} in Figure 2.13 shows only marginal decrease as τ increases, suggesting that the interfacial matching of anchoring residues is dominant throughout TM helix tilting in POPC bilayers and thus each helix has broader thermally-accessible tilt regions than in DMPC bilayers. As shown in Figure 2.14, the interfacial matching is closely related to the tilting direction (i.e., rotation angle) having outward-facing of the Trp sidechains. Note that the tilting direction is similar for each helix in POPC, but different from that of the WALP*n*/DMPC systems. Such difference may arise from the different $L_{bilayer}$ in DMPC and POPC bilayers.

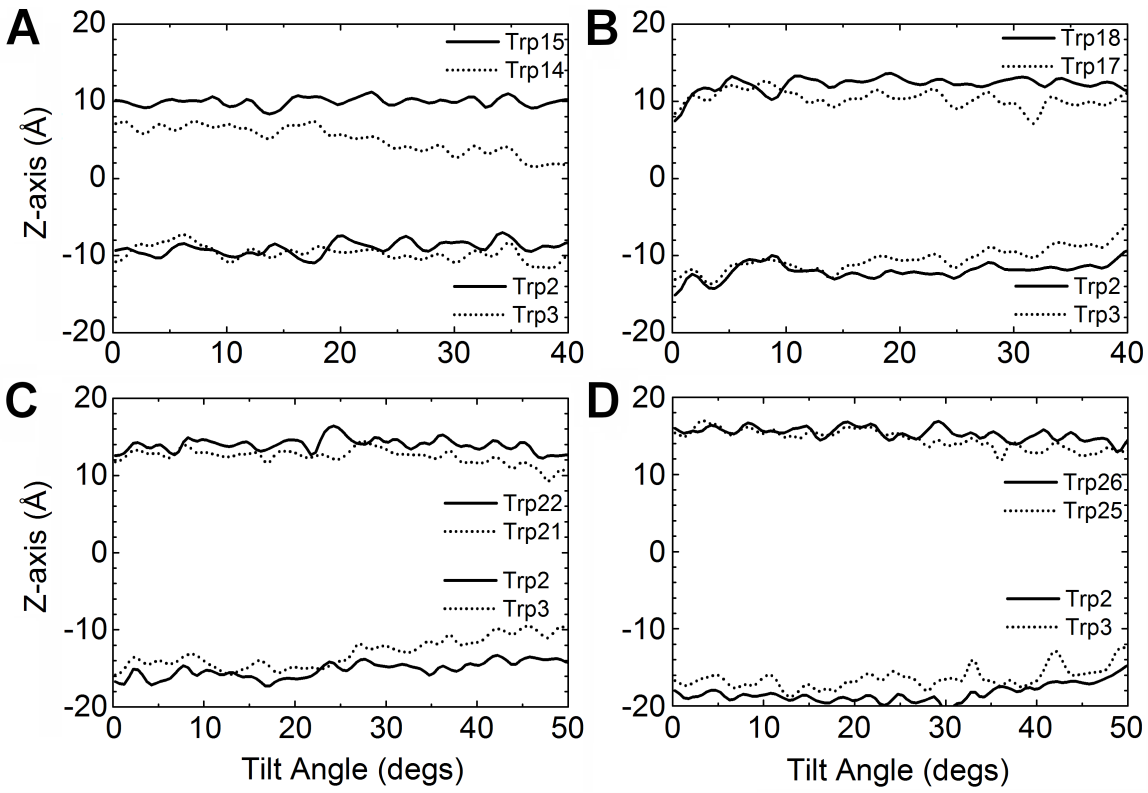

Figure 2.13. Average locations of Trp sidechains as a function of τ in (A) WALP16 (Trps 2, 3, 14, and 15), (B) WALP19 (Trps 2, 3, 16, and 17), (C) WALP23 (Trps 2, 3, 21, and 22), and (D) WALP27 (Trps 2, 3, 25, and 26) in POPC bilayers.

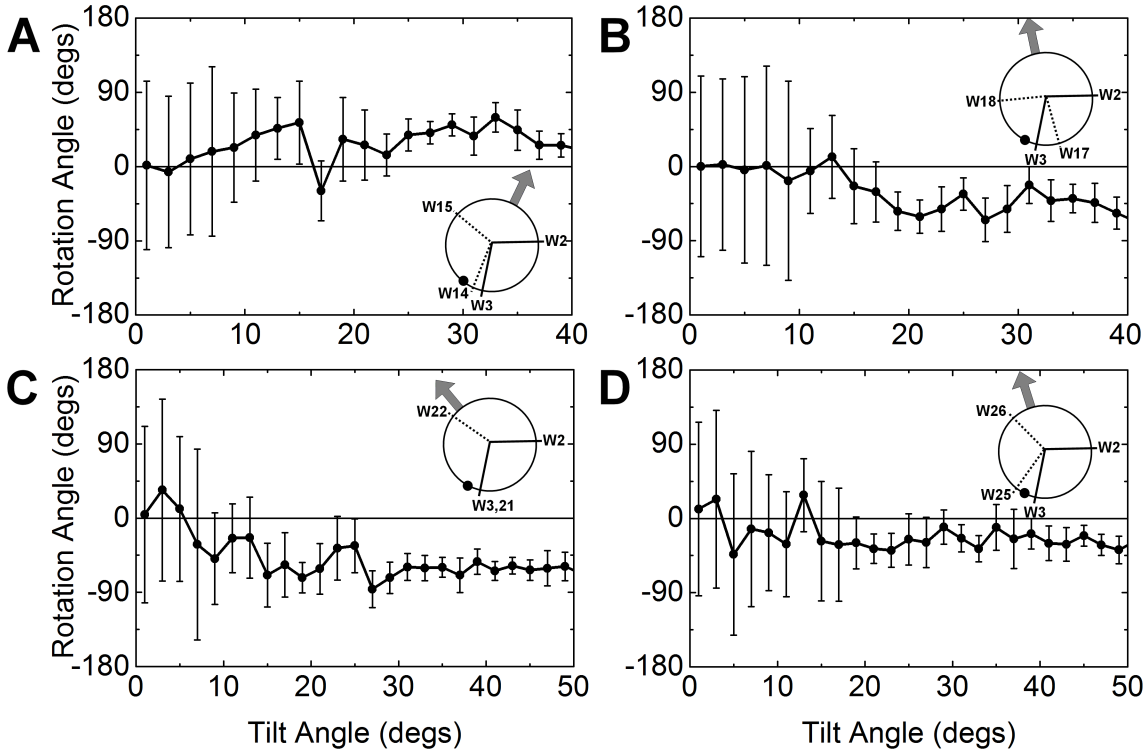

Figure 2.14. TM helix rotation angle (ρ) as a function of τ in (A) WALP16, (B) WALP19, (C) WALP23, and (D) WALP27 in POPC bilayers. The reference atoms, such as Ala^{7} (for WALP16), Leu^{10} (for WALP19), and Leu^{14} (for others), and the tilting direction at τ_{min} are indicated by black circles and gray arrows on the helical view, respectively.

2.3.3 Influence of anchoring residues

A flanking residue of a single-pass TM helix can also influence helix tilt and rotation as well as lipid adaptations (19, 55). To investigate such influences, we used three different anchoring residues (Ala, Lys, and Arg) in addition to Trp in the WALP23/DMPC system for the PMF calculations. Figure 2.3 (C) shows the total PMFs of the *X*ALP23/DMPC (*X* = A, K, W, and R) systems as a function of τ. Interestingly, even though the *X*ALP23 series have the same L_{TM} except AALP23 (Table 2.1), their minimum-PMF tilt angles (Table 2.2) show a direct relationship to the hydrophobicity (56) of its anchoring residues: τ_{min} (RALP23) < τ_{min} (KALP23) < τ_{min} (WALP23) < τ_{min} (AALP23). These results appear to be at odds with the tilt angles estimated from solid-state ^{2}H-NMR experiments (19), showing τ = 4.4° (KALP23) and τ = 5.2° (WALP23). However, it is now apparent that the correct determination of tilt angles using ^{2}H-NMR quadrupolar splitting measurements requires a proper average of rotation angles (24, 25, 35) (It will be discussed in Chapter 3). For example, as mentioned above, the recent fluorescence spectroscopy experiment (35) shows much larger tilt angle of WALP23 (τ = 24° ± 5°) in a DOPC membrane than the tilt angle (τ = 4.4°~8.2°) estimated from solid-state ^{2}H-NMR measurements (17, 19).

The free energy decomposition (Figure 2.15) shows that as the hydrophobicity of anchoring residue increases, there is more W_{int} contribution to TM helix tilting up to τ_{min} in addition to the intrinsic $W_{entropy}$ contribution, and the thermally-accessible tilt region

becomes wider. Such difference is closely related to the local lipid adaptations. As shown in Figure 2.5 (C), $\Delta L^{adaptation}$ disappears around each τ_{min}, and the extent of $\Delta L^{adaptation}$ before τ_{min} is inversely proportional to the hydrophobicity of each anchoring residue. In other words, the W_{int} contribution to TM helix tilting up to τ_{min} arises from the helix-lipid interaction to relieve the hydrophobic mismatch. To avoid exposure of the charged sidechains to the hydrophobic membrane interior and to allow them to interact favorably with the aqueous environment (56), as shown in Figure 2.16, Lys and Arg anchoring residues prefer to be positioned at 3~5 Å above the hydrophilic/hydrophobic interface where Trp residues are generally positioned. These 'snorkeling' behaviors (23, 57) also affect the local lipid adjustment as shown in Figures 2.5 (C) and 2.7 (C). Consequently, the long charged sidechains make more dominant interaction with water (Figure 2.17), so that they have less τ_{min}.

As shown in Figure 2.18, the *X*ALP23/DMPC systems show quite different rotations and thus tilt directions. The large fluctuation in the AALP23 system appears to arise from the flexible dynamics of AALP23 due to a lack of bulky anchoring residue's interaction with membranes. In addition, the large change of ρ and its fluctuation in RALP23 is attributed to the ill-definition of ρ due to slight helix bending at $\tau > 20°$ (Figure 2.8 (C)). The tilting direction of KALP23 ($-114.3° \pm 55.8°$) at $\tau = \tau_{min}$ is well correlated with the rotation angle ($\rho = -109°$) estimated from the solid-state ^{2}H-NMR measurement (19). These results demonstrate that the interaction of Lys and Arg

anchoring residues at the membrane/water interface plays an important role in determining TM helix orientations.

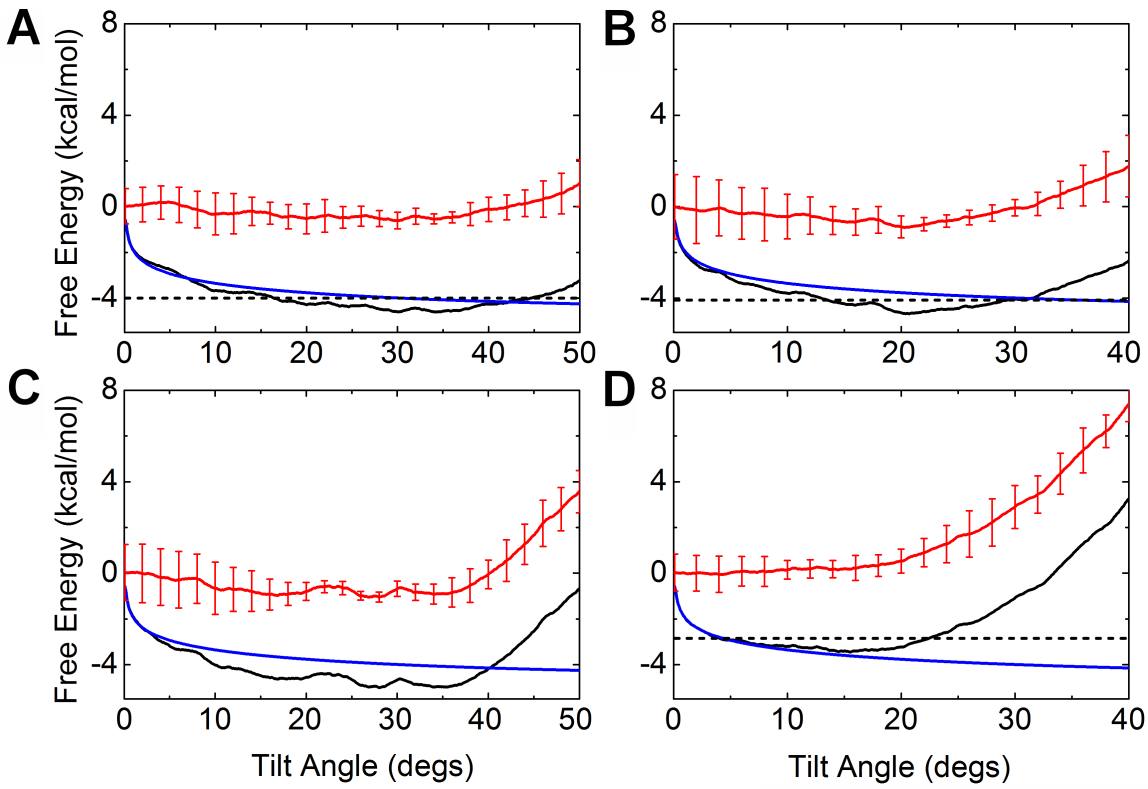

Figure 2.15. Decomposition of the total PMF (*black*) into the helix-lipid interaction (W_{int}: *red*) and the entropic contribution ($W_{entropy}$: *blue*), and the thermally-accessible region (black dashed) in (A) AALP23, (B) KALP23, (C) WALP23, and (D) RALP23 in DMPC bilayers.

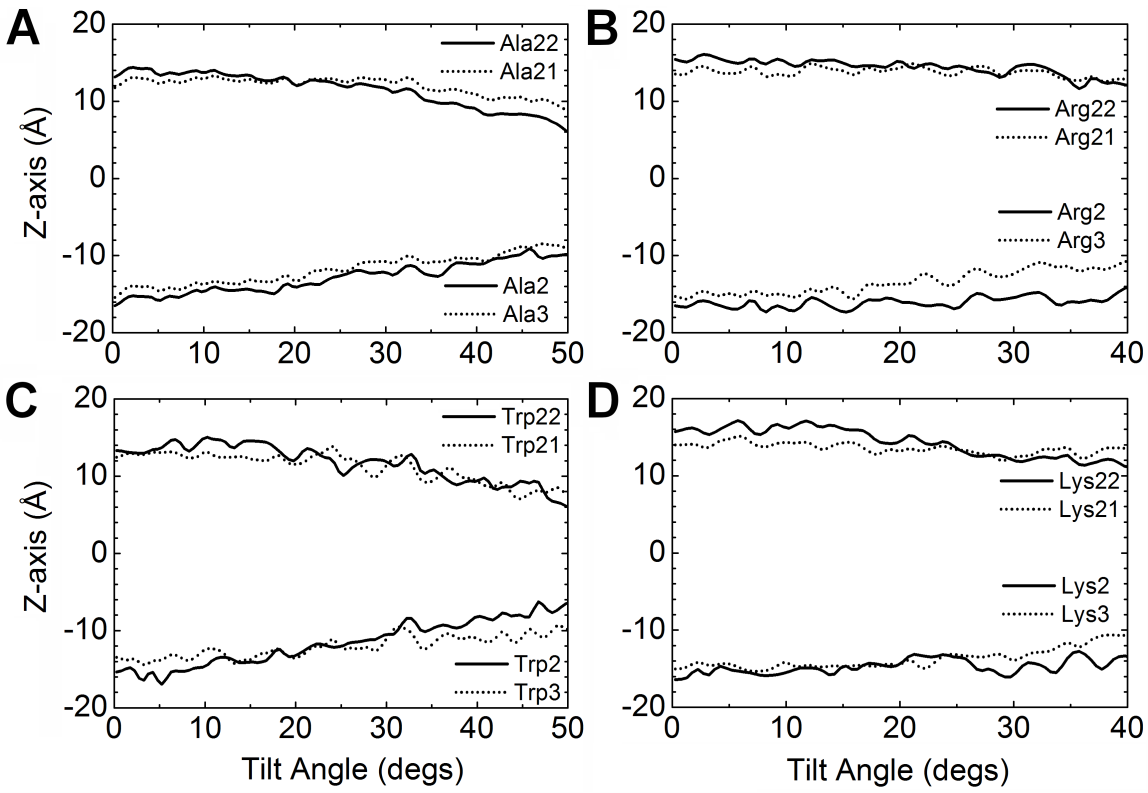

Figure 2.16. Average locations of sidechains of anchoring residues (residue #: 2, 3, 21, and 22) as a function of tilt (τ) in (A) AALP23, (B) KALP23, (C) WALP23, and (D) RALP23 in DMPC bilayers.

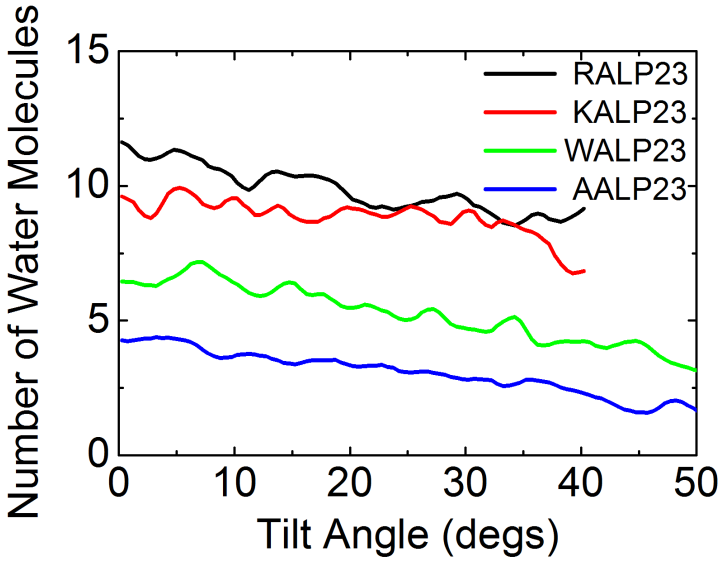

Figure 2.17. The Number of water molecules within 4.5 Å from each anchoring residue as a function of tilt (τ).

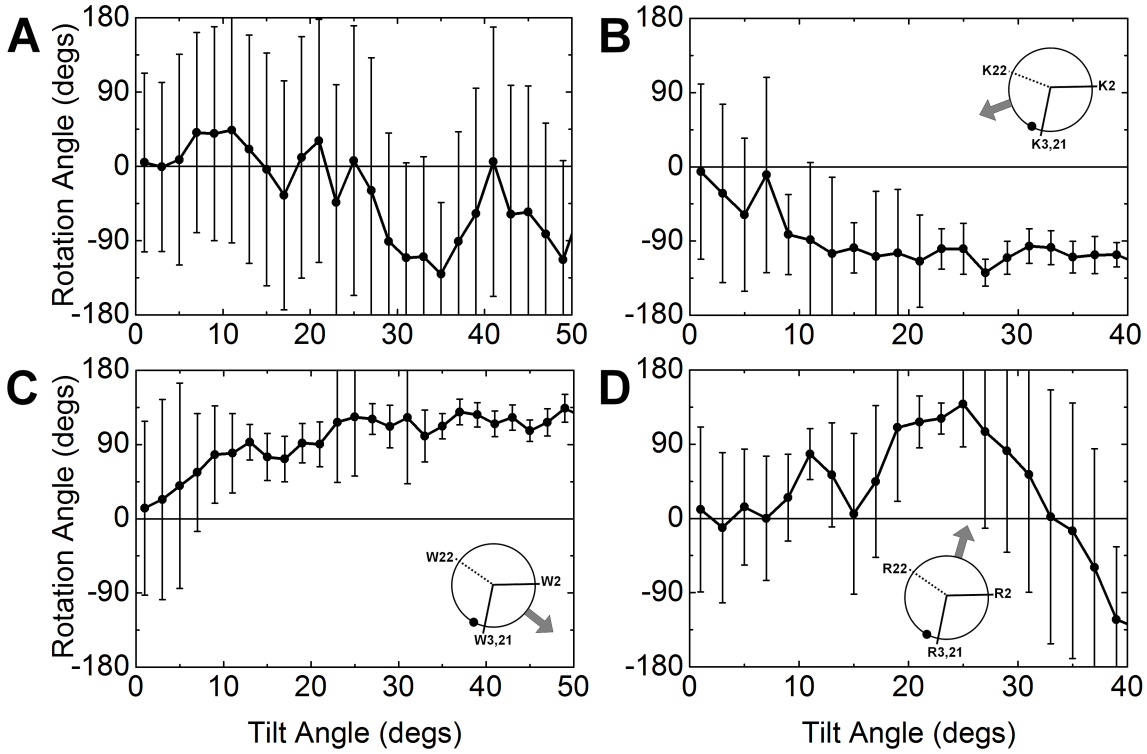

Figure 2.18. TM helix rotation angle (ρ) as a function of tilt (τ) in (A) AALP23, (B) KALP23, (C) WALP23, and (D) RALP23 systems in DMPC bilayers. The reference atom (Leu^{14}) and the tilting direction at τ_{min} are indicated by black circles and gray arrows on the helical view, respectively.

2.4. Conclusions

In Chapter 2, to systematically characterize responses of a single-pass TM helix in terms of its orientation (tilt and rotation) and lipid adaptations under various hydrophobic mismatch conditions, we have performed extensive umbrella sampling MD simulations and calculated the PMFs as a function of TM helix tilt angle (τ) in the WALP*n*/DMPC, WALP*n*/POPC (*n* = 16, 19, 23, and 27), and *X*ALP23/DMPC (*X* = A, K, W, and R) systems (Tables 2.1 and 2.2). The PMF in each system, its decomposition, and trajectory analysis allow us to generalize such responses and the underlying molecular forces.

1. Tilting of a single-pass TM helix in the lipid bilayers is the major response to a hydrophobic mismatch. Regardless of the negative and positive mismatches, the PMFs in all the systems (Figure. 2.3 and Table 2.3) clearly demonstrate that each TM helix prefers to stay around its minimum-PMF tilt angle (τ_{min}) without conformational deformations such as kinks or bending (Figure 2.8).

2. Tilting of a single-pass TM helix up to ~10° is inherent. As shown in Figures. 2.4, 2.12, and 2.15, there is the intrinsic entropic contribution ($W_{entropy}$) to TM helix tilting in a membrane bilayer, which arises from helix precession around the membrane normal. In other words, the accessible orientational space of the helix is reduced as τ decreases, which causes the entropy cost associated with small tilt angles. In particular, its cost up to ~10° is high enough to make the TM helix tilt even under negative mismatch conditions, such as WALP16/19 in DMPC bilayers and WALP16/19/23 in POPC bilayers.

3. The favorable helix-lipid interaction provides additional driving forces for TM helix tilting under a positive mismatch. The helix-lipid interactions (W_{int}) are TM sequence- and length-specific, and indeed vary for different mismatch conditions (Figures 2.4, 2.12, and 2.15). Generally, there is no favorable W_{int} contribution under negative mismatch conditions because of increased stress on the (already) perturbed lipid bilayer as τ increases (Figures 2.5 and 2.7). However, under positive mismatch conditions (WALP23/27 in DMPC bilayers and WALP27 in POPC bilayers), molecular interaction forces to decrease such membrane deformation stress at $\tau < \tau_{min}$ provides additional driving forces to TM helix tilting to τ_{min}.

4. τ_{min} is generally located where there is the hydrophobic match and little or no lipid perturbation under a positive mismatch, as shown in Figures 2.5 and 2.7. It should be stressed that there are the thermally-accessible tilt regions of ~10°–20° in single-pass TM helices (Figure 2.3 (A) and Table 2.3) where a certain extent of a hydrophobic mismatch exists. This observation strongly suggests that the membrane system can have some flexibility to tolerate such a mismatch within a certain threshold by slight lipid adaptations.

5. TM helix rotation (ρ) is dependent on the sequence- and length-specific helix-lipid interaction. In other words, ρ is determined by both the anchoring residue type and the mismatch conditions (Figures 2.10, 2.14, and 2.18). As shown in Figure 2.11, there is a significant dependence of the tilting energetics on ρ. In general, a single-pass TM helix

with bulky anchoring residues can explore various ρ at small τ up to ~10°, but there are significant energy barriers between different ρ regions after τ ≈ 10°. The precise estimation of thermally-accessible rotation angles as a function of τ further requires the two-dimensional PMF calculations as a function of both τ and ρ.

6. Anchoring residues at the hydrophilic/hydrophobic interface can be an important determinant of TM helix orientation. As shown in Figures 2.9, 2.13, and 2.16, it is apparent that anchoring residues, such as Arg, Lys, and Trp, prefer to position at the hydrophilic (lipid head group and water)/hydrophobic interface around τ_{min}, regardless of the negative and positive mismatches. In general, there are no other favorable interactions available in the systems under negative mismatch conditions and thus such interfacial matching appears to be more important. Interestingly, τ_{min} in the *X*ALP23/DMPC systems (Table 2.3) has a direct relationship to the hydrophobicity of its anchoring residues: τ_{min} (RALP23) < τ_{min} (KALP23) < τ_{min} (WALP23) < τ_{min} (AALP23), i.e., more hydrophobic the anchoring residue is, the more TM helix prefers to tilt.

This generalization, based on the extensive PMF calculations and trajectory analysis, provides in-depth insights into the responses of the single-pass TM helix and lipid bilayers to various hydrophobic mismatches. These findings are particularly important because of the abundance of membrane proteins with a single-pass TM helix and their association and conformational changes involved in TM-induced signaling (29, 30). Yet, we need further investigation on the influence of the TM helix-helix interaction on the structure and function of these biologically important systems.

Chapter III

Solid-State NMR Ensemble Dynamics

as a Mediator between Experiment and Simulation[1]

[1] Reused from *Biophysical Journal*, Taehoon Kim, Sunhwan Jo, and Wonpil Im, **100**. 2011. pp 2292-2928. Copyright (2011). with permission from Elsevier Science

Summary

Solid-state NMR (SSNMR) is a powerful technique to describe the orientations of membrane proteins and peptides in their native membrane bilayer environments. The deuterium (^{2}H) quadrupolar splitting (DQS), one of the SSNMR observables, has been used to characterize the orientations of various single-pass transmembrane (TM) helices using a semistatic rigid-body model such as the geometric analysis of labeled alanine (GALA) method. However, dynamic information of these TM helices, which could be related to important biological function, can be missing or misinterpreted with the semistatic model. We have investigated the orientation of WALP23 in an implicit membrane of dimyristoylglycerophospho-choline (DMPC) by determining an ensemble of structures using multiple conformer models with a DQS restraint potential. When a single conformer is used, the resulting helix orientation (tilt angle (τ) of 5.6 ± 3.2° and rotation angle (ρ) of 141.8 ± 40.6°) is similar to that determined by the GALA method. However, as the number of conformers is increased, the tilt angles of WALP23 ensemble structures become larger (26.9 ± 6.7°), which agrees well with previous molecular dynamics simulation results. In addition, the ensemble structure distribution shows excellent agreement with the two-dimensional free energy surface as a function of WALP23's τ and ρ. These results demonstrate that SSNMR ensemble dynamics provides a means to extract orientational and dynamic information of TM helices from their SSNMR observables and to explain the discrepancy between molecular dynamics simulation and GALA-based interpretation of DQS data.

3.1. Introduction

Chapter 3 aims to determine the transmembrane (TM) helix dynamics that is possibly embedded in solid-state NMR (SSNMR) deuterium (^{2}H) quadrupolar splitting (DQS) and to reconcile the long-standing discrepancy between molecular dynamics (MD) simulation and experimental interpretation on TM helix orientation and dynamics. For more than a decade, considerable efforts have been made to understand TM helix orientation and dynamics, and their changes in the context of hydrophobic mismatch, which can be related to the important biological function of membrane proteins (35, 51, 58, 59). In particular, SSNMR has proven to be a powerful technique to describe the orientation of membrane proteins and peptides in their native membrane bilayer environments (60-62). However, dynamic information of these TM helices can be missing or misinterpreted when a static or semi-static rigid-body model is used to interpret the SSNMR observables.

Among various SSNMR observables, the DQS measurement has been used to characterize the orientation of single-pass TM helices, such as WALP and KALP peptides, using the semi-static geometric analysis of labeled alanine (GALA) method (15, 17); n.b., the term "semi-static" is used to broadly include some non-specified motion that is taken into account in the GALA method with an order parameter of less than 1. The TM helix tilt angle interpreted by the GALA method is relatively small (~5° for WALP23 in dimyristoylglycerophospho-choline (DMPC)) (17, 19), which differs

significantly from much larger tilt angles (~30°) observed in MD simulations (22, 24, 25, 27, 28). Recently, to explain the apparent discrepancy between GALA-based interpretation and MD simulation of WALP23, it has been suggested that an average of large-scale rotation motion along the helix axis needs to be considered when interpreting the TM helix orientation from DQS (24, 63, 64). Several approaches including motional averaging of TM helix orientation have been proposed to include TM helix orientational variability (24, 63, 65), but these approaches have fundamental limitations in describing complex TM helix motion from the SSNMR observables, which will be discussed in detail in RESULTS AND DISCUSSION. In general, extracting information about conformational variability directly from NMR and X-ray diffraction is not an easy task because the experimental observables represent time- and ensemble-averages (66-68).

In this work, we determine the TM orientation and intrinsic dynamic information of WALP23 using SSNMR ensemble dynamics (SSNMR-ED). In SSNMR-ED, an ensemble of conformers or replicas is used in parallel MD simulation, and a biased potential (i.e., DQS restraint potential in this work) is applied to minimize the deviation of the ensemble-averaged property from experimental measurements (17). The distribution of WALP23 ensemble structures is characterized as a function of its number of replica; the resulting ensemble structures show better agreement with SSNMR observables with increased number of replicas and much larger TM helix tilt angles with more than one replica. The ensemble structure distribution is validated by calculating a two-dimensional (2D) potential of mean force (PMF) as a function of WALP23's

orientation (TM tilt and rotation). These results demonstrate that SSNMR-ED provides a means to extract the orientational and dynamic information of TM helices from their SSNMR observables. SSNMR-ED also provides a realistic explanation of the discrepancy between MD simulation and GALA-based interpretation of DQS data.

3.2. Computational Method

3.2.1. Defining tilt and rotation angle

The TM helix orientation is defined in terms of its tilt (τ) and rotation (ρ) angles. τ is defined as the angle between the helical principal axis and the unit vector along the *Z*-axis parallel to the membrane normal (13). For ρ, both the internal and external references have to be defined (Figure 2.1). The internal reference is given by the vector pointing from the helical axis to Cα atom of Leu^{10}. Gly^{1} has been widely used to define ρ (mostly when a rigid helix is used) (15, 17, 24), but it is not an appropriate choice for a dynamic system because of its flexibility at the terminal. Instead, we used Leu^{10} to avoid the flexibility problem and for facile comparison with other results based on Gly^{1}, because Leu^{10} is at the almost exact opposite position to Gly^{1} on the helical wheel projection of WALP23. With the unit vector along the *Z*-axis as the external reference, ρ is defined as the angle between the projections of such reference vectors on the plane made by the second and third helical principal axes. The detailed expressions can be found in our previous works (13, 38).

3.2.2. Implicit membrane model

WALP23, acetyl-GWW(LA)$_8$LWWA-methylamide, was constructed in an ideal α-helical conformation (ϕ = −57.8°; ψ = −47.0°). The EEF1/IMM1 (69, 70) implicit membrane model in CHARMM (42) was used to mimic the bilayer membrane environment. The planar implicit membrane was centered at $Z = 0$ with the membrane normal parallel to the Z-axis. The EEF1/IMM1 calculations were prepared using the Implicit Solvent Modeler module in CHARMM-GUI (www.charmm-gui.org) (41).

Solvent/membrane environments play an important role in TM helix orientation. To determine a proper hydrophobic thickness of the implicit membrane, the PMF calculations as a function of WALP23's τ at different rotation angles were performed and compared with our previous results in explicit lipid bilayers (Table 3.1) (27). The initial systems for the umbrella sampling simulations were generated by tilting WALP23 from τ = 0° to 50° by 2° every 100 ps, resulting in a total of 26 windows, at different rotation angles. Each window was then subjected to a 200-ps equilibration and 6-ns production for the PMF calculations with a different hydrophobic thickness from 18.5 Å to 21 Å in 0.5 Å increment. The biased distribution from the umbrella sampling simulations was unbiased by the weighted histogram analysis method (WHAM) (71) to construct the PMF. The PMFs as a function of τ were calculated for every 0.2°, with the energy tolerance of 10^{-6} kcal/mol. The optimal hydrophobic thickness was determined to be 20 Å, which showed the best agreement with the PMFs calculated in the explicit membranes

(27) in terms of root-mean-square deviation (RMSD) and the minimum-PMF τ (Table 3.1 and Figure 3.1). The simulations were performed at 298 K using Langevin dynamics with a 2-fs time step. All bond lengths involving hydrogen were fixed with the SHAKE algorithm (48).

Table 3.1. Root-mean-square deviation between the PMFs[†] calculated from the all-atom simulations and the implicit membrane simulations with various hydrophobic thickness (L_H).

L_H (Å) / ρ (°)	18.5	19.0	19.5	20.0	20.5	21.0
Free	0.78	0.28	0.33	0.24	0.28	0.14
0	0.94	1.07	1.18	1.52	1.56	1.87
90	0.34	0.42	0.43	0.65	1.16	1.36
180	0.33	0.45	0.47	0.61	1.18	1.45
270	0.31	0.38	0.54	0.71	1.06	1.17

[†]The PMFs were calculated as a function of WALP23's tilt angle at four specific rotation angles (ρ) and "Free" represents no rotational restraint applied.

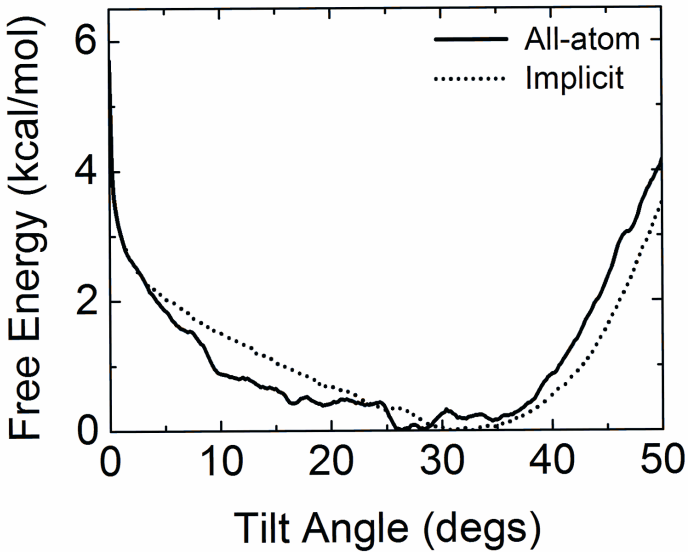

Figure 3.1. PMFs calculated from the all-atom simulation (solid line) and the implicit membrane simulation with 20 Å hydrophobic thickness (dotted line) for free rotation.

3.2.3. Ensemble dynamics with DQS restraint

In the ensemble dynamics simulation, one can perform the simulations with a certain number of replicas (N_{REP}) simultaneously and restrain the ensemble-averaged property ($\left\langle \chi^{\mathrm{calc}} \right\rangle_{\mathrm{ens}}$) from the experimental target value (χ^{exp}). In this work, the target data are the experimental DQS observables ($\chi = \nu$), so that we have developed an ensemble DQS restraint potential (based on our recently-developed $^{1}\mathrm{H}-^{15}\mathrm{N}$ dipolar coupling ensemble restraint potential (72) using the $^{1}\mathrm{H}-^{15}\mathrm{N}$ dipolar coupling restraint potential (73)),

$$U_{\mathrm{DQS}} = N_{\mathrm{REP}} \sum_{i=1}^{N_{\mathrm{DQS}}} k_{\mathrm{DQS}} \left(\left| \left\langle \nu_i^{\mathrm{calc}} \right\rangle_{\mathrm{ens}} \right| - \nu_i^{\mathrm{exp}} \right)^2 \tag{3.1}$$

where N_{DQS} is the number of experimental DQS observables, k_{DQS} is the force constant [kcal/(mol·kHz^2)], and $\left\langle \nu_i^{\mathrm{calc}} \right\rangle_{\mathrm{ens}}$ is

$$\left\langle \nu_i^{\mathrm{calc}} \right\rangle_{\mathrm{ens}} = \frac{1}{N_{\mathrm{REP}}} \frac{3K_{\mathrm{QC}}}{4} \sum_{R=1}^{N_{\mathrm{REP}}} \left(3\cos^2 \theta_i^R - 1 \right) \tag{3.2}$$

where K_{QC} is the quadrupolar coupling constant and θ_i is the angle between the Cα-Cβ bond of labeled alanine (virtually the Cβ−D vectors due to their fast rotation) and the external magnetic field (i.e., the *Z*-axis) as shown in Figure 3.2. K_{QC} was set to 56 kHz, which corresponds to one-third of a typical quadrupolar coupling constant, 168 kHz (74), due to the fast rotation of the methyl group. The total potential energy (U_{TOTAL}) of the ensemble system is then expressed as

$$U_{\mathrm{TOTAL}} = U_{\mathrm{CHARMM}} + U_{\mathrm{DQS}} \tag{3.4}$$

where U_{CHARMM} is the CHARMM potential energy of the ensemble structure. We have checked the numerical accuracy of the ensemble DQS restraint potential; the total energy of all the replicas (not the total energy of each replica) was well converged during the NVE dynamics (75).

The simulation stability depends on the applied force constants and dynamics algorithms (73). Based on our previous studies with other SSNMR structure calculations, we used torsion angle MD (TAMD) simulation (76) because it yields more stable trajectories than Cartesian MD due to a rigid peptide plane. In addition, to generate stable simulation trajectories, the maximum force constant was empirically optimized to be k_{DQS} = 0.4 kcal/(mol·kHz^2). Experimental DQS observables were taken from oriented 0° di-C14:0-PC (17): 9.3 kHz for Ala5, 11.3 kHz for Ala9, 12.8 kHz for Ala13, 12.3 kHz for Ala17, and 2.0 kHz for Ala19.

Starting from an α-helical conformation of WALP23, k_{DQS} was smoothly increased to the maximum value during 10 cycles of 400-ps TAMD simulations, and a final 200-ps TAMD production was performed for structural analysis. To increase the sampling statistics, we repeated the TAMD simulation 100 times with different initial velocity for N_{REP} = 1, 2, 4, 8, 16, and 32. We used a 1-fs time-step for TAMD. A constant temperature of 298 K was maintained by using a simple Berendsen thermostat

(77) in combination with velocity reassignment. The completion of the simulation cycle (i.e., 4.2 ns for each run) took about 4 hours for 8 or smaller replicas, 8 hours for 16 replicas, and 16 hours for 32 replicas running in parallel on 2.33 GHz quad-core Intel workstations; the time increase is mostly due to the communication between the replicas.

To validate the quality of the ensemble dynamics simulation result, we have calculated RMSD [kHz] between $\left|\left\langle \nu_i^{\mathrm{calc}} \right\rangle_{\mathrm{ens}}\right|$ and ν_i^{exp},

$$\mathrm{RMSD} = \sqrt{\frac{1}{N_{\mathrm{DQS}}} \sum_{i=1}^{N_{\mathrm{DQS}}} \left[\left|\left\langle \nu_i^{\mathrm{calc}} \right\rangle_{\mathrm{ens}}\right| - \nu_i^{\mathrm{exp}}\right]^2} \tag{3.4}$$

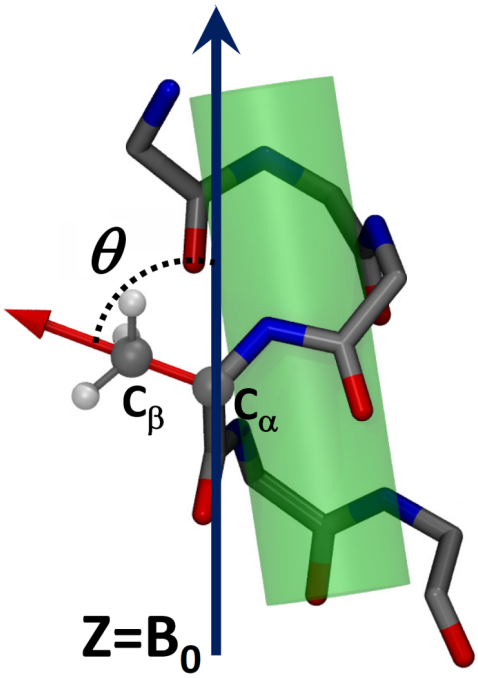

Figure 3.2. Schematic representation of internuclear vectors that is used to calculate instantaneous DQS value. Adapted from Ref. 75

3.2.4. 2D-PMF as a function of tilt and rotation angles

To validate the orientation distribution from the SSNMR-ED simulations, we calculated the 2D-PMF as a function of WALP23's τ and ρ in the EEF1/IMM1 implicit membrane. The initial structures were generated by tilting WALP23 every 2° from 0° to 60°, followed by rotating it every 5° from −180° to 180° at each τ, resulting in a total of 2,263 windows. We performed a 200-ps equilibration and a 10-ns production at each window using the same force constants for the WALP23 tilt and rotation restraint potentials as those used in the explicit membrane PMF calculations (26, 27). We used the same dynamics options used in the SSNMR-ED with TAMD. The biased distribution from the umbrella sampling simulations was unbiased by WHAM (71) to construct the 2D-PMF; the interval of the free energy surface was set to 0.5° and 1.0° along the τ and ρ directions, respectably. The energy tolerance for the WHAM iterations was 10^{-6} kcal/mol.

3.3. Results and Discussion

3.3.1. Orientation of ensemble structures

Figure 3.3 shows the orientation of WALP23 in terms of τ and ρ as a function of N_{REP}. The orientation distribution of the ensemble structures shows a striking difference between $N_{REP} = 1$ and $N_{REP} \geq 2$, while the ensemble-averaged DQS are in close agreement with experimental values in terms of RMSD (Figure 3.4 (A)). The τ and ρ for $N_{REP} = 1$ are 5.6 ± 3.2° and 141.8 ± 40.6° with the DQS RMSD of ~0.8 kHz (Figure 3.4), which agrees very well with the result (τ = 5.5°, ρ = 153.5°, and RMSD = 0.9 kHz) based on the GALA method (17). Interestingly, for $N_{REP} \geq 2$, much larger τ are observed, reaching at ~27° when $N_{REP} = 32$, while ρ remains similar values with increased fluctuation. The ensemble orientation appears to converge when $N_{REP} \geq 8$, demonstrating that it is possible to find a well-converged solution to the applied restraints (78). In addition, Figure 3.4 (A) shows that the DQS RMSD decreases as more replicas are used in SSNMR-ED, illustrating that the generated structure ensemble agrees well with the ^{2}H-NMR experimental DQS data.

3.3.2 How does the structure ensemble show such a dramatic increase in τ with smaller DQS RMSD when $N_{REP} \geq 2$?

Figure 3.5 shows the DQS distribution of each alanine in the ensemble structures as a function of N_{REP}. Surprisingly, each distribution is very broad except when $N_{REP} = 1$; DQS of each alanine covers the whole DQS range (−42 to 84 kHz in Figure 3.4). It is notable that each distribution has the highest population on the negative DQS side and a broad distribution on the positive one. As shown in Figure 3.5, the peaks in the DQS distribution (mostly −34 kHz) correspond to the highest population ($\theta \approx 75°$) in the distribution of θ_i, the angle between the C_α−C_β vector and the *Z*-axis in Eq. 2. It becomes clear that such broad DQS distribution (Figure 3.5) results from the various TM helix orientations in the structure ensemble (Figures 3.3 and 3.6). Thus, the absolute value of the ensemble-averaged DQS becomes smaller (0 ~ 10 kHz), which is measured in the ^{2}H-NMR experiment. It should be stressed that, when $N_{REP} \geq 2$, the calculated DQS of individual structures are different from the experimental one, but their ensemble-averaged DQS (regardless of their signs) show excellent agreement with experimental observables. While we obtain the possible DQS distributions from individual replicas (Figure 3.5), it is not feasible to use them directly as reference values for the current SSNMR-ED simulation scheme.

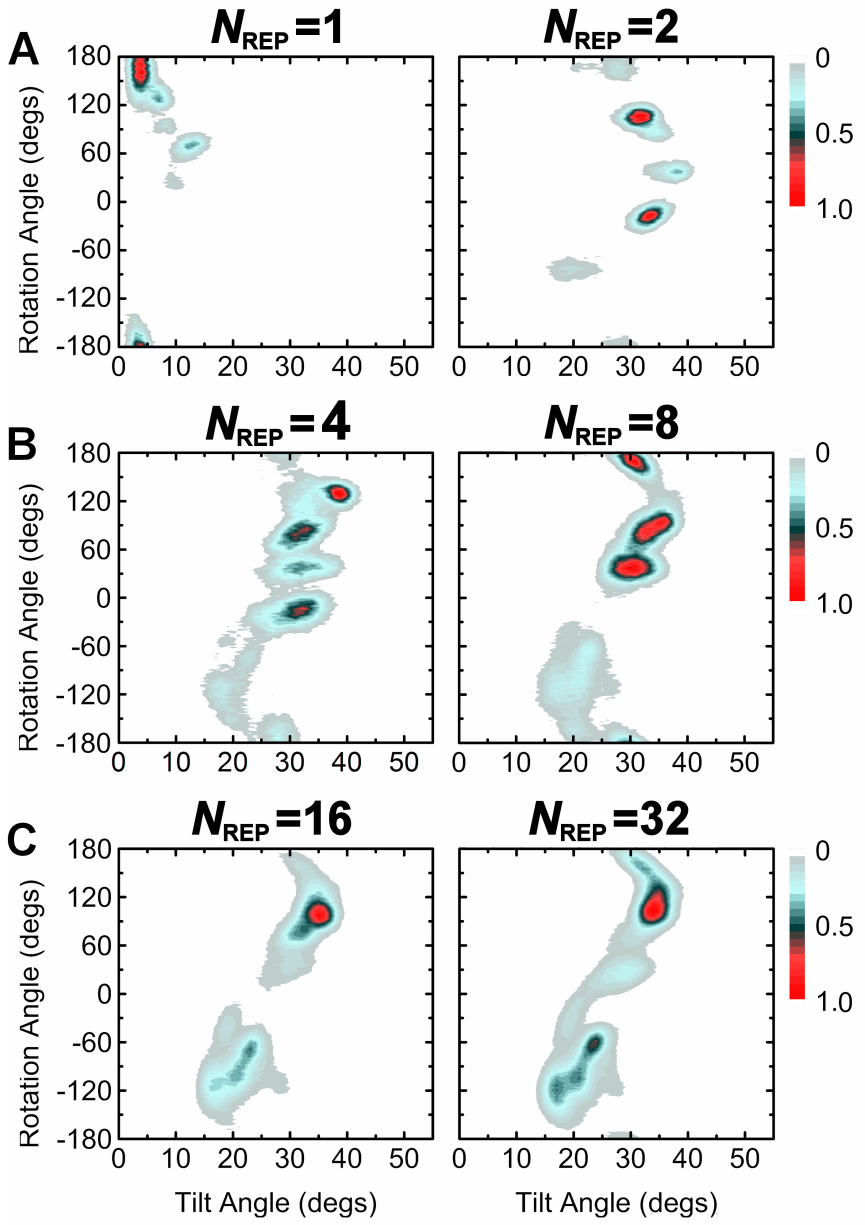

Figure 3.3. Orientation distribution of ensemble structures as a function of N_{REP}. When (A) N_{REP} = 1 and 2, (B) N_{REP} = 4 and 8, and (C) N_{REP} = 16 and 32. The population is normalized by setting the highest value to 1 for easy comparison for each system.

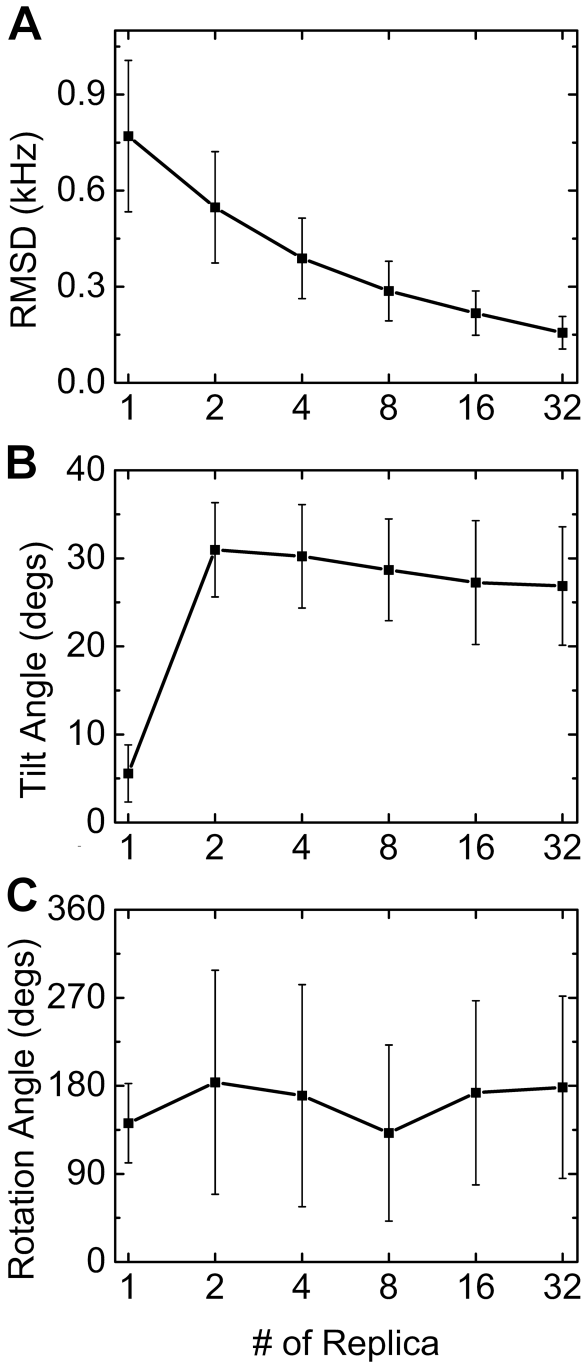

Figure 3.4. (A) RMSD of DQS and (B and C) tilt and rotation angles of WALP23 as a function of N_{REP}.

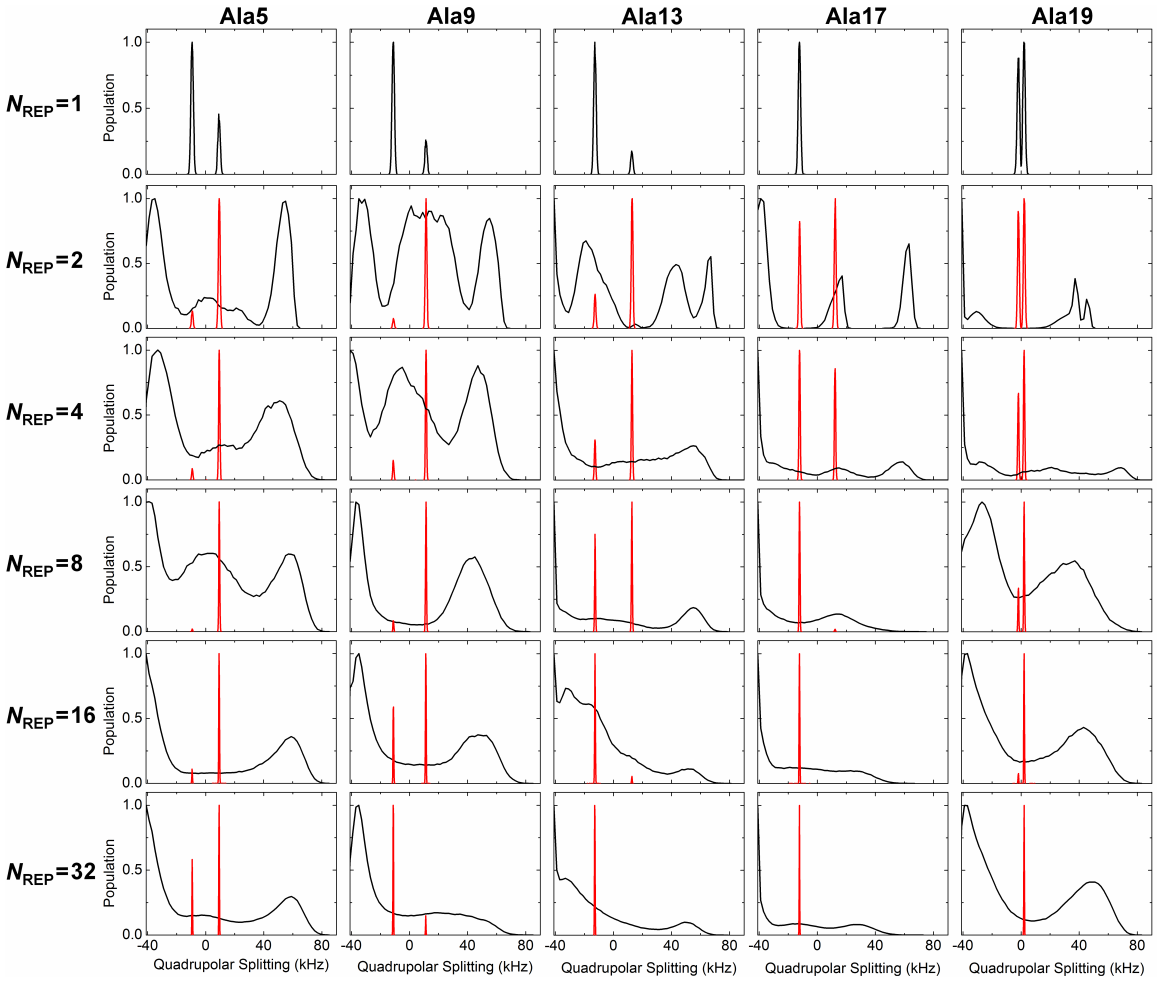

Figure 3.5. Distribution of calculated (*black*) and ensemble averaged (*red*) DQS of each alanine as a function of N_{REP}. In the case of $N_{\mathrm{REP}} = 1$, the ensemble-averaged DQS does not exist. The population is normalized by setting the highest value to 1 for easy comparison for each system.

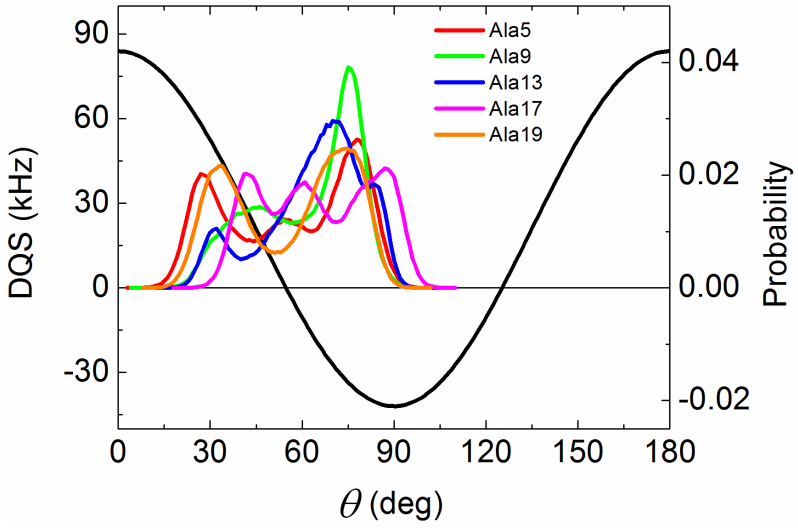

Figure 3.6. DQS value as a function of θ (*black*) and distribution of θ for each alanine when $N_{\mathrm{REP}} = 32$. The possible value of DQS is −42 to 84 kHz.

3.3.3. Evaluation of MD simulation

The SSNMR-ED simulation is different from the standard MD simulation, in that the ensemble structures are generated by a biased restraint potential U_{DQS} in Equation. 3.3. The applied restraints could force the generated structures to be trapped in a physically irrelevant orientation that only satisfies the experimental DQS observables. To validate the orientational variability of the SSNMR-ED structures, we have carried out the 2D-PMF calculation as a function of WALP23's τ and ρ. Such a validation approach in SSNMR-ED is important for two reasons. First, the number of restraints (5 DQSs) in the present SSNMR-ED simulation is not enough to perform reliable cross-validation. Second, a regular MD simulation often suffers from insufficient sampling to obtain a reliable and converged TM helix orientation distribution.

Figure 3.7 (A) shows the resulting 2D-PMF of WALP23 in τ and ρ space. The free energy minimum is at $\tau = 36°$ and $\rho = 112°$, and the thermally-accessible τ and ρ ranges are $27.7° \leq \tau \leq 42.1°$ and $69° \leq \rho \leq 149°$. The thermally-accessible orientations are the regions that have free energies within 0.6 kcal/mol from the minimum-PMF orientation. The thermally-accessible τ region from the 2D-PMF is similar to that from the WALP23 PMFs as a function of τ in explicit DMPC membranes ($14.4° \leq \tau \leq 39°$) (27). Similar to our previous work on a TM β-hairpin (79, 80), as shown in Figure 3.7 (A), there is no significant energy barrier for TM helix rotation when $\tau < 10°$, so that WALP23 can explore various ρ values, but energy barriers along ρ become increased

when $\tau > 10°$.

Figure 3.7 (B) compares the 2D-PMF with the SSNMR-ED ensemble structure distribution with $N_{REP} = 32$ (Figure 3.3). The high population in the ensemble structures well matches with the thermally-accessible region in the 2D-PMF. Most structures from the SSNMR-ED are within 3.0 kcal/mol from the minimum-PMF orientation. This comparison clearly provides support for the notion that the orientation distribution of the ensemble structures from the SSNMR-ED simulations is physically relevant. The secondary structure of individual WALP23 is also well maintained during the SSNMR-ED simulations (data not shown). It should be noted that the SSNMR-ED distribution might not exactly match with the 2D-PMF because the SSNMR-ED distribution is obtained with the DQS restraints and could be deviated from the non-restrained PMF calculation or the standard MD simulation. In this context, the agreement shown in Figure 3.7 (B) is remarkable.

Interestingly, a total of 1.1-μs comparative (multiple) MD simulations (24) have yielded a DQS distribution similar to Figure 3.4 (see Figure 3 in reference 12). This, as an independent comparison, illustrates again that the present SSNMR-ED and the standard MD simulations do capture the physically relevant essential dynamic features of WALP23 in the bilayer membrane environment. Possibly due to sampling or/and force field inaccuracy, the ensemble-averaged DQS from such standard MD simulations show some deviations from the experimental values, with the DQS RMSD of 20 ~ 40 kHz for

individual trajectories and ~6 kHz for combined (ensemble) trajectories. Ironically, such deviations, which are considered too large to be acceptable in the experimental view point (64), provided motivation for the development of various models to consider TM helix dynamics and to seek better agreement with experimental observables, which will be discussed in the next section.

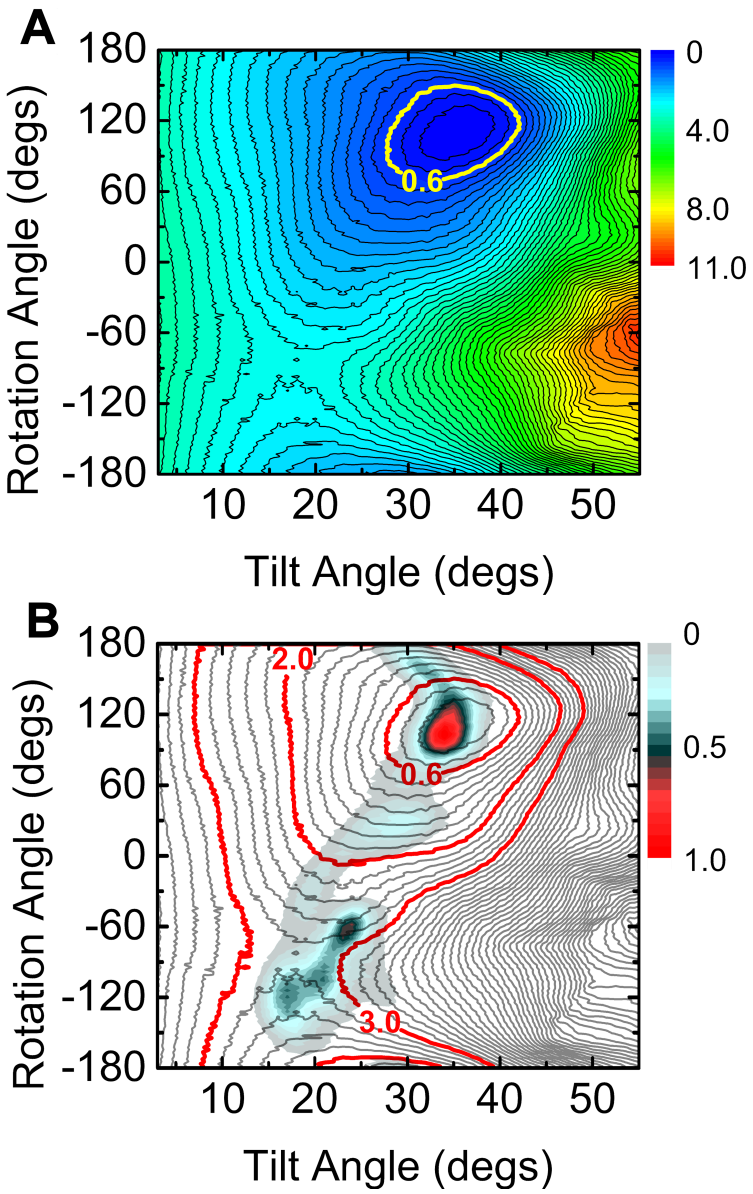

Figure 3.7. (A) 2D-PMF as a function of WALP23's τ and ρ. *Yellow* line indicates thermally-accessible region. (B) Overlap of the ensemble structure distribution (when $N_{\mathrm{REP}} = 32$) and 2D-PMF. The contour lines (*gray*) are drawn every 0.2 kcal/mol and red line indicates 0.6, 2.0, and 3.0 kcal/mol from the PMF minimum.

3.3.4. Various approaches in DQS interpretation

It was a MD simulation study in an implicit membrane that showed a significantly large τ with a considerable fluctuation (τ = 32.7 ± 8.5°) (22), when the GALA-based interpretation of WALP23 was showing τ = 5.5 ± 0.9°. At that time, the discrepancy was attributed to unknown oligomer states of WALP23 in a bilayer (17) because oligomer formation could yield smaller τ (28, 81). Now, there are several approaches/models proposed to resolve the discrepancy by considering the TM helix dynamics and orientational variability in the DQS interpretation. As mentioned at the end of the previous section, based on their long comparative MD simulations, Özdireckan et al. proposed that the small τ of WALP23 estimated by the GALA method could be the result of orientation averaging in the τ and ρ space accessible to WALP23 (24). However, due to an unknown free energy profile in τ and ρ space, it is still a challenging task to use standard MD simulations to determine the WALP23 orientational space and the extent of the orientational variability from which one can reliably calculate the DQS (or other SSNMR) observables. It is this reason why other approaches have been recently proposed to better understand the TM helix dynamics and orientational variability in the interpretation of experimental DQS values, particularly when the observed absolute values of DQS are small (82).

Esteban-Martín et al. used empirical partition free energies of individual amino acid residues from aqueous solution to a membrane bilayer, and calculated the relative

population of WALP23 orientations in a rigid-body movement fashion (65). Such a population allows one to calculate the experimental DQS reasonably well. However, having a relatively high population at small τ appears to be problematic; our previous PMF calculation and its decomposition demonstrate that it is difficult to have small τ (usually < 5°) for a single-pass TM helix in a bilayer environment due to the intrinsic tendency of TM helix tilting, driven by the entropic contribution arising from helix precession (area) around the membrane normal, as indicated in Figures 3.1 and 3.7 (26, 27). Therefore, the relatively high population in small τ, while necessary to reproduce the experimental data when using only positive DQS, could be physically questionable.

To take TM helix dynamic motion into account, additional fitting parameters were also introduced in the framework of the GALA method. In other words, the TM helix orientation distribution in τ and ρ space that satisfies the experimental DQS values are obtained by adjusting the variations of τ and ρ (i.e., $\delta\tau$ and $\delta\rho$), in addition to τ and ρ themselves. Strandberg et al. assume Gaussian distributions around a mean τ and ρ to adjust $\delta\tau$ and $\delta\rho$ (63). This procedure leads to larger values of τ (e.g., 14°−18° for WALP23 in DMPC). Also, the authors analyzed the influence of helix dynamics on the interpretation of DQS data by evaluating different dynamic models of increasing fitting parameter complexity. Very recently, extending this concept, Holt et al. (64) introduced a method using multiple anisotropic constraints, which combines nuclear interactions with different orientations with respect to helical axis. However, the addition of fitting parameters in these approaches could be arbitrary and do not provide clear explanation

for expressing dynamic information and orientational variability from SSNMR observables, since the TM helix orientation distribution may be neither uniform nor Gaussian, illustrated by our results (Figure 3.3). Unlike aforementioned approaches/models, the primary advantage of SSNMR-ED is the ability to generate an ensemble of structures (i.e., TM helix orientation distribution) that satisfies the experimental observables within a reasonable physical (force field) model (Figures 3.3 and 3.7), so that one can extract both TM helix orientation and dynamic information from SSNMR observables.

3.4. Conclusions

In Chapter 3, we have demonstrated that SSNMR-ED provides insights into the interpretation of experimental DQS data, one of the SSNMR observables, and can be used as a means to extract both TM helix orientation and dynamics information. In addition, the SSNMR-ED simulations of WALP23 also provide a realistic explanation of the discrepancy between MD simulation and GALA-based interpretation of DQS data. SSNMR-ED may provide a general strategy for the structural interpretation of the SSNMR observables, and one may apply this knowledge to investigating the influence of the TM helix orientation and its variability on the structure and function of biologically important systems.

Chapter IV

Influence of Hydrophobic Mismatch on Structures and Dynamics of Gramicidin A and Lipid Bilayers[1]

[1] Taehoon Kim, Phillip Morris, Kyu Il Lee, Richard W. Pastor, Olaf S. Andersen, and Wonpil Im, submitted to *Biophysical Journal* (2011)

Summary

Gramicidin A (gA) is a 15-amino acid antibiotic peptide with an alternating L-D sequence, which forms (dimeric) bilayer-spanning, monovalent cation channels in biological membranes and synthetic bilayers. We performed molecular dynamics simulations of gA dimers and monomers in all-atom, explicit dilauroylphosphatidylcholine (DLPC), dimyristoylphosphatidylcholine (DMPC), dioleoylphosphatidylcholine (DOPC), and palmitoyloleoylphosphatidylcholine (POPC) bilayers. The variation in acyl chain length in these different phospholipids provides a way to alter gA-bilayer interactions by varying the bilayer hydrophobic thickness and to determine the influence of hydrophobic mismatch on the structure and dynamics of both gA channels (and monomeric subunits) and the host bilayers. The simulations show that the channel structure varied little with changes in hydrophobic mismatch, and that the lipid bilayer adapts to the bilayer-spanning channel to minimize the exposure of hydrophobic residues. The bilayer thickness, however, did not vary monotonically as a function of radial distance from the channel. In all simulations, there was an initial decrease in thickness within 4–5 Å from the channel, which was followed by an increase in DOPC and POPC or a further decrease in DLPC and DMPC bilayers. The bilayer thickness varied little in the monomer simulations—except one of three independent simulations for DMPC and all three DLPC simulations, where the bilayer thinned to allow a single subunit to form a bilayer-spanning water-permeable pore. The radial dependence of lipid area and bilayer compressibility is also non-monotonic in the first shell around gA dimers due to gA-

phospholipid interactions and the hydrophobic mismatch. Order parameters, i.e., acyl chain dynamics, and diffusion constants also differ between the lipids in the first shell and the bulk. The lipid behaviors in the first shell around gA dimers are more complex than would be predicted from a simple mismatch model, which has implications for understanding the energetics of membrane protein-lipid interactions.

4.1. Introduction

Integral membrane proteins are coupled to their host bilayer through hydrophobic interactions between the proteins' transmembrane domains and the bilayer hydrophobic core (83), and membrane protein function is regulated by changes in the lipid bilayer thickness or intrinsic lipid curvature (12). This regulation of membrane proteins function arises because the energetic penalty for exposure of hydrophobic residues to water, between 25 and 75 cal/(mol·Å^2) (84). Changes in protein conformation that involve the protein's transmembrane domain therefore will cause local changes in lipid packing. In the case of a hydrophobic mismatch (between the length of a protein's hydrophobic transmembrane domain and the thickness of the bilayer hydrophobic core), the bilayer adaptation involves local changes in lipid bilayer thickness, and possibly changes in transmembrane domain orientation (85). Focusing on the changes in bilayer organization, the local bilayer thickness change (protein-induced bilayer deformation) has an associated energetic cost, the bilayer deformation energy (ΔG_{def}) (85, 86). The difference in ΔG_{def} associated with two different conformations (I and II) of the protein of interest is the bilayer contribution to the free energy difference for the conformational transition, $\Delta G_{\mathrm{bilayer}}^{\mathrm{I}\to\mathrm{II}} = \Delta G_{\mathrm{def}}^{\mathrm{I}} - \Delta G_{\mathrm{def}}^{\mathrm{II}}$ (87).

ΔG_{def} has been evaluated using the theory of elastic bilayer deformations (86, 88-92). The theory has been calibrated using changes in gramicidin A (gA) single-channel lifetimes (τ) as a function of bilayer thickness (d_0) (86, 93) and changes in

gA channel appearance rate (f) and τ as a function of membrane tension (σ) (94). The results of these studies show that ΔG_{def} varies as a function of the boundary conditions for lipid packing at the protein/bilayer boundary (88, 90, 91). In addition, the f-σ and τ-σ relations (94) and τ-d_0 relation (93) for gA channels do not conform to predictions based on the elastic bilayer model using bulk bilayer elastic moduli and boundary conditions that minimize ΔG_{def}. The experimental results could be fit by varying the slope (s) of the bilayer/solution interface at the channel/bilayer boundary. This indicates that there are additional constraints on lipid packing, for example the energetic cost of acyl chain tilt (90), which would tend to move s toward 0. Indeed, the τ-d_0 relation could be fit by assuming $s = 0$ (93). Alternatively, the bilayer elastic moduli close to the channel could be larger than the bulk moduli (92). Either modification of the basic elastic bilayer model would be compatible with the τ-d_0 results, but the former modification (constraining s to be 0) is difficult to reconcile with the observed effects of varying the intrinsic curvature (87, 91, 95).

To understand how a channel-bilayer hydrophobic mismatch alters the local lipid structure and dynamics, we used molecular dynamics (MD) simulation to explicitly probe the radial bilayer deformation profile and evaluate the lipid fluctuations, which allows for the determination of "local" compressibility moduli. The radial dependence of lipid organization and dynamics were not extensively investigated in previous MD simulations on gA channels in lipid bilayers (96-99) because the number of lipid molecules was insufficient (usually 10 lipids/gA monomer, or one shell) to explore gA-lipid bilayer interaction that might propagate over several shells. To explore the influence of

hydrophobic mismatch on the structure and dynamics of gA bilayer-spanning dimers and monomeric subunits, as well as the lipids in the vicinity of the channel or subunit, we therefore performed MD simulations on gA dimers and monomers embedded in bilayers of different thickness with 4 lipid shells. The simulations were carried out in dilaurylphosphatidylcholine (DLPC), dimyristoylphosphatidylcholine (DMPC), dioleoyl-phosphatidylcholine (DOPC), and palmitoyloleoylphosphatidylcholine (POPC) bilayers with the recently developed CHARMM36 (C36) lipid force field (100).

The influence of hydrophobic mismatch on the structure and dynamics of gA bilayer-spanning dimers and monomeric subunits were characterized in terms of the root mean squared deviation (RMSD), hydrogen bonding patterns, orientation (tilt and rotation), Trp side chain orientation, and relative position in bilayers. We also calculated key lipid properties— hydrophobic thickness, per-lipid surface area, compressibility, acyl chain order parameter, and lateral diffusion coefficient—as functions of radial distance from the channel and discuss them in terms of the influence of hydrophobic mismatch on lipid bilayer structure and dynamics..

4.2. Computational Methods

Using the *Membrane Builder* module (39, 40) in CHARMM-GUI (www.charmm-gui.org) (41), the gA dimer structure from PDB:1JNO (101) with added pore water molecules was inserted into four different lipid bilayers with 180 DLPC, DMPC, DOPC, and POPC molecules (Figure 4.1), which corresponds to about 4 lipid shells around the channel. The monomeric subunit from the gA dimer was inserted into one leaflet and 5 more lipid molecules were added into the other leaflet. 0.15 M KCl was used for all simulations. Figure 4.2 shows a snapshot of such gA dimer and monomeric subunit systems in the lipid bilayers. Each system was replicated and assigned different initial velocities to generate three independent simulation systems for each type of lipid bilayer, yielding a total of 24 systems. Table 4.1 summarizes the system information.

All calculations were performed in the NPT (constant particle number, pressure and temperature) ensemble (50) at 303.15 K using the biomolecular simulation program CHARMM (42) with the CHARMM all-atom protein force field (43) including a modified version of dihedral cross-term correction (CMAP) (referred to as dCMAP) (44, 102), the latest C36 lipid force field (100), and a modified TIP3 water model (45). A time-step of 2 fs was used with the SHAKE algorithm (48).

Each initial system was equilibrated using 50-ps NPAT (constant particle number, pressure, *XY* area, and temperature) dynamics followed by 325-ps NPT dynamics with the nonbonded and dynamics options in the *Membrane Builder* input; the van der Waals interactions were smoothly switched off at 10–12 Å by a force-switching function (103)

and the electrostatic interaction were calculated using the particle-mesh Ewald (PME) method (104) with a mesh size of ~1 Å for fast Fourier transformation, $\kappa = 0.34$ Å^{-1}, and a sixth-order B-spline interpolation. After equilibration, 100-ns production run was performed for each system.

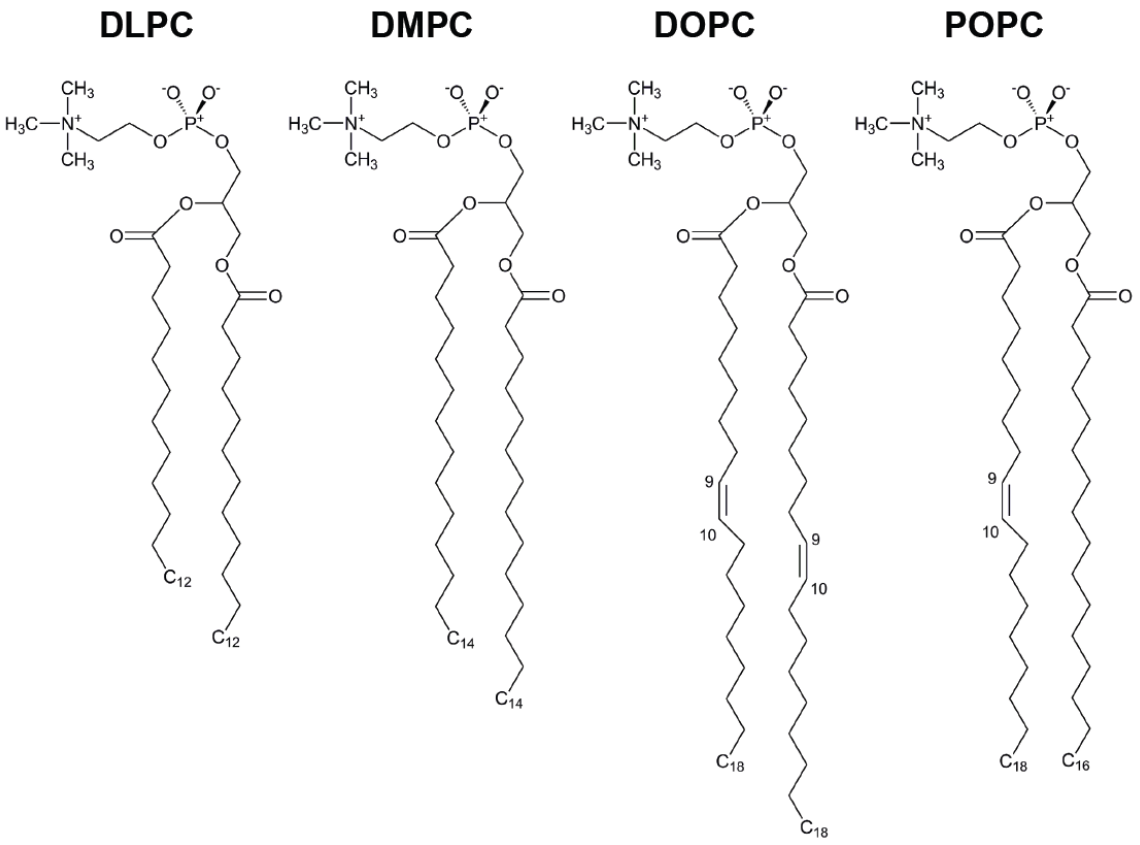

Figure 4.1. Structural representations of phospholipid molecule used in the current MD simulations. (from left to right) DLPC, DMPC, DOPC, and POPC lipid molecule, respectively.

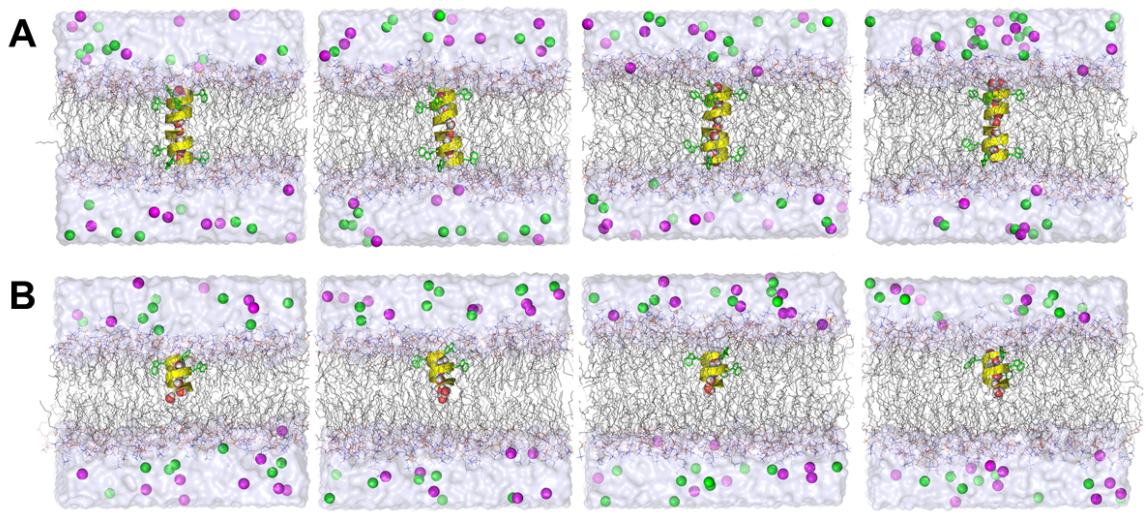

Figure 4.2. Snapshots of (A) dimer and (B) monomeric subunit systems in (from left to right) DLPC, DMPC, DOPC, and POPC bilayers. The gA dimers and monomers are colored *yellow* with the Trp residues *green*; the lipids have *blue* carbons. Pore water molecules are represented as spheres, K^+ and Cl^- are *purple* and *green*, and bulk water molecules is light *blue*.

Table 4.1. System information

Lipid	System Size[1]	Lipid		Ions		Water
		Top	Bottom	K^+	Cl^-	
DLPC	74 × 74 × 70	90	90 (95)[2]	15	15	7,394
DMPC	76 × 76 × 70	90	90 (95)	16	16	6,949
DOPC	80 × 80 × 70	90	90 (95)	18	18	6,802
POPC	80 × 80 × 70	90	90 (95)	18	18	6,670

[1]The system size is given by $L_X \times L_Y \times L_Z$ (in Å), where L_X, L_Y, and L_Z correspond to the length of the system along the *X*, *Y*, and *Z*-axis respectively.

[2]5 lipid molecules are added for the monomer systems.

4.3. Results and Discussion

4.3.1. Influence of hydrophobic mismatch on gA structure and dynamics

Both the bilayer-spanning dimers (channels) and the monomeric subunits were stable for the duration of the simulations. RMSD from the PDB:1JNO structure for the dimers were less than those for the monomers (Figure.4.4 (A)). The number of hydrogen bonds in the dimers (Figure 4.4 (B)) mostly varied between 22 and 26 (the maximum possible), with an average of 25 and occasional transitions to lower numbers. Except in the DOPC bilayers, we observed transient increases in the RMSD for the dimers, which were correlated with the loss of hydrogen bonds —usually caused by one of ethanolamide (EAM) groups swinging out from the channel (102) (Figure 4.5). K^+ binding to the carbonyl oxygens at the channel entrance also caused slight increases of dimer RMSD. The number of hydrogen bonds in the monomers varied between 6 and 10 (the maximal possible), with an average of 8 and occasional transitions to lower numbers. The average number of residues per turn was 6.28–6.29 (compared to 6.3 from PDB:1JNO structure (101)), the average rise per turn was 4.51–4.57 Å (compared to 4.7 ± 0.2 Å in the PDB:1JNO structure and also deduced from X-ray diffraction (105)). There were no significant differences among the dimer structures in different lipid bilayers. The gA channel structure is quite rigid, independent of the lipid bilayer type, and the dimer is more rigid than the monomer.

To explore the gA orientation and dynamics in the different bilayers, we

determined the dimers' and monomeric subunits' average tilt (θ) and rotation (ρ), see definition in Figure 4.3 (27)). To define ρ, Cα atom of Trp9 in one subunit was used as a reference atom. The θ distribution followed the hydrophobic mismatch concept (Figure 4.6 (A)). That is, to maximize the hydrophobic match between the channel and bilayer, θ decreases as the bilayer hydrophobic thickness increased: 14.5 ± 6.3° (DLPC) < 12.2 ± 6.2° (DMPC) < 9.1 ± 4.6° (DOPC) ≈ 8.9 ± 5.2° (POPC). In contrast, there were no significant differences among the monomeric subunits' θ in different lipid bilayers (Figure 4.7 (B)) due to it being free-floating in one leaflet (see below). Except in DLPC bilayers, ρ had a slight preference for –90°, which is the tilt direction between Trp13 and Trp15 (Figures 4.7 and 4.8). The ρ distributions, however, were much broader than those observed in single-pass TM α-helices (e.g., WALPs and VpuTM) (27, 106, 107) because of gA's small θ.

Knowing θ, we can compare our results with experimental determinations. The dynamic extent of (mis)alignment between the molecular *Z*-axis and the membrane normal is characterized by the time averaged order parameter, $S_{zz} = \left\langle 2\cos^2(\tau) - 1 \right\rangle / 2$. S_{zz} for the gA channel backbone is 0.92–0.93 in DMPC bilayer (108-110). Figure 4.6 (C) shows the S_{zz} distributions: 0.89 ± 0.09 (DLPC), 0.91 ± 0.08 (DMPC), 0.95 ± 0.05 (DOPC), and 0.94 ± 0.07 (POPC). The average S_{zz} from MD simulations in DMPC is excellent agreement with experimental measurements. Notably, though gA channels do respond to a hydrophobic mismatch by changing their θ , the extent of the response is

modest compared to those observed in single-pass TM α-helices (e.g., VpuTM: 35° in DLPC to 18° in DOPC and WALPs: 12° of WALP19 to 28° of WALP23 in DMPC) (27, 106, 107). The different behaviors are presumably due to the four Trp residues in each monomer and their strong preference to be at the bilayer's hydrophobic/hydrophobic interface (26).

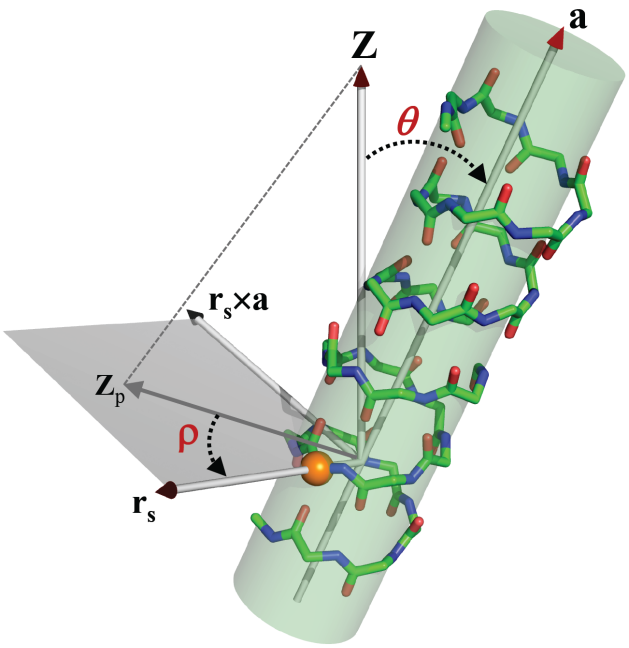

Figure 4.3. Definition of tilt (θ) and rotation (ρ) angle of the gA channel. θ is defined by the angle between the helical principal axis (**a**) and the unit vector along the Z axis. ρ is defined by the angle between the projects of the *Z* axis (**Zp**) and the internal reference vector ($\mathbf{r_s}$) on the plane perpendicular to the helical principal axis. (*Orange sphere*) Cα atom of Trp9 residue as an internal reference atom.

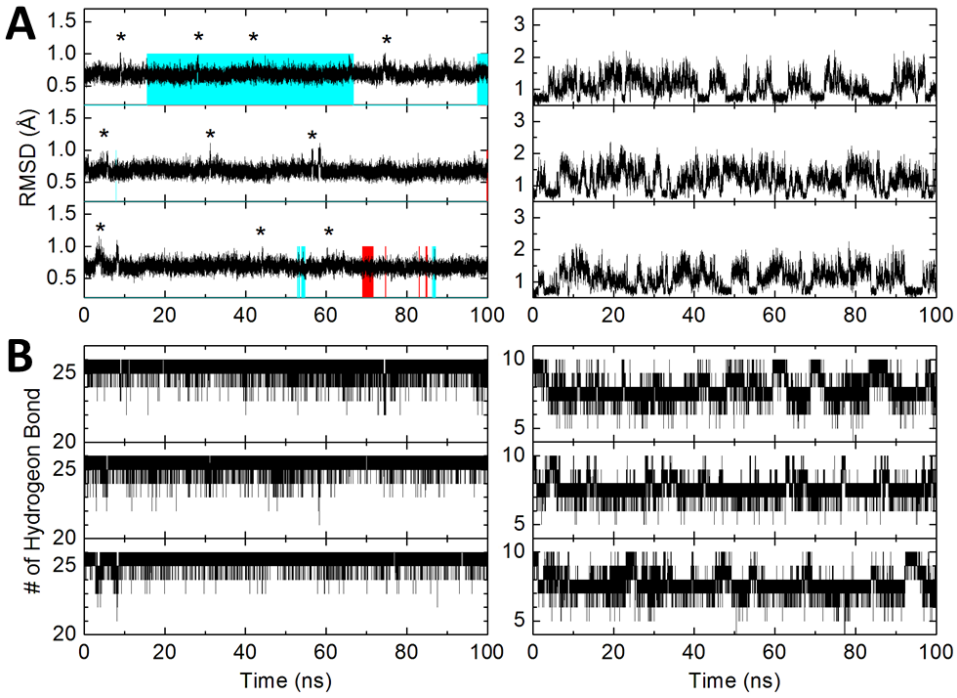

Figure 4.4. (A) RMSD time series for a gA dimer (left) and the monomeric subunit (right) in a DOPC bilayer. Cyan and red colored region represents the binding of K^+ at the upper (*cyan*) and lower (*red*) pore entrance. EAM swing motions are marked by *. (B) The number of hydrogen bonds in the dimer (left) and the monomeric subunit (right) in a DOPC bilayer.

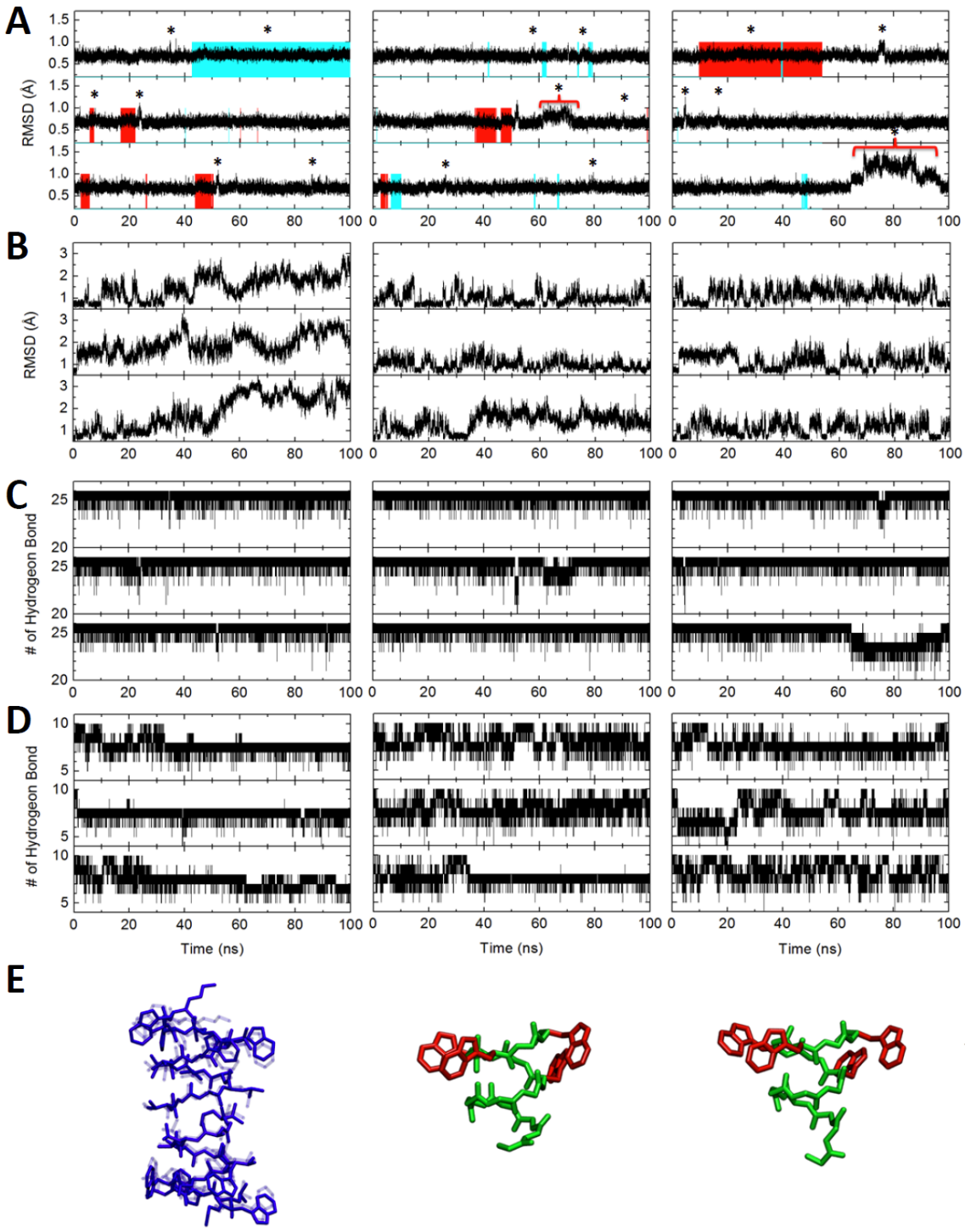
A
RMSD (Å)
B
RMSD (Å)
C
# of Hydrogeon Bond
D
# of Hydrogeon Bond
Time (ns)
Time (ns)
Time (ns)
E

Figure 4.5. (A) RMSD time series of gA dimer and (B) monomer in (from left to right) DLPC, DMPC, and POPC bilayers. Cyan and red colored region represent binding of K^+ at upper (*cyan*) and lower (*red*) pore entrance. EAM swing motions are marked as *****. The number of hydrogen bonds of (C) dimer and (D) monomer in (from left to right) DLPC, DMPC, and POPC bilayers. (E) (left) EAM swing motion of dimer (transparent blue represent the PDB structure and (middle and right) two monomers with 10 and 5 hydrogen bonds, respectively.

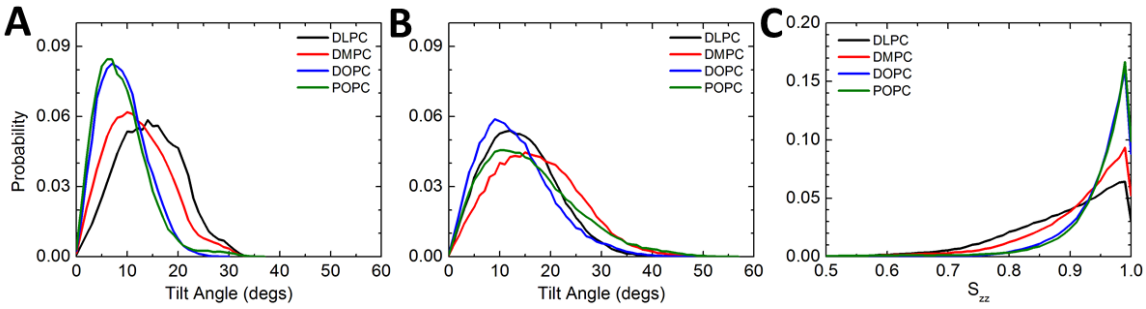

Figure 4.6. Tilt angle distributions of (A) a gA dimer and (B) a monomeric subunit in different lipid bilayers. (C) S_{zz} distribution of a gA dimer in the different bilayers. The results for each system are averages over the three simulations.

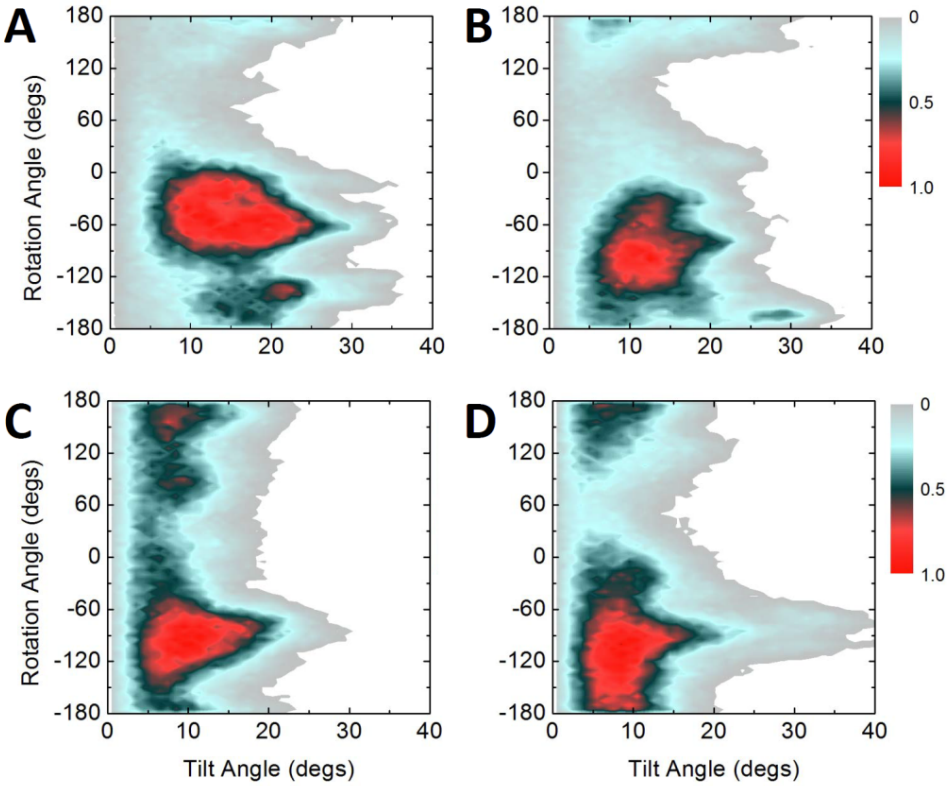

Figure 4.7. Tilt and rotation angle distribution of gA dimers in (A) DLPC, (B) DMPC, (C) DOPC, and (D) POPC bilayers.

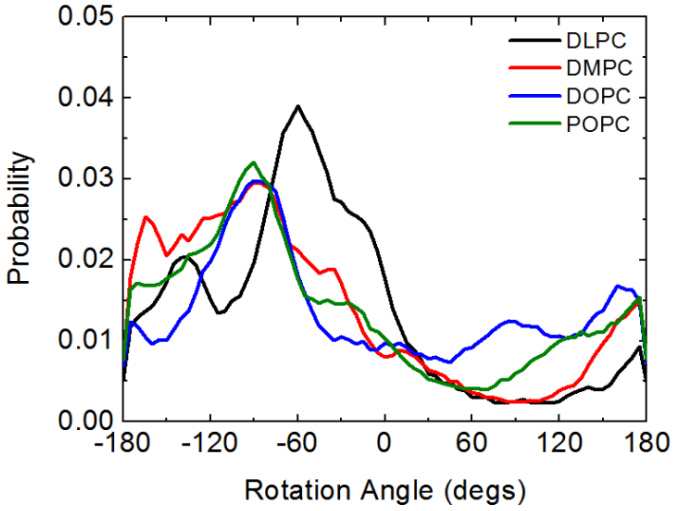

Figure 4.8. Rotation angle distribution of gA dimers in the different bilayers.

To further explore the effect of hydrophobic mismatch on the channel structure, we examined the distributions of the Trp dihedral angles χ_1 and χ_2 (Figures 4.9 (A) and 4.10). Trps 11, 13, and 15 have a single predominant dihedral angle ($\chi_1 \approx -60°$, $\chi_2 \approx -80°$), and the distribution of rotameric states does not vary systematically with the changes in the phospholipid acyl chain (bilayer thickness). As found previously (97, 102), Trp9 was much more mobile than the other Trps, presumably because Trp9 is more deeply buried and therefore not so strongly coupled to hydrogen bond acceptors at the bilayer/solution interface. Consistent with this interpretation, Trp9 in the monomers (Figures 4.9 (B) and 4.11) was less buried and less mobile.

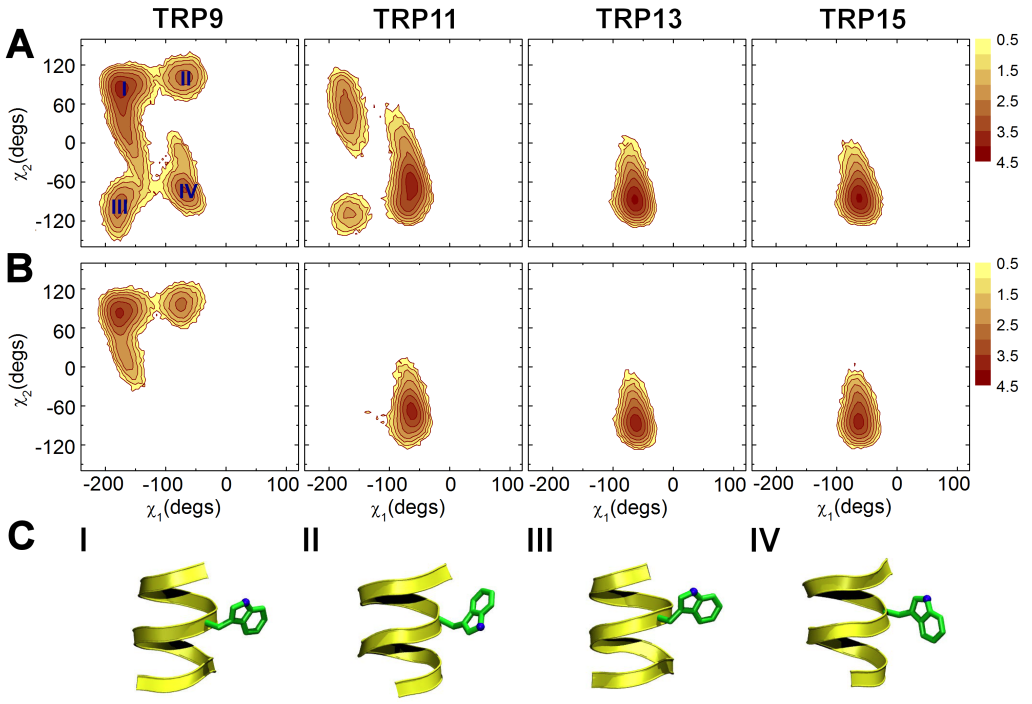

Figure 4.9. The Trp dihedral angles χ_1 and χ_2 of (A) gA dimer and (B) the monomeric subunits in DOPC bilayers. The contours/colors represent the number of counts per 5° square bin on a log 10 scale. (C) Molecular representation of each Trp9 rotamer state. The gA monomer is colored yellow and Trp9 green. Nitrogen atoms are represented as blue sphere. The results for each system are averages of the three simulations.

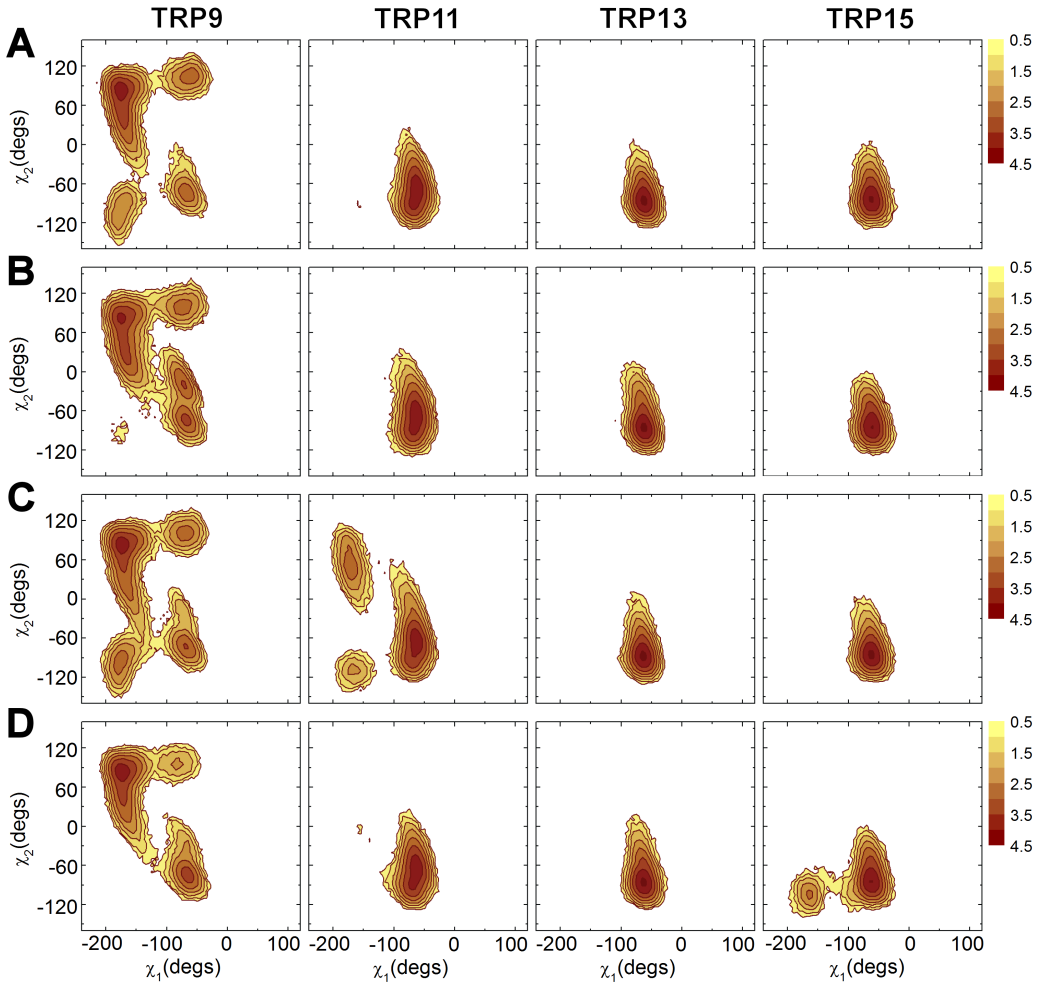

Figure 4.10. The Trp dihedral angles χ_1 and χ_2 of dimer in (A) DLPC, (B) DMPC, (C) DOPC, and (D) POPC bilayers. The contours/colors represent the number of counts per 5° square bin on a log 10 scale.

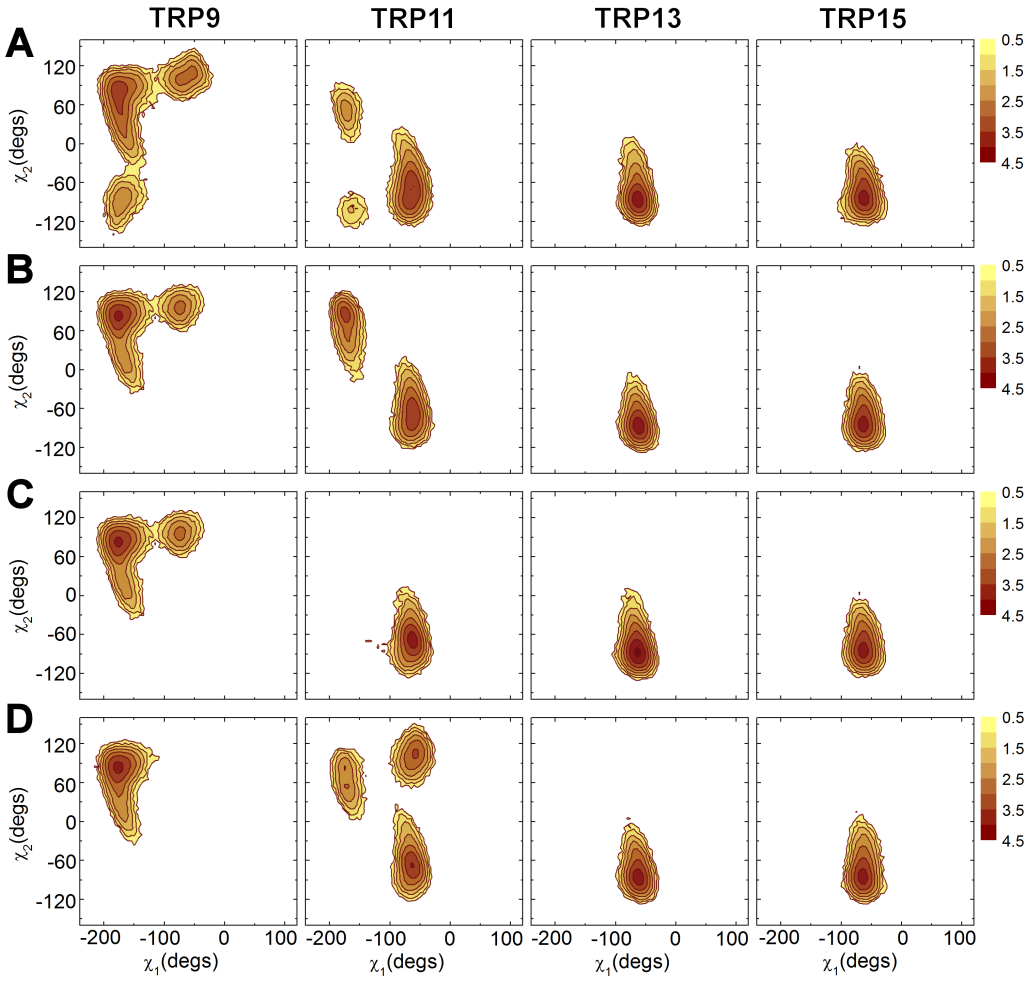

Figure 4.11. The Trp dihedral angles χ_1 and χ_2 of monomer in (A) DLPC, (B) DMPC, (C) DOPC, and (D) POPC bilayers. The contours/colors represent the number of counts per 5° square bin on a log 10 scale.

Despite the lower Trp9 mobility in the monomeric subunits, the overall monomer conformations were more dynamic than the dimer conformations (Figure 4.5), and the monomers moved more freely in the hydrophobic core region of bilayers (see below). The monomeric subunits usually "floating" at the bilayer/solution interface (see Figure 4.12 for the behavior in DOPC and POPC bilayers), reflecting fewer constrains imposed by the bilayer. The DLPC and one of DMPC systems were exceptions, as the monomeric subunits moved toward the bilayer center ($Z = 0$) (Figure 4.12 (A)), to form monomeric, metastable water-permeable channels after ~40 ns of simulation time (Figure 4.12 (B)). The Trps on one end of these monomeric channels remained at the hydrophobic/hydrophilic interface and pull their surrounding lipid molecules down as the monomer moved toward the bilayer center. The formyl group makes hydrogen bonds with interfacial moieties in the opposite leaflet, and the lipid bilayer close to the subunits is grossly deformed. In DOPC and POPC bilayers, which have greater hydrophobic thickness than DLPC and DMPC bilayers, the monomer subunit does not show such a movement (Figure 4.13)

The bilayer-spanning monomers are water permeable. To quantify the water permeability, we traced the *Z*-coordinates of all the water molecules that visit the pore region of monomer, a complete water permeation (+1 into the +*Z* direction and –1 into the –*Z* direction) was recorded only if a water molecule moves from $Z = –12$ Å to 12 Å or vice versa (Figure 4.12 (C)). This may explain why gA analogues that would be expected to be monomeric increase the water permeability in thin bilayers (111): a significant

amount of the water could go through such metastable channel-forming monomers. Water permeability of the dimer was estimated using the same protocol (Figure 4.14). Water movement can be interrupted (as indicated by the plateau regions) by EAM swing motion and K^+ binding at the channel entrances (Figures 4.4 (A) and 4.5), which blocks water movement in the single-filing pore.

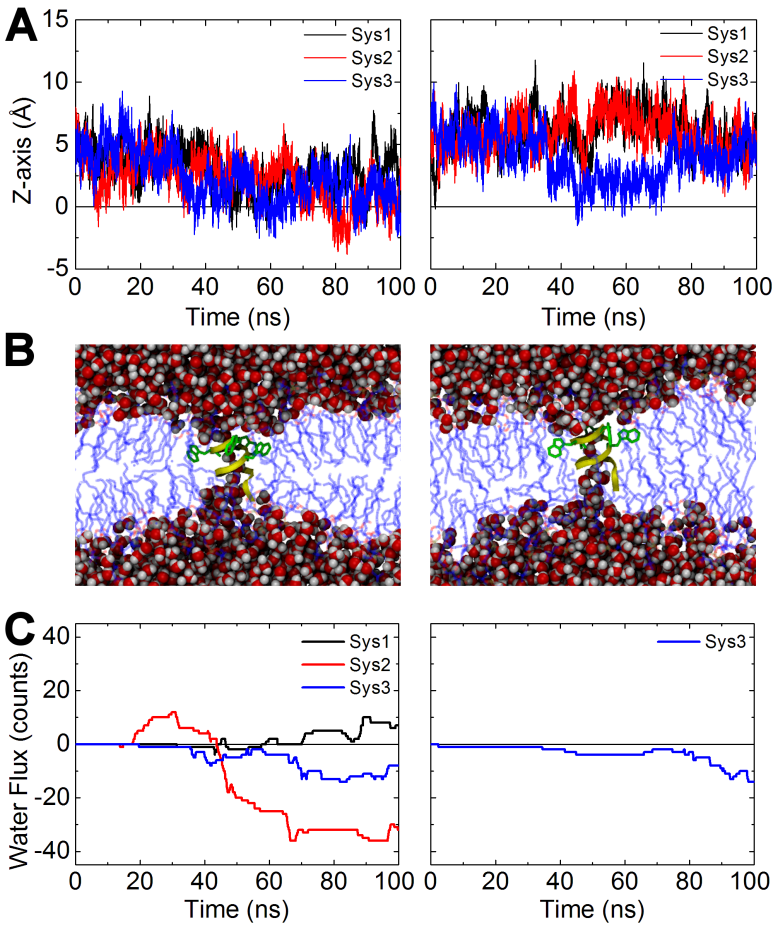

Figure 4.12. Monomeric subunit in DLPC (left column) and DMPC (right column) bilayers. (A) Time series of the *Z*-coordinate of the gA monomer's center of mass (COM) in the bilayers. (B) Snapshots of water pore formation in the bilayers. The gA monomeric subunit is colored *yellow* and Trp *green*, and the lipid molecules *blue*. Water molecules are represented as spheres. (C) The number of water molecules translocated through gA monomers as a function of time (see the main text for definition).

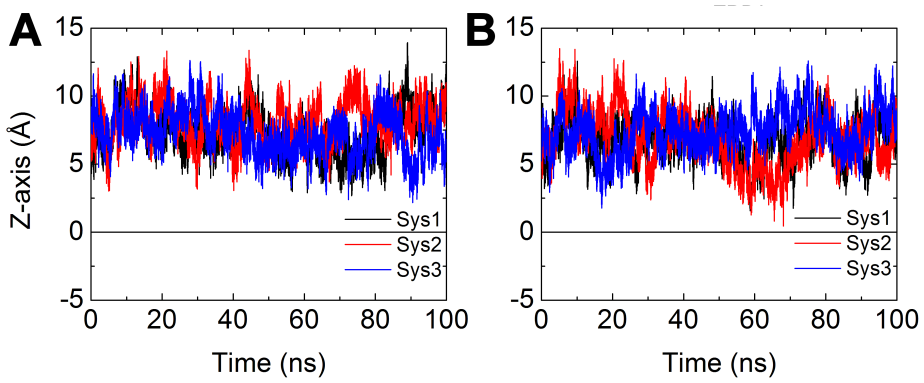

Figure 4.13. Time series of the Z-coordinate of the gA monomer's center of mass (COM) in (A) DOPC and (B) POPC bilayers.

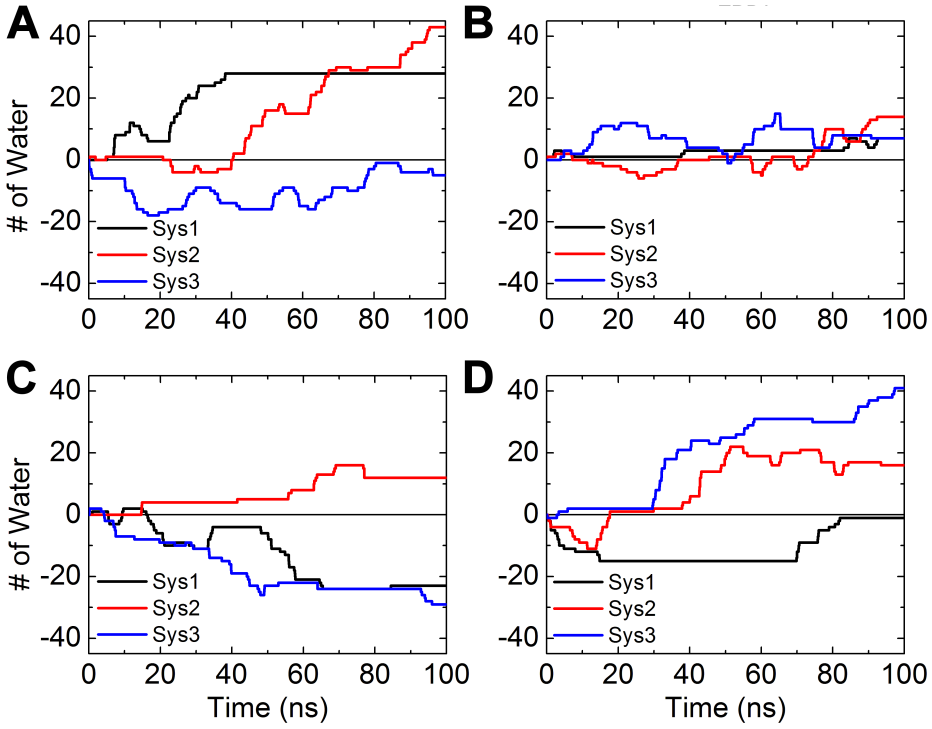

Figure 4.14. The number of water molecules translocated through gA dimers as a function of time in (A) DLPC, (B) DMPC, (C) DOPC, and (D) POPC bilayers.

4.3.2 Influence of hydrophobic mismatch on lipid structure and dynamics

To examine the hydrophobic mismatch-induced changes in lipid structure and dynamics, we first explored the lipid distribution around the gA dimers and monomers in the different bilayers. We calculated the two-dimensional (2D) radial distribution function, $g(r)$, based on the COM or the choline N atoms for each lipid type as a function of radial distance (r) from the gA center.

$$g(r) = \frac{\rho(r)}{\rho_{bulk}} = \frac{N(r, r+dr)}{2\pi r dr} \frac{1}{\rho_{bulk}} \tag{4.1}$$

where $2\pi r dr$ is the area in between r and $r + dr$, $N(r, r+dr)$ is the number of lipid molecules in the area, and ρ_{bulk} is the two-dimensional density of a pure lipid bilayer. Figures 4.15 and 4.16 show $g(r)$ for each lipid type, and Table 4.2 summarizes each shell size based on the COM $g(r)$ and the number of lipid molecules in each shell. There is little variation among the different lipid types. The first peak is at 11–12 Å, and there are 9–11 lipid molecules in the first shell. The $g(r)$ based on the choline N atoms shows that the choline moiety in the phospholipid head group may interfere with gA channel function (99) (Figure 4.17), because the cholines may "reach in" over the channel to approach the pore entrance. Though the cholines thereby could block water movement, its residence time usually is very short (mostly less than 10 ps), and there was no clear correlation between water flux and choline blocking in Figures 4.12 (C) and 4.14.

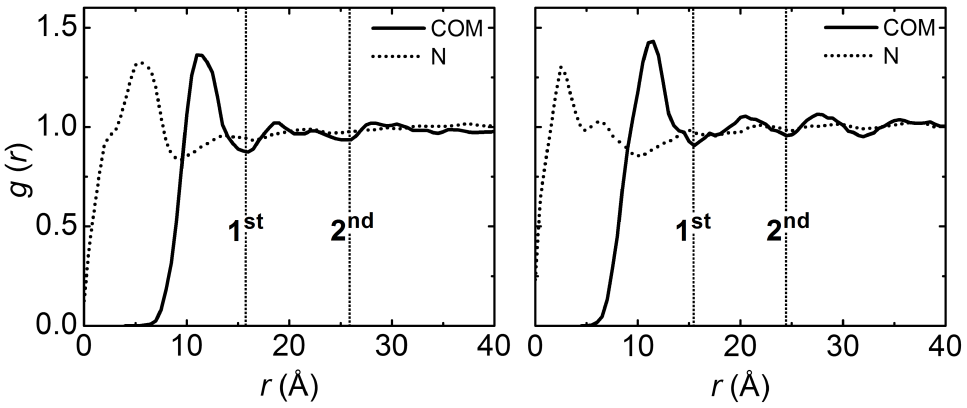

Figure 4.15. Radial distribution functions of lipid atoms (the choline N) and the lipid center of mass (COM) around gA dimers (left) and monomeric subunits (right) as a function of *r* in DOPC bilayers. The first and second shells are denoted as dotted lines.

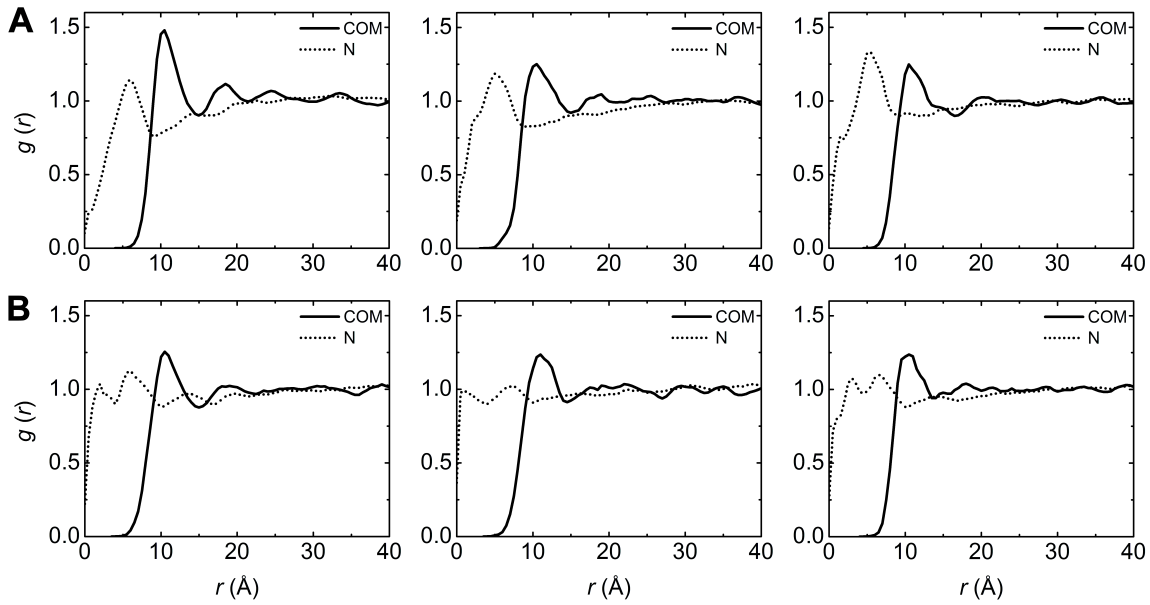

Figure 4.16. Radial distribution functions of lipid atoms (the choline N) and the lipid center of mass (COM) around gA dimers. (A) and monomeric subunits (B) as a function of *r* in (from left to right) DLPC, DMPC, and POPC bilayers.

Table 4.2. Lipid shell size (1st and 2nd) and the number of lipid molecule in each shell with standard error of 3 systems (for the dimer, upper and lower leaflets are considered and for the monomeric subunit only upper one is considered).

Lipid	Dimer (# of lipid)		Monomer (# of lipid)	
	1st shell	2nd shell	1st shell	2nd shell
DLPC	15.0 Å (9.2 ± 0.1)	21.5 Å (12.3 ± 0.2)	15.0 Å (8.5 ± 0.1)	22.5 Å (13.8 ± 0.1)
DMPC	15.0 Å (9.4 ± 0.2)	22.0 Å (13.7 ± 0.2)	14.5 Å (8.3 ± 0.4)	N/A
DOPC	16.0 Å (9.2 ± 0.2)	26.0 Å (19.1 ± 0.3)	15.5 Å (8.9 ± 0.1)	24.5 Å (16.1 ± 0.3)
POPC	17.0 Å (11.2 ± 0.3)	27.5 Å (22.9 ± 0.2)	14.5 Å (7.7 ± 0.1)	N/A

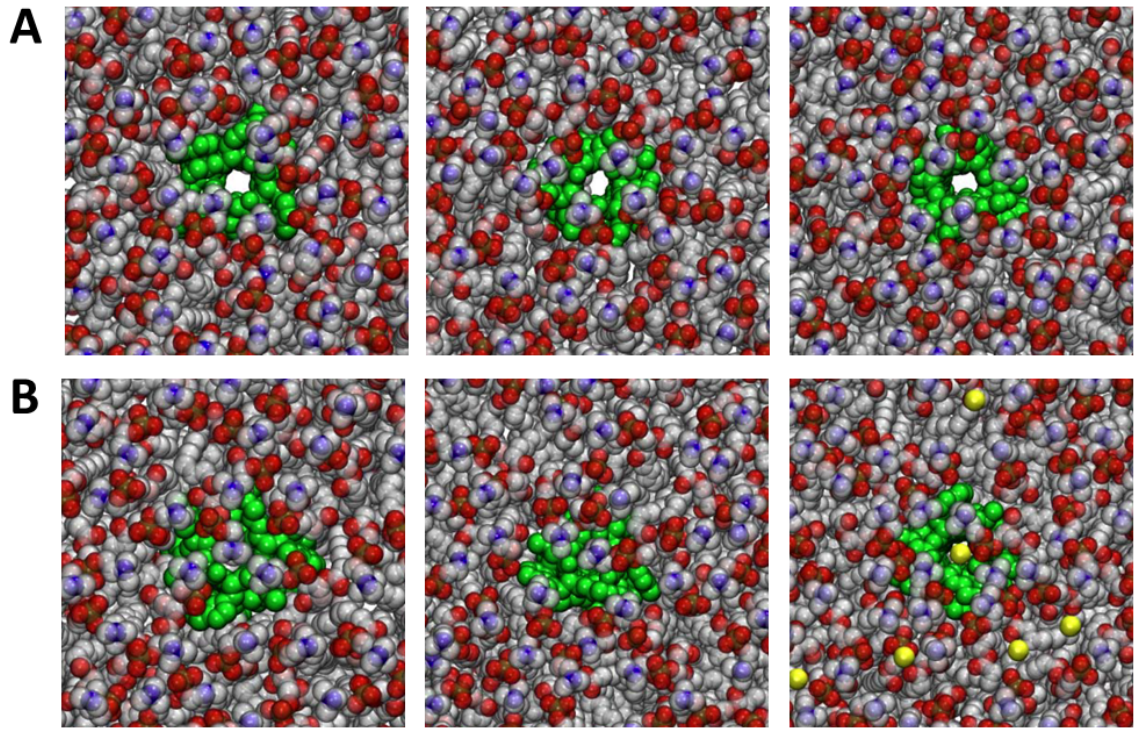

Figure 4.17. Snapshots of (A) clear open state of gA channels in DLCP, DMPC, and DOPC bilayers, respectively. (B).The gA channels occluded by lipid choline groups and K^+.in DMPC and POPC bilayers. The gA dimers are colored *green*, carbon atoms *gray*, oxygen atoms *red*, nitrogen atoms *blue*, and K^+ ions *yellow* spheres.

Knowing $g(r)$, we then could examine how lipid bilayer structure and dynamics responds to different hydrophobic mismatches by calculating the hydrophobic thickness, per-lipid surface area, compressibility, acyl chain order parameters, and lateral diffusion coefficients as functions of r. These are designated by the usual symbol followed by "(r)"; e.g., the bilayer hydrophobic thickness, d_H, is commonly defined as the average distance between the acyl chain C2 carbon atoms in both leaflets (16, 27), , and is written as $d_H(r)$. Similarly, the local area per lipid, area compressibility, and diffusion constant are denoted as $A(r)$, $K_A(r)$, and $D(r)$, respectively.

The thickness profiles (Figure 4.18 (A), 2D thickness profiles in Figure. 4.19) show both expected and surprising features. As would be expected from the gA channel structure, we observe no evidence for residual hydrophobic exposure (112), meaning that there is near-perfect hydrophobic adaptation between the channel and its surrounding phospholipids. The 2D thickness profiles, however, show a remarkable variation in thickness within the first shell, with some lipids being more extended than their neighbors. These "hot spots" are due to lipids that have their cholines interacting with the pore entrance and to lipids that "slide" over the Trp side chains so that their carbonyl and phosphate oxygens can form hydrogen bonds with the indole NH groups (Figure 4.20). This organization is reminiscent of that suggested by Meulendijks et al. (113), but the interactions are unlikely to be specific in the usual sense because the gA channel function does not depend on the gA channel or phospholipid chirality (114).

Moving away from the channel, $d_H(r)$ decreased within 4–5 Å from the dimer/bilayer boundary (Figure 4.18 (A)). This decrease reflects, in part, the hot spots in the 2D profiles (Figure 4.19), which will tend to increase the bilayer thickness adjacent to the channel. Not including the hot spots in the thickness calculations reduced the $d_H(r)$ changes from ~4 Å to ~2 Å (for DMPC, POPC and DOPC) and from ~6 Å to ~3 Å for DLPC. The non-monotonic $d_H(r)$ profiles are in general agreement with the profile deduced by Huang (86) using the continuum theory of elastic bilayer deformation, but more pronounced so. The $d_H(r)$ profiles in Figures 4.18 (A) and 4.19 differ from the profiles deduced by Helfrich and Jakobsson (88) and Nielsen et al. (90) by minimizing the deformation energy and by Lundbæk and Andersen (93) from fitting the continuum theory to the gA lifetime vs. bilayer thickness data of Elliott et al. (115).

Except for DLPC, the $d_H(r)$ profiles close to the dimers were similar. This need not imply, however, that there is less hydrophobic adaptation in DLPC bilayers because the dimer's θ is larger in this system (see Figure 4.6 (A)). In the case of DLPC (positive mismatch) and DMPC (near match) bilayers, the perturbation extended over the first and second shells, whereas the lipid adaptation in DOPC and POPC (negative mismatch) bilayers occurred mostly within the first shell. The average DLPC bilayer thickness in the first shell was about 2 Å thicker than the bulk thickness, in general agreement with the X-ray diffraction results (116). The average DMPC bilayer thickness in the first shell was ~3 Å greater than that in the DLPC system (Figure 4.18 (A)), which is in general agreement with Harroun et al.'s estimation of the local thickness in the DMPC system to be 2 Å greater than that in the DLPC system (116).

Compared to our previous study (27) showing that the PMF-minimum orientations of WALP helical peptides minimize a hydrophobic mismatch by changing θ with minimum perturbation of lipid bilayers, the gA channels in DLPC and DMPC bilayers showed strong lipid adaptation. In other words, simple single-pass TM helices such as WALPs and VpuTM respond to a large hydrophobic mismatch through changes in θ , whereas the gA channels overcome the energetic penalty due to a hydrophobic mismatch by imposing changes in $d_H(r)$ with minimal changes in θ (117). $d_H(r)$ approached the bulk values at r = 30–40 Å, within the third lipid shell surrounding the channel. In the case of free-floating monomeric subunits, in which lesser constraints are imposed on the bilayer, there was less lipid adaptation (except DLPC bilayers where monomeric subunits form water pores) (see Figure 4.20) than in the case of channel-forming dimers (Figure 4.18 (A)).

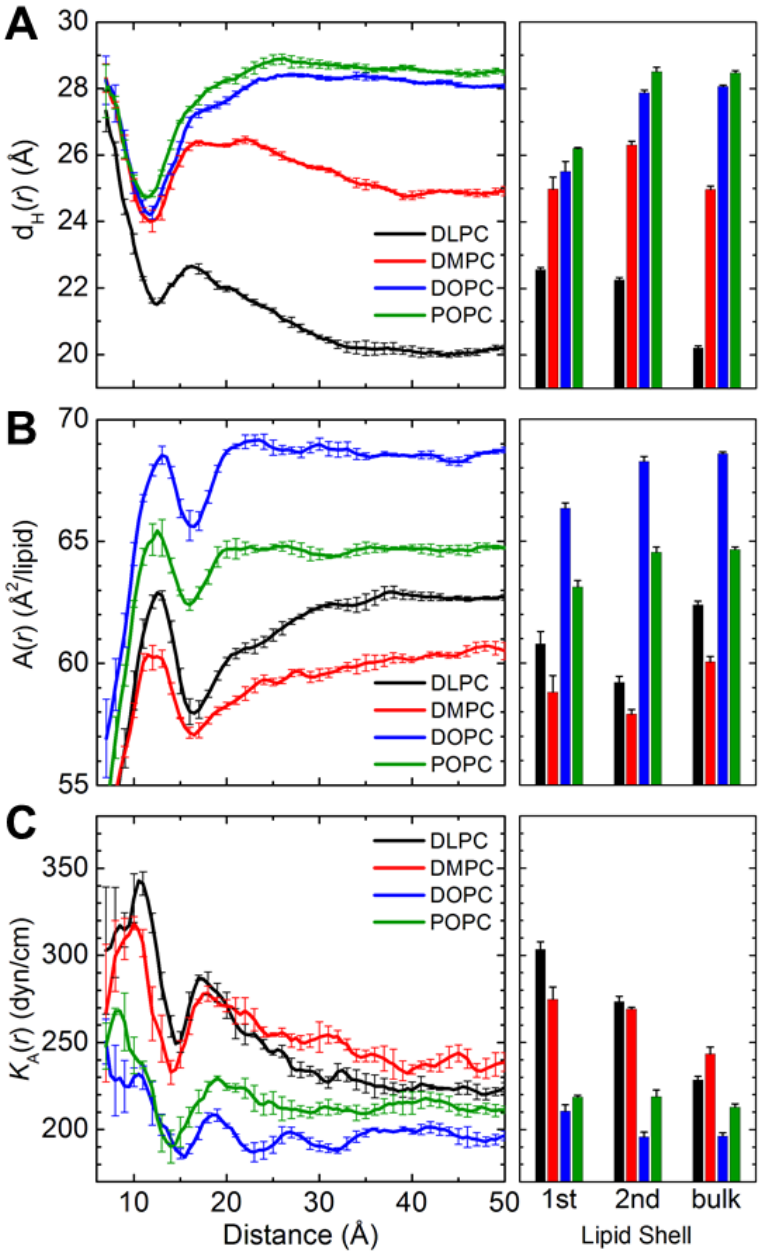

Figure 4.18. gA-induced lipid bilayer deformations in bilayers of different thickness (A) Hydrophobic thickness profile, (B) area per lipid profile, and (C) compressibility profile

as a function of r (mean ± standard error). The right-hand panels show the results for the first and second lipid shells and for the bulk (shell definitions are from Table 4.2).

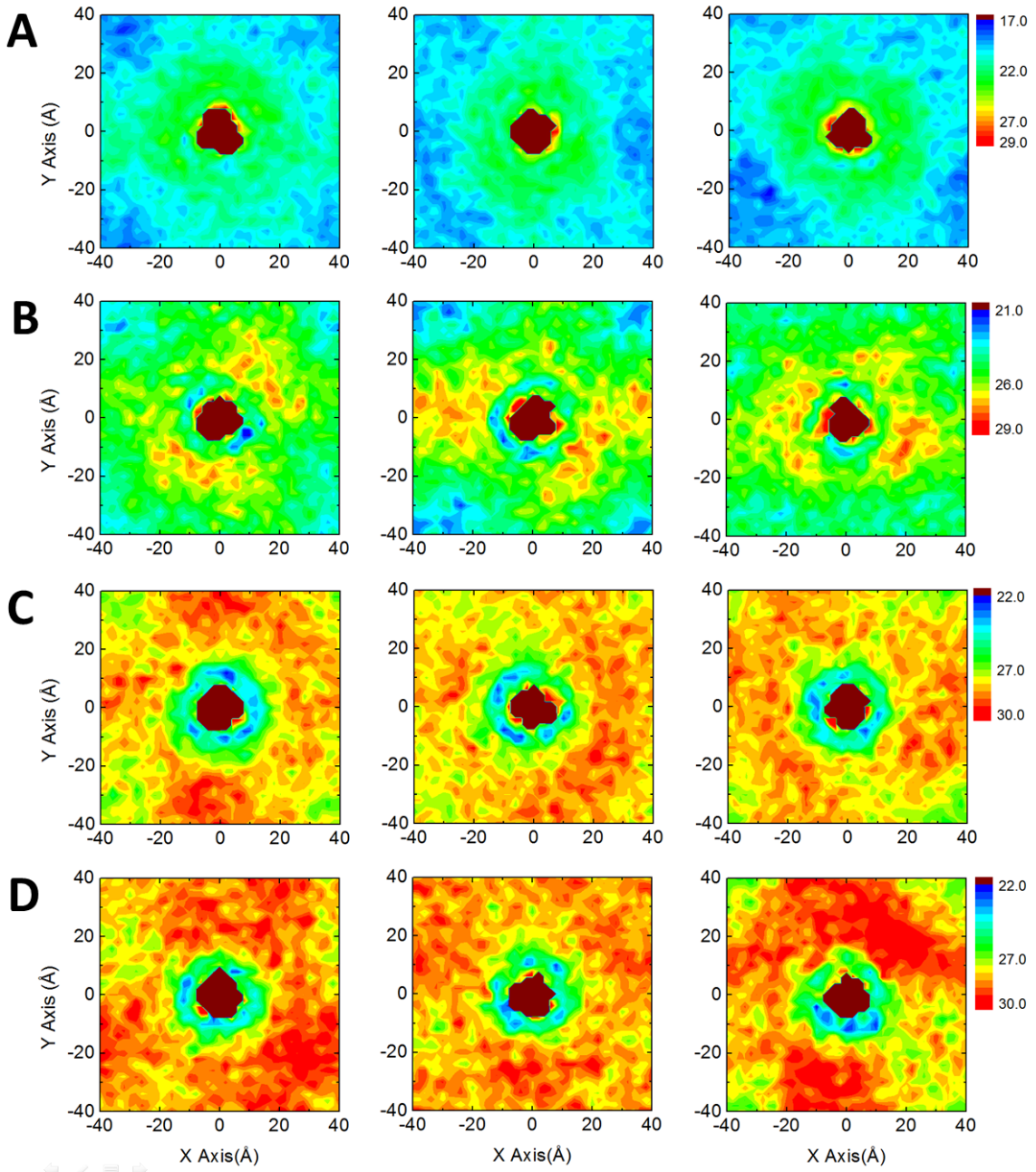

Figure 4.19. 2D hydrophobic thickness distributions of lipid bilayer of gA dimer systems in (A) DLPC, (B) DMPC, (C) DOPC, and (D) POPC bilayers (Unit: Å). Note the isolated "hotspots" where the lipid molecules are more extended.

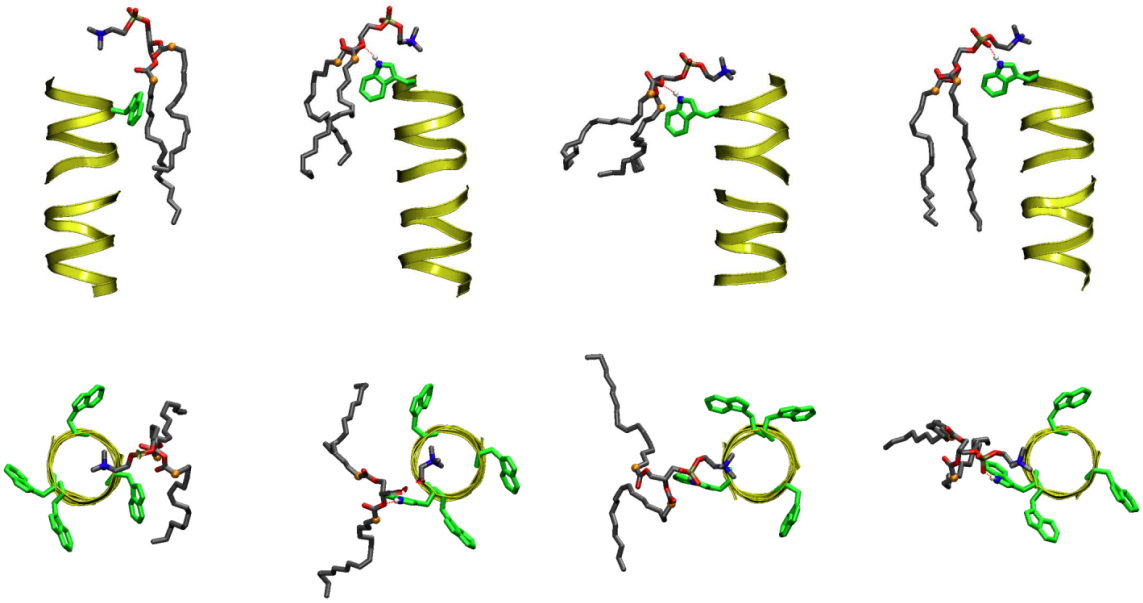

Figure 4.20. Snapshots of showing interactions between the gA backbone and Trps, and lipid molecule. The gA dimer is colored yellow and Trp green. The lipid molecule is represented as stick models (*blue*; nitrogen, *red*; oxygen, and C2 carbon as *orange* sphere).

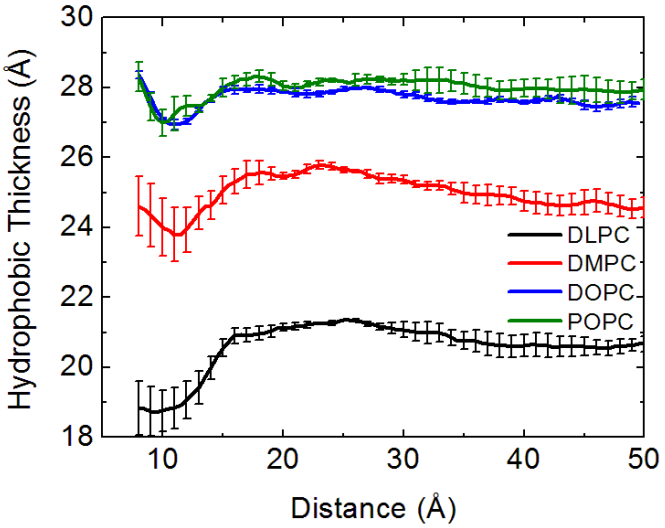

Figure 4.21. Hydrophobic thickness profile of each lipid bilayer type as a function of *r* in monomeric systems.

Phospholipids are almost incompressible (118), in which case the $d_H(r)$ profiles in Figure 4.18 (A) should be associated with reciprocal changes in lipid area. To explore this, we estimated the per-lipid surface area, $A(r)$, using the Voronoi tessellation approach by Pandit et al. (119). A lipid molecule was first defined by three key atoms located approximately at the hydrophobic/hydrophilic interface: the two carbonyl carbon atoms on each chain and the carbon that connects the two aliphatic chains to the chain leading to the phosphate. The gA structure was defined by the backbone heavy atoms. Delaunay triangulation was then used to determine the circumcenters of triangles that resulted in vertices for the Voronoi polygons to obtain lipid areas, and the Quickhull program (120) was used for this geometric calculation. In each bilayer type, $A(r)$ is indeed anti-correlated with $d_H(r)$ (Figure 4.18 (B)). $A(r)$ in the bulk region agree well with per-lipid surface areas estimated in previous MD simulations (100), and lipid bilayer experiments: 63.2 ± 0.5 Å^2 (DLPC), 60.6 ± 0.5 Å^2 (DMPC), 67.4 ± 1.0 Å^2 (DOPC), and 68.3 ± 0.5 Å^2 (POPC) (121, 122). Because $A(r)$ is (anti)-correlated with $d_H(r)$, the profile is not simply monotonic. Beyond the first shell, $d_H(r)$ increased gradually in the case of positive mismatch. In the case of negative mismatch, the lipid bilayer adjustment occurred within 20 Å, and one might expect $A(r)$ to be increased near the protein because of lipid compression (123). This area increment was not observed due to the local increase in $d_H(r)$.

The per-lipid surface areas together with their fluctuations allow for an estimate the local compressibility modulus, $K_A(r)$ (124).

$$K_A(r) = \frac{k_B T A(r)}{N\left\langle \delta A(r)^2 \right\rangle} \tag{4.2}$$

where $k_B T$ is the thermal energy and N the number of lipid molecules in a leaflet. Figure 4.18 (C) shows $K_A(r)$ for each system. The compressibility moduli for the bulk (r > ~30 Å) are similar to each other, 200–250 dyn/cm, and to those of pure lipid bilayers: 234 ± 23 dyn/cm (DMPC) and 237 ± 16 dyn/cm (DOPC) (125). $K_A(r)$ for lipids in the first shell are higher than the bulk values, indicating that the lipid acyl chains in the vicinity of the channel are harder to compress. From the calculated lipid bilayer parameters ($d_H(r)$, $A(r)$, and $K_A(r)$), we conclude that the first shell is highly perturbed because the system has to adjust to both gA-lipid interactions (hydrogen bond formation to the indole NH groups) and hydrophobic mismatch in order to maintain the constant bilayer density. In the second shell, the lipids are less stressed than in the first shell, and then the perturbation decays monotonically. $A(r)$ and $K_A(r)$ in the first shell are subject to uncertainty because of the arbitrariness in defining the gA structure in the Voronoi polyhedral calculations. The consistency of between these quantities and $d_H(r)$, which is not calculated from Voronoi polyhedra, indicates that the Voronoi definitions are reasonable.

The hydrophobic mismatch-imposed lipid adaptation around gA channels (Figure 4.18) affects acyl chain dynamics and orientation (123). The relative order of the hydrocarbon tails can be obtained from the order parameter, S_{CD},

$$S_{CD} = \frac{1}{2}\left\langle 3\cos^2 \theta_{CH} - 1 \right\rangle \tag{4.3}$$

where θ_{CH} is the angle between the CH bond vector and the bilayer normal (note, we use

θ in a different context in the discussion of the channel tilt); S_{CD} defined in this way can be directly compared with the order parameter measured by deuterium NMR, and is therefore denoted as the deuterium order parameter. Figure 4.22 compares S_{CD} in each shell and includes available experimental measurements (126, 127). As in previous studies (96), DLPC and DMPC bilayers (Figure 4.22 (A) and (B)) show higher S_{CD} in the first and second shell than in the bulk lipids due to chain ordering induced by local increase in $d_H(r)$ (Figure 4.18 (A)) together with the decrease in $A(r)$ (Figure 4.18 (B)). In contrast, the first shell of DOPC and POPC bilayers (Figure 4.22 (C) and (D)), which is more compressed than the bulk lipids due to negative mismatch, S_{CD} is less than in bulk.

To further explore how protein-lipid incarnations affect lipid dynamics, we investigated the influence of protein-lipid interaction on lipid diffusion. The lateral diffusion coefficient, $D(r)$, was calculated on a grid in the XY-plane around the gA dimmer from the lateral mean-squared displacement (MSD) (128, 129) of each lipid COM, $\Delta x(t) = x(t + \Delta t) - x(t)$:

$$D(r) = \frac{\left\langle \left[\Delta x(t) - \left\langle \Delta x(t) \right\rangle\right]^2 + \left[\Delta y(t) - \left\langle \Delta y(t) \right\rangle\right]^2 \right\rangle}{4\Delta t} \tag{4.4}$$

At each grid point (a grid spacing = 1.0 Å), $D(r)$ was calculated with $\Delta t = 10$ ns and the calculated bulk values in the gA systems reasonable represent diffusion constants of pure lipid bilayers within 15% errors. Figures 4.22 and 4.23 show the 1D and 2D $D(r)$ distributions of each lipid bilayer, respectively. Generally, the $D(r)$ in the first and second shell is lower than in the bulk, and it show a relatively week correlation with the profiles

for $d_H(r)$, A(r), and $K_A(r)$ (Figure 4.17). Figure 4.22 shows a much larger D(r) for the DLPC bilayer than the others. Because the DMPC, DOPC, and POPC bilayers have the same head group and the same relative D(r) (~13.0×10^{-8} cm^2/s) in the bulk, acyl chain saturation and hydrophobic thickness of the lipid do not seem to be the factor that affected the D(r). Although the diffusion coefficient of DLPC bilayer is different from the others, the relative changes in D(r) between the first shell and the plateau region (at ~40 Å) are 2.32 (DLPC), 2.31 (DMPC), 2.41 (DOPC), and 2.10 (POPC), which implies that lipid adaptation by hydrophobic mismatch associated with DLPC bilayer is unlikely to be determining factor in the diffusion coefficient.

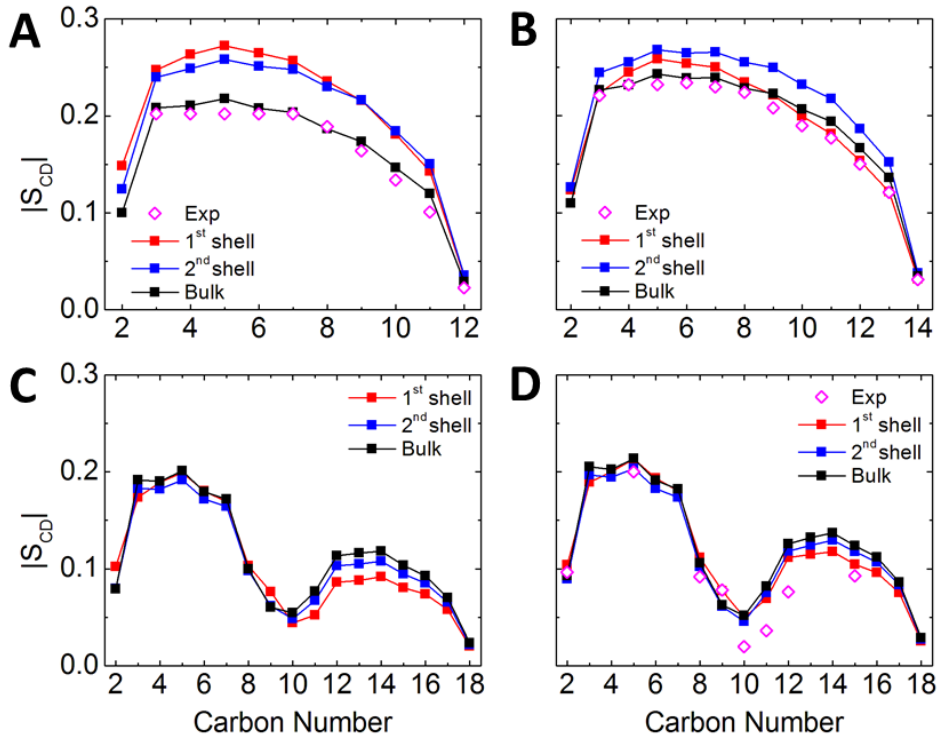

Figure 4.22. The ^{2}H order parameter of (A) DLPC, (B) DMPC, (C) DOPC, and (D) POPC (oleoly chain in the C2 glycerol backbone carbon) bilayers for the first and second lipid shells and bulk lipid (*red*; 1st shell, *blue*; 2nd shell, *black*; bulk, and *magenta diamond*; experimental results).

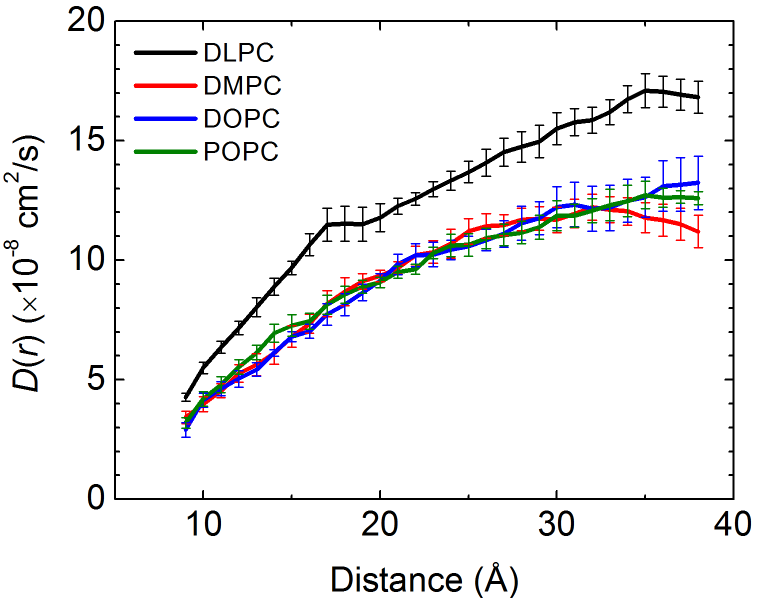

Figure 4.23. The lipid lateral diffusion coefficient as a function of *r* (mean ± standard error) for each lipid bilayer system.

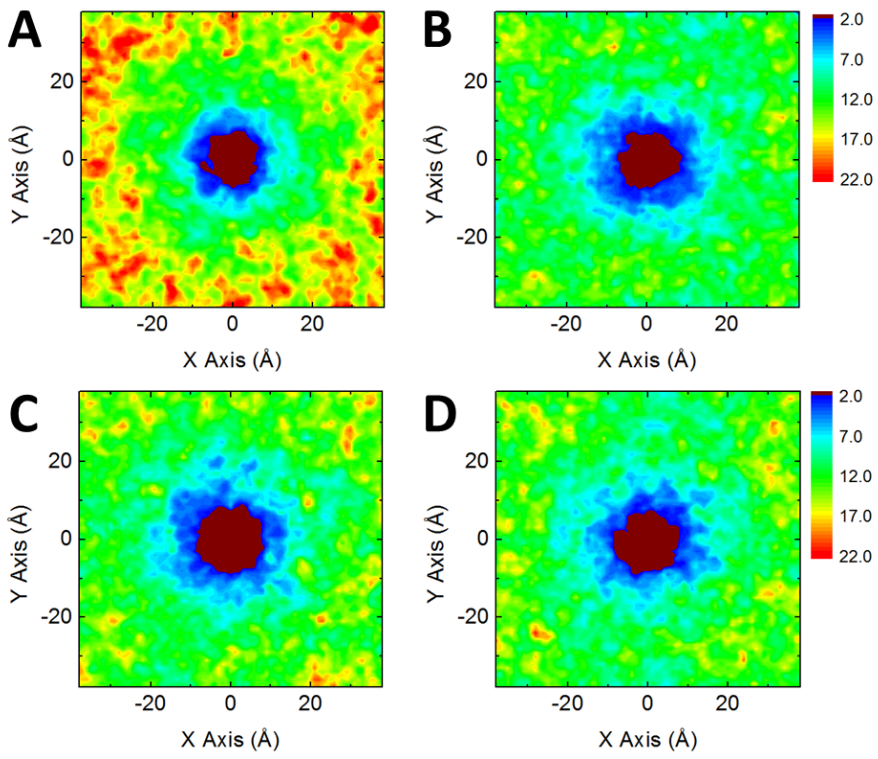

Figure 4.24. 2D distribution of the lipid lateral diffusion coefficient of (A) DLPC, (B) DMPC, (C) DOPC, and (D) POPC bilayers. (Unit: 10^{-8} cm^2/s)

4.4. Conclusions

Molecular dynamics simulations of gA dimers and monomers in all-atom DLPC, DMPC, DOPC, and POPC bilayers reveal a range of responses to different peptide/lipid hydrophobic mismatches. The structure of the gA dimer is largely unaffected by changes in lipid bilayer composition (thickness), and its tilt varies from 14° in DLPC the thinnest bilayer to 9° in DOPC. This 5° variation in tilt is less than the previously reported 16~17° difference deduced for single-pass TM α-helices in bilayers formed by the same lipids (107) or in similar mismatch conditions (27). That is, the lipid bilayer adapts to the gA, whereas single-pass TM α-helices such as WALPs and VpuTM adapt to the lipid bilayer. The monomeric gA subunits retain their β-helical conformation for the 100-ns simulation. They "float" in a single leaflet in DOPC and POPC bilayers, but can form metastable, water permeable bilayer-spanning channels in DLPC and DMPC bilayers.

The bilayer structure and dynamics in the first lipid shell around gA dimers reflect both the channel-bilayer mismatch and hydrogen bond formation between the phospholipid carbonyl and phosphate oxygens and the indole NH groups. The results provide support for the importance of hydrophobic adaptation between integral membrane proteins and their host bilayer, which was near-perfect in this case, and show also that hydrogen bond formation between the indole side chains and the phospholipid phosphate and carbonyls, or choline interacting with the pore entrance, may impact on the lipid structure and dynamics. The radial dependence of hydrophobic thickness, lipid

area, and bilayer compressibility vary non-monotonically over the first lipid shell around the channel and reach their bulk values in the second shell in DOPC and POPC bilayers and in the third shell in DLPC and DMPC bilayers. Order parameters and diffusion coefficients also differ for lipids in the first and second shells and the bulk. Reflecting the different order parameters, the local compressibility moduli in the vicinity of the channel are higher than the bulk values, supporting Partenskii and Jordan's conjecture that the channel alters the local lipid dynamics—and thus the local moduli—beyond what would be predicted from a simple mismatch model. The non-monotonic variation in bilayer thickness within the first shell differs from the profiles commonly deduced using continuum deformation models. Importantly, the increased local moduli indicate that the bilayer deformation energies will be larger than predicted using the simple continuum description (assuming constant moduli). This has implications for evaluating the energetic cost of hydrophobic mismatch-induced bilayer deformations, which is likely to be larger than predicted using the continuum description. Lundbæk and Andersen (93), for example, found that the experimental gA single-channel lifetime vs. bilayer thickness relation could be fit by the continuum description (with constant moduli) only when using a phenomenological spring coefficient that was three-fold larger than the value predicted using equilibrium theory and assuming no constraints on lipid structure and dynamics (apart from that imposed by the hydrophobic mismatch).

References

1. Jordan, J. D., E. M. Landau, and R. Iyengar. 2000. Signaling networks: the origins of cellular multitasking. *Cell* 103:193-200.
2. Hunter, T. 2000. Signaling--2000 and beyond. *Cell* 100:113-127.
3. Murata, K., K. Mitsuoka, T. Hirai, T. Walz, P. Agre, J. B. Heymann, A. Engel, and Y. Fujiyoshi. 2000. Structural determinants of water permeation through aquaporin-1. *Nature* 407:599-605.
4. Fu, D., A. Libson, L. J. Miercke, C. Weitzman, P. Nollert, J. Krucinski, and R. M. Stroud. 2000. Structure of a glycerol-conducting channel and the basis for its selectivity. *Science (New York, N.Y* 290:481-486.
5. Jiang, Y., A. Lee, J. Chen, M. Cadene, B. T. Chait, and R. MacKinnon. 2002. Crystal structure and mechanism of a calcium-gated potassium channel. *Nature* 417:515-522.
6. Yellen, G. 2002. The voltage-gated potassium channels and their relatives. *Nature* 419:35-42.
7. Khademi, S., J. O'Connell, 3rd, J. Remis, Y. Robles-Colmenares, L. J. Miercke, and R. M. Stroud. 2004. Mechanism of ammonia transport by Amt/MEP/Rh: structure of AmtB at 1.35 A. *Science (New York, N.Y* 305:1587-1594.
8. Elston, T., H. Wang, and G. Oster. 1998. Energy transduction in ATP synthase. *Nature* 391:510-513.

9. Dong, J., G. Yang, and H. S. McHaourab. 2005. Structural basis of energy transduction in the transport cycle of MsbA. *Science (New York, N.Y* 308:1023-1028.

10. Alberts, B. 2002. Molecular biology of the cell.xxxiv, 1463, [1486] p.

11. Wallin, E., and G. von Heijne. 1998. Genome-wide analysis of integral membrane proteins from eubacterial, archaean, and eukaryotic organisms. *Protein Sci* 7:1029-1038.

12. Andersen, O. S., and R. E. Koeppe II. 2007. Bilayer Thickness and Membrane Protein Function: An Energetic Perspective. *Annu. Rev. Biophys. Biomol. Struct.* 36:107−130.

13. Lee, J., and W. Im. 2007. Restraint potential and free energy decomposition formalism for helical tilting. *Chem. Phys. Lett.* 441:132−135.

14. Jensen, M. Ø., and O. G. Mouritsen. 2004. Lipids do influence protein function—the hydrophobic matching hypothesis revisited. *Biochimica et Biophysica Acta (BBA) - Biomembranes* 1666:205-226.

15. van der Wel, P. C. A., E. Strandberg, J. A. Killian, and R. E. Koeppe II. 2002. Geometry and Intrinsic Tilt of a Tryptophan-Anchored Transmembrane α-Helix Determined by ^{2}H NMR. *Biophys. J.* 83:1479−1488.

16. de Planque, M. R. R., and J. A. Killian. 2003. Protein-lipid interactions studied with designed transmembrane peptides: role of hydrophobic matching and interfacial anchoring (Review). *Mol. Membr. Biol.* 20:271−284.

17. Strandberg, E., S. direkcan, D. T. S. Rijkers, P. C. A. van der Wel, R. E. Koeppe II, R. M. J. Liskamp, and J. Antoinette Killian. 2004. Tilt Angles of Transmembrane Model Peptides in Oriented and Non-Oriented Lipid Bilayers as Determined by ^{2}H Solid-State NMR. *Biophys. J.* 86:3709−3721.

18. Park, S. H., and S. J. Opella. 2005. Tilt Angle of a Trans-membrane Helix is Determined by Hydrophobic Mismatch. *J. Mol. Biol.* 350:310−318.

19. Ozdirekcan, S., D. T. S. Rijkers, R. M. J. Liskamp, and J. A. Killian. 2005. Influence of Flanking Residues on Tilt and Rotation Angles of Transmembrane Peptides in Lipid Bilayers. A Solid-State ^{2}H NMR Study. *Biochemistry* 44:1004−1012.

20. Killian, J. A., and T. K. Nyholm. 2006. Peptides in lipid bilayers: the power of simple models. *Curr. Opin. Struct. Biol.* 16:473−479.

21. Petrache, H. I., D. M. Zuckerman, J. N. Sachs, J. A. Killian, R. E. Koeppe II, and T. B. Woolf. 2002. Hydrophobic Matching Mechanism Investigated by Molecular Dynamics Simulations. *Langmuir* 18:1340−1351.

22. Im, W., and C. L. Brooks III. 2005. Interfacial folding and membrane insertion of designed peptides studied by molecular dynamics simulations. *Proc. Natl. Acad. Sci. U.S.A.* 102:6771−6776.

23. Kandasamy, S. K., and R. G. Larson. 2006. Molecular Dynamics Simulations of Model Trans-Membrane Peptides in Lipid Bilayers: A Systematic Investigation of Hydrophobic Mismatch. *Biophys. J.* 90:2326−2343.

24. Ozdirekcan, S., C. Etchebest, J. A. Killian, and P. F. J. Fuchs. 2007. On the Orientation of a Designed Transmembrane Peptide: Toward the Right Tilt Angle? *J. Am. Chem. Soc.* 129:15174−15181.

25. Esteban-Mart, S., and J. Salgado. 2007. The Dynamic Orientation of Membrane-Bound Peptides: Bridging Simulations and Experiments. *Biophys. J.* 93:4278−4288.

26. Lee, J., and W. Im. 2008. Transmembrane Helix Tilting: Insights from Calculating the Potential of Mean Force. *Phys. Rev. Lett.* 100:018103.

27. Kim, T., and W. Im. 2010. Revisiting Hydrophobic Mismatch with Free Energy Simulation Studies of Transmembrane Helix Tilt and Rotation. *Biophys. J.* 99:175−183.

28. Monticelli, L., D. P. Tieleman, and P. F. J. Fuchs. 2010. Interpretation of ^{2}H-NMR Experiments on the Orientation of the Transmembrane Helix WALP23 by Computer Simulations. *Biophys. J.* 99:1455−1464.

29. Arkin, I. T., A. T. Brünger, and D. M. Engelman. 1997. Are there dominant membrane protein families with a given number of helices? *Proteins: Struct., Funct., Genet.* 28:465−466.

30. Lichanska, A. M., and M. J. Waters. 2008. New Insights into Growth Hormone Receptor Function and Clinical Implications. *Hormone Research in Paediatrics* 69:138-145.

31. Killian, J. A. 1998. Hydrophobic mismatch between proteins and lipids in membranes *Biochim. Biophys. Acta Gene Struct. Expression* 1376:401−416.

32. Johannsson, A., G. A. Smith, and J. C. Metcalfe. 1981. The effect of bilayer thickness on the activity of (Na^+ + K^+)-ATPase. *Biochimica et Biophysica Acta (BBA) - Biomembranes* 641:416−421.

33. Froud, R. J., C. R. A. Earl, J. M. East, and A. G. Lee. 1986. Effects of lipid fatty acyl chain structure on the activity of the (Ca^{2+} + Mg^{2+})-ATPase. *Biochimica et Biophysica Acta (BBA) - Biomembranes* 860:354−360.

34. Pelham, H. R. B., and S. Munro. 1993. Sorting of membrane proteins in the secretory pathway. *Cell* 75:603−605.

35. Holt, A., R. B. M. Koehorst, T. Rutters-Meijneke, M. H. Gelb, D. T. S. Rijkers, M. A. Hemminga, and J. A. Killian. 2009. Tilt and Rotation Angles of a Transmembrane Model Peptide as Studied by Fluorescence Spectroscopy. *Biophys. J.* 97:2258−2266.

36. Torrie, G. M., and J. P. Valleau. 1977. Nonphysical sampling distributions in Monte Carlo free-energy estimation: Umbrella sampling. *J. Comput. Phys.* 23:187−199.

37. Lee, J., and W. Im. 2007. Implementation and application of helix-helix distance and crossing angle restraint potentials. *J. Comput. Chem.* 28:669−680.

38. Im, W., J. Lee, T. Kim, and H. Rui. 2009. Novel free energy calculations to explore mechanisms and energetics of membrane protein structure and function. *J. Comput. Chem.* 30:1622−1633.

39. Jo, S., T. Kim, and W. Im. 2007. Automated Builder and Database of Protein/Membrane Complexes for Molecular Dynamics Simulations. *PLos ONE* 2:e880.

40. Jo, S., J. B. Lim, J. B. Klauda, and W. Im. 2009. CHARMM-GUI Membrane Builder for Mixed Bilayers and Its Application to Yeast Membranes. *Biophys. J.* 97:50−58.

41. Jo, S., T. Kim, V. G. Iyer, and W. Im. 2008. CHARMM-GUI: A web-based graphical user interface for CHARMM. *J. Comput. Chem.* 29:1859−1865.

42. Brooks, B. R., C. L. Brooks III, A. D. Mackerell Jr., L. Nilsson, R. J. Petrella, B. Roux, et al. 2009. CHARMM: The biomolecular simulation program. *J. Comput. Chem.* 30:1545−1614.

43. MacKerell Jr, A. D., D. Bashford, M. Bellott, R. L. Dunbrack Jr, J. D. Evanseck, M. J. Field, et al. 1998. All-atom empirical potential for molecular modeling and dynamics studies of proteins. *J. Phys. Chem. B* 102:3586−3616.

44. Mackerell Jr, A. D., M. Feig, and C. L. Brooks III. 2004. Extending the treatment of backbone energetics in protein force fields: Limitations of gas-phase quantum mechanics in reproducing protein conformational distributions in molecular dynamics simulations. *J. Comput. Chem.* 25:1400−1415.

45. Jorgensen, W. L., J. Chandrasekhar, J. D. Madura, R. W. Impey, and M. L. Klein. 1983. Comparison of simple potential functions for simulating liquid water. *J. Chem. Phys.* 79:926−935.

46. Klauda, J. B., B. R. Brooks, A. D. MacKerell Jr, R. M. Venable, and R. W. Pastor. 2005. An ab Initio Study on the Torsional Surface of Alkanes and Its Effect on Molecular Simulations of Alkanes and a DPPC Bilayer. *J. Phys. Chem. B* 109:5300−5311.

47. Nagle, J. F., and S. Tristram-Nagle. 2000. Structure of lipid bilayers. *Biochim. Biophys. Acta Gene Struct. Expression* 1469:159−195.

48. Ryckaert, J.-P., G. Ciccotti, and H. J. C. Berendsen. 1977. Numerical integration of the cartesian equations of motion of a system with constraints: molecular dynamics of n-alkanes. *J. Comput. Phys.* 23:327−341.

49. Hoover, W. G. 1985. Canonical dynamics: Equilibrium phase-space distributions. *Phys. Rev. A: At. Mol. Opt. Phys.* 31:1695−1697.

50. Feller, S. E., Y. Zhang, and R. W. Pastor. 1995. Computer simulation of liquid/liquid interfaces. II. Surface tension-area dependence of a bilayer and monolayer. *J. Chem. Phys.* 103:10267−10276.

51. Andersen, O. S., and R. E. Koeppe. 2007. Bilayer Thickness and Membrane Protein Function: An Energetic Perspective. *Annu. Rev. Biophys. Biomol. Struct.* 36:107−130.

52. Weiss, T. M., P. C. A. van der Wel, J. A. Killian, R. E. Koeppe II, and H. W. Huang. 2003. Hydrophobic Mismatch between Helices and Lipid Bilayers. *Biophys. J.* 84:379−385.

53. Nezil, F. A., and M. Bloom. 1992. Combined influence of cholesterol and synthetic amphiphillic peptides upon bilayer thickness in model membranes. *Biophys. J.* 61:1176−1183.

54. Rog, T., K. Murzyn, R. Gurbiel, Y. Takaoka, A. Kusumi, and M. Pasenkiewicz-Gierula. 2004. Effects of phospholipid unsaturation on the bilayer nonpolar region: a molecular simulation study. *J. Lipid Res.* 45:326−336.

55. de Planque, M. R. R., J.-W. P. Boots, D. T. S. Rijkers, R. M. J. Liskamp, D. V. Greathouse, and J. A. Killian. 2002. The Effects of Hydrophobic Mismatch between Phosphatidylcholine Bilayers and Transmembrane α-Helical Peptides Depend on the Nature of Interfacially Exposed Aromatic and Charged Residues. *Biochemistry* 41:8396−8404.

56. Wimley, W. C., and S. H. White. 1996. Experimentally determined hydrophobicity scale for proteins at membrane interfaces. *Nat. Struct. Mol. Biol.* 3:842−848.

57. Strandberg, E., and J. A. Killian. 2003. Snorkeling of lysine side chains in transmembrane helices: how easy can it get? *FEBS Lett.* 544:69−73.

58. Killian, J. A., I. Salemink, M. R. R. de Planque, G. Lindblom, R. E. Koeppe II, and D. V. Greathouse. 1996. Induction of Nonbilayer Structures in Diacylphosphatidylcholine Model Membranes by Transmembrane α-Helical Peptides: Importance of Hydrophobic Mismatch and Proposed Role of Tryptophans. *Biochemistry* 35:1037−1045.

59. de Planque, M. R. R., J. A. W. Kruijtzer, R. M. J. Liskamp, D. Marsh, D. V. Greathouse, R. E. Koeppe II, B. de Kruijff, and J. A. Killian. 1999. Different Membrane Anchoring Positions of Tryptophan and Lysine in Synthetic Transmembrane α-Helical Peptides. *J. Biol. Chem.* 274:20839−20846.

60. Cross, T. A., and J. R. Quine. 2000. Protein structure in anisotropic environments: Development of orientational constraints. *Conc. Magn. Reson.* 12:55−70.

61. Opella, S. J., A. C. Zeri, and S. H. Park. 2008. Structure, Dynamics, and Assembly of Filamentous Bacteriophages by Nuclear Magnetic Resonance Spectroscopy. *Annu. Rev. Phys. Chem.* 59:635−657.

62. Vostrikov, V. V., C. V. Grant, A. E. Daily, S. J. Opella, and R. E. Koeppe II. 2008. Comparison of "Polarization Inversion with Spin Exchange at Magic Angle" and "Geometric Analysis of Labeled Alanines" Methods for Transmembrane Helix Alignment. *J. Am. Chem. Soc.* 130:12584−12585.

63. Strandberg, E., S. Esteban-Mart, J. Salgado, and A. S. Ulrich. 2009. Orientation and Dynamics of Peptides in Membranes Calculated from ^{2}H-NMR Data. *Biophys. J.* 96:3223−3232.

64. Holt, A., L. Rougier, V. Réat, F. Jolibois, O. Saurel, J. Czaplicki, J. A. Killian, and A. Milon. 2010. Order Parameters of a Transmembrane Helix in a Fluid Bilayer: Case Study of a WALP Peptide. *Biophys. J.* 98:1864−1872.

65. Esteban-Martín, S., D. Giménez, G. Fuertes, and J. s. Salgado. 2009. Orientational Landscapes of Peptides in Membranes: Prediction of ^{2}H NMR Couplings in a Dynamic Context. *Biochemistry* 48:11441−11448.

66. Bonvin, A. M. J. J., and A. T. Brünger. 1995. Conformational Variability of Solution Nucelar Magnetic Resonance Structures. *J. Mol. Biol.* 250:80−93.

67. Lindorff-Larsen, K., R. B. Best, M. A. DePristo, C. M. Dobson, and M. Vendruscolo. 2005. Simultaneous determination of protein structure and dynamics. *Nature* 433:128−132.

68. Richter, B., J. Gsponer, P. Várnai, X. Salvatella, and M. Vendruscolo. 2007. The MUMO (minimal under-restraining minimal over-restraining) method for the determination of native state ensembles of proteins. *J. Biomol. NMR* 37:117−135.

69. Lazaridis, T., and M. Karplus. 1999. Effective energy function for proteins in solution. *Proteins: Struct., Funct., Genet.* 35:133−152.

70. Lazaridis, T. 2003. Effective energy function for proteins in lipid membranes. *Proteins: Struct., Funct., Genet.* 52:176−192.

71. Kumar, S., J. M. Rosenberg, D. Bouzida, R. H. Swendsen, and P. A. Kollman. 1992. THE weighted histogram analysis method for free-energy calculations on biomolecules. I. The method. *J. Comput. Chem.* 13:1011−1021.

72. Jo, S., and W. Im. 2011. Transmembrane Helix Orientation and Dynamics: Insights from Ensemble Dynamics with Solid-State NMR Observables. *submitted*.

73. Lee, J., J. Chen, C. L. Brooks III, and W. Im. 2008. Application of solid-state NMR restraint potentials in membrane protein modeling. *J. Magn. Reson.* 193:68−76.

74. Davis, J. H. 1983. The description of membrane lipid conformation, order and dynamics by ^{2}H-NMR. *Biochim. Biophys. Acta* 737:117−171.

75. Im, W., S. Jo, and T. Kim. 2011. An ensemble dynamics approach to decipher solid-state NMR observables of membrane proteins. *Biochimica et Biophysica Acta (BBA) - Biomembranes*:In Press.

76. Chen, J., W. Im, and C. L. Brooks III. 2005. Application of torsion angle molecular dynamics for efficient sampling of protein conformations. *J. Comput. Chem.* 26:1565−1578.

77. Berendsen, H. J. C., J. P. M. Postma, W. F. v. Gunsteren, A. DiNola, and J. R. Haak. 1984. Molecular dynamics with coupling to an external bath. *J. Chem. Phys.* 81:3684−3690.

78. Best, R. B., and M. Vendruscolo. 2004. Determination of Protein Structures Consistent with NMR Order Parameters. *J. Am. Chem. Soc.* 126:8090−8091.

79. Lee, J., S. Ham, and W. Im. 2009. Beta-hairpin restraint potentials for calculations of potentials of mean force as a function of beta-hairpin tilt, rotation, and distance. *J. Comput. Chem.* 30:1334−1343.

80. Rui, H., and W. Im. 2010. Protegrin-1 orientation and physicochemical properties in membrane bilayers studied by potential of mean force calculations. *J. Comput. Chem.* 31:2859−2867.

81. Im, W., M. Feig, and C. L. Brooks III. 2003. An Implicit Membrane Generalized Born Theory for the Study of Structure, Stability, and Interactions of Membrane Proteins. *Biophys. J.* 85:2900−2918.

82. Vostrikov, V. V., A. E. Daily, D. V. Greathouse, and R. E. Koeppe II. 2010. Charged or Aromatic Anchor Residue Dependence of Transmembrane Peptide Tilt. *J. Biol. Chem.* 285:31723−31730.

83. Popot, J.-L., and D. M. Engelman. 2000. HELICAL MEMBRANE PROTEIN FOLDING, STABILITY, AND EVOLUTION. *Annu. Rev. Biochem* 69:881−922.

84. Southall, N. T., and K. A. Dill. 2000. The Mechanism of Hydrophobic Solvation Depends on Solute Radius. *J. Phys. Chem. B* 104:1326−1331.

85. Mouritsen, O. G., and M. Bloom. 1984. Mattress model of lipid-protein interactions in membranes. *Biophys. J.* 46:141−153.

86. Huang, H. W. 1986. Deformation free energy of bilayer membrane and its effect on gramicidin channel lifetime. *Biophys. J.* 50:1061−1070.

87. Lundbæk, J. A., S. A. Collingwood, H. I. Ingólfsson, R. Kapoor, and O. S. Andersen. 2010. Lipid bilayer regulation of membrane protein function: gramicidin channels as molecular force probes. *J. R. Soc. Interface* 7:373−395.

88. Helfrich, P., and E. Jakobsson. 1990. Calculation of deformation energies and conformations in lipid membranes containing gramicidin channels. *Biophys. J.* 57:1075−1084.

89. Aranda-Espinoza, H., A. Berman, N. Dan, P. Pincus, and S. Safran. 1996. Interaction between inclusions embedded in membranes. *Biophys. J.* 71:648−656.

90. Nielsen, C., M. Goulian, and O. S. Andersen. 1998. Energetics of Inclusion-Induced Bilayer Deformations. *Biophys. J.* 74:1966−1983.

91. Nielsen, C., and O. S. Andersen. 2000. Inclusion-Induced Bilayer Deformations: Effects of Monolayer Equilibrium Curvature. *Biophys. J.* 79:2583−2604.

92. Partenskii, M. B., and P. C. Jordan. 2002. Membrane deformation and the elastic energy of insertion: Perturbation of membrane elastic constants due to peptide insertion. *J. Chem. Phys.* 117:10768−10776.

93. Lundbæk, J. A., and O. S. Andersen. 1999. Spring Constants for Channel-Induced Lipid Bilayer Deformations Estimates Using Gramicidin Channels. *Biophys. J.* 76:889−895.

94. Goulian, M., O. N. Mesquita, D. K. Fygenson, C. Nielsen, O. S. Andersen, and A. Libchaber. 1998. Gramicidin Channel Kinetics under Tension. *Biophys. J.* 74:328−337.

95. Ingólfsson, H. I., and O. S. Andersen. 2010. Screening for Small Molecules' Bilayer-Modifying Potential Using a Gramicidin-Based Fluorescence Assay. *Assay Drug Dev. Technol.* 8:427−436.

96. Chiu, S.-W., S. Subramaniam, and E. Jakobsson. 1999. Simulation Study of a Gramicidin/Lipid Bilayer System in Excess Water and Lipid. I. Structure of the Molecular Complex. *Biophys. J.* 76:1929−1938.

97. Allen, T. W., O. S. Andersen, and B. Roux. 2003. Structure of Gramicidin A in a Lipid Bilayer Environment Determined Using Molecular Dynamics Simulations and Solid-State NMR Data. *J. Am. Chem. Soc.* 125:9868−9877.

98. Allen, T. W., T. Ba_tu, S. Kuyucak, and S.-H. Chung. 2003. Gramicidin A Channel as a Test Ground for Molecular Dynamics Force Fields. *Biophys. J.* 84:2159−2168.

99. Allen, T. W., O. S. Andersen, and B. Roux. 2006. Ion Permeation through a Narrow Channel: Using Gramicidin to Ascertain All-Atom Molecular Dynamics Potential of Mean Force Methodology and Biomolecular Force Fields. *Biophys. J.* 90:3447−3468.

100. Klauda, J. B., R. M. Venable, J. A. Freites, J. W. O'Connor, D. J. Tobias, C. Mondragon-Ramirez, I. Vorobyov, A. D. MacKerell Jr, and R. W. Pastor. 2010. Update of the CHARMM All-Atom Additive Force Field for Lipids: Validation on Six Lipid Types. *J. Phys. Chem. B* 114:7830−7843.

101. Townsley, L. E., W. A. Tucker, S. Sham, and J. F. Hinton. 2001. Structures of Gramicidins A, B, and C Incorporated into Sodium Dodecyl Sulfate Micelles†,‡. *Biochemistry* 40:11676−11686.

102. Ingólfsson, H. I., Y. Li, V. V. Vostrikov, H. Gu, J. F. Hinton, R. E. Koeppe II, B. t. Roux, and O. S. Andersen. 2011. Gramicidin A Backbone and Side Chain Dynamics Evaluated by Molecular Dynamics Simulations and Nuclear Magnetic Resonance Experiments. I: Molecular Dynamics Simulations. *J. Phys. Chem. B* 115:7417−7426.

103. Steinbach, P. J., and B. R. Brooks. 1994. New spherical-cutoff methods for long-range forces in macromolecular simulation. *J. Comput. Chem.* 15:667−683.

104. Essmann, U., L. Perera, M. L. Berkowitz, T. Darden, H. Lee, and L. G. Pedersen. 1995. A smooth particle mesh Ewald potential. *J. Chem. Phys.* 103:8577−8592.

105. Katsaras, J., R. S. Prosser, R. H. Stinson, and J. H. Davis. 1992. Constant helical pitch of the gramicidin channel in phospholipid bilayers. *Biophys. J.* 61:827−830.

106. Kim, T., S. Jo, and W. Im. 2011. Solid-State NMR Ensemble Dynamics as a Mediator between Experiment and Simulation. *Biophys. J.* 100:2922−2928.

107. Jo, S., and W. Im. 2011. Transmembrane Helix Orientation and Dynamics: Insights from Ensemble Dynamics with Solid-State NMR Observables. *Biophys. J.* 100:2913−2921.

108. Prosser, R. S., J. H. Davis, F. W. Dahlquist, and M. A. Lindorfer. 1991. Deuterium nuclear magnetic resonance of the gramicidin A backbone in a phospholipid bilayer. *Biochemistry* 30:4687−4696.

109. Killian, J. A., M. J. Taylor, and R. E. Koeppe II. 1992. Orientation of the valine-1 side chain of the gramicidin transmembrane channel and implications for channel functioning. A deuterium NMR study. *Biochemistry* 31:11283−11290.

110. Pulay, P., E. M. Scherer, P. C. A. van der Wel, and R. E. Koeppe II. 2005. Importance of Tensor Asymmetry for the Analysis of ^{2}H NMR Spectra from Deuterated Aromatic Rings. *J. Am. Chem. Soc.* 127:17488−17493.

111. Saparov, S. M., Y. N. Antonenko, R. E. Koeppe II, and P. Pohl. 2000. Desformylgramicidin: A Model Channel with an Extremely High Water Permeability. *Biophys. J.* 79:2526−2534.

112. Mondal, S., G. Khelashvili, J. Shan, Olaf S. Andersen, and H. Weinstein. 2011. Quantitative Modeling of Membrane Deformations by Multihelical Membrane Proteins: Application to G-Protein Coupled Receptors. *Biophys. J.* 101:2092−2101.

113. Meulendijks, G. H. W. M., T. Sonderkamp, J. E. Dubois, R. J. Nielen, J. A. Kremers, and H. M. Buck. 1989. The different influences of ether and ester phospholipids on the conformation of gramicidin A. A molecular modelling study. *Biochimica et Biophysica Acta (BBA) - Biomembranes* 979:321−330.

114. Providence, L. L., O. S. Andersen, D. V. Greathouse, R. E. Koeppe, and R. Bittman. 1995. Gramicidin Channel Function Does Not Depend on Phospholipid Chirality. *Biochemistry* 34:16404−16411.

115. Elliott, J. R., D. Needham, J. P. Dilger, and D. A. Haydon. 1983. The effects of bilayer thickness and tension on gramicidin single-channel lifetime. *Biochimica et Biophysica Acta (BBA) - Biomembranes* 735:95−103.

116. Harroun, T. A., W. T. Heller, T. M. Weiss, L. Yang, and H. W. Huang. 1999. Experimental Evidence for Hydrophobic Matching and Membrane-Mediated Interactions in Lipid Bilayers Containing Gramicidin. *Biophys. J.* 76:937−945.

117. Venturoli, M., B. Smit, and M. M. Sperotto. 2005. Simulation Studies of Protein-Induced Bilayer Deformations, and Lipid-Induced Protein Tilting, on a Mesoscopic Model for Lipid Bilayers with Embedded Proteins. *Biophys. J.* 88:1778−1798.

118. Evans, E. A., and R. M. Hochmuth. 1978. Mechano-chemical properties of membranes. In Curr. Top. Membr. Kleinzeller, and Bronner, editors. Academic Press, New York. 1−64.

119. Pandit, S. A., S. Vasudevan, S. W. Chiu, R. Jay Mashl, E. Jakobsson, and H. L. Scott. 2004. Sphingomyelin-Cholesterol Domains in Phospholipid Membranes: Atomistic Simulation. *Biophys. J.* 87:1092−1100.

120. Barber, C. B., D. P. Dobkin, and H. Huhdanpaa. 1996. The quickhull algorithm for convex hulls. *ACM Trans. Math. Softw.* 22:469−483.

121. Ku erka, N., Y. Liu, N. Chu, H. I. Petrache, S. Tristram-Nagle, and J. F. Nagle. 2005. Structure of Fully Hydrated Fluid Phase DMPC and DLPC Lipid Bilayers Using X-Ray Scattering from Oriented Multilamellar Arrays and from Unilamellar Vesicles. *Biophys. J.* 88:2626−2637.

122. Kučerka, N., S. Tristram-Nagle, and J. Nagle. 2006. Structure of Fully Hydrated Fluid Phase Lipid Bilayers with Monounsaturated Chains. *J. Membr. Biol.* 208:193−202.

123. Fattal, D. R., and A. Ben-Shaul. 1993. A molecular model for lipid-protein interaction in membranes: the role of hydrophobic mismatch. *Biophys. J.* 65:1795−1809.

124. Feller, S. E., and R. W. Pastor. 1999. Constant surface tension simulations of lipid bilayers: The sensitivity of surface areas and compressibilities. *J. Chem. Phys.* 111:1281−1287.

125. Rawicz, W., K. C. Olbrich, T. McIntosh, D. Needham, and E. Evans. 2000. Effect of Chain Length and Unsaturation on Elasticity of Lipid Bilayers. *Biophys. J.* 79:328−339.

126. Perly, B., I. C. P. Smith, and H. C. Jarrell. 1985. Acyl chain dynamics of phosphatidylethanolamines containing oleic acid and dihydrosterculic acid: deuteron NMR relaxation studies. *Biochemistry* 24:4659−4665.

127. Douliez, J. P., A. Léonard, and E. J. Dufourc. 1995. Restatement of order parameters in biomembranes: calculation of C-C bond order parameters from C-D quadrupolar splittings. *Biophys. J.* 68:1727−1739.

128. Im, W., and B. Roux. 2002. Ions and Counterions in a Biological Channel: A Molecular Dynamics Simulation of OmpF Porin from Escherichia coli in an Explicit Membrane with 1 M KCl Aqueous Salt Solution. *J. Mol. Biol.* 319:1177−1197.

129. Rui, H., K. I. Lee, R. W. Pastor, and W. Im. 2011. Molecular Dynamics Studies of Ion Permeation in VDAC. *Biophys. J.* 100:602−610.

Appendices

Appendix A

A List of Publications

1. "Automated Builder and Database of Protein/Membrane Complexes for Molecular Dynamics Simulations" S. Jo, T. Kim, and W. Im, *PLos ONE* 2(9):e880 (**2007**)
2. "CHARMM-GUI: A Web-based Graphical User Interface for CHARMM" S. Jo, T. Kim, V.G. Lyer, and W. Im, *J. Comput. Chem.* 29, 1859-1865 (**2008**)
3. "Molecular Dynamics Studies on Structure and Dynamics of Phospholamban Monomer and Pentamer in Membrane" T. Kim, J. Lee, and W. Im, *Proteins* 76, 86-98 (**2009**)
4. "Novel Free Energy Calculations to Explore Mechanisms and Energetics of Membrane Protein Structure and Function" W. Im, J. Lee, T. Kim, and H. Rui, *J. Comput. Chem.* 30, 1622-1633 (**2009**)
5. "Revisiting Hydrophobic Mismatch with Free Energy Simulation Studies of Transmembrane Helix Tilt and Rotation" T. Kim and W. Im, *Biophys. J.* 99, 175-183 (**2010**)
6. "Solid-State NMR Ensemble Dynamics as a Mediator between Experiment and Simulation" T. Kim, S. Jo, and W. Im, *Biophys. J.* 100, 2822-2928 (**2011**)

7. "An Ensemble Dynamics Approach to Decipher Solid-State NMR Observables of Membrane Proteins" W. Im, S. Jo, and T. Kim, *Biochimica et Biophysica Acta (BBA)-Biomembranes*, in press (**2011**)
8. "Influence of Hydrophobic Mismatch on Structures and Dynamics of Gramicidin A and Lipid Bilayers" T. Kim, P.M. Morris, K.I. Lee, R.W. Pastor, O.S. Andersen, and W. Im, *submitted*
9. "Critical Assessment of Membrane Deformation Continuum Elastic Models" K.I. Lee, T. Kim, R.W. Pastor, O.S. Andersen, and W. Im, *in preparation*
10. "Transmembrane Helix Assembly with Window Exchange Umbrella Sampling Molecular Dynamics" S. Park, T. Kim, and W. Im, *in preparation*
11. "Solid-state NMR Ensemble Dynamics of GWALP23 in DMPC bilayer" T. Kim, R.E. Koeppe II, and W. Im, *in preparation*

Appendix B

License Terms and Conditions

ELSEVIER LICENSE
TERMS AND CONDITIONS

Oct 17, 2011

This is a License Agreement between Taehoon Kim ("You") and Elsevier ("Elsevier") provided by Copyright Clearance Center ("CCC"). The license consists of your order details, the terms and conditions provided by Elsevier, and the payment terms and conditions.

All payments must be made in full to CCC. For payment instructions, please see information listed at the bottom of this form.

Supplier	Elsevier Limited The Boulevard,Langford Lane Kidlington,Oxford,OX5 1GB,UK
Registered Company Number	1982084
Customer name	Taehoon Kim
Customer address	2030 Becker Drive Room 260E Lawrence, KS 66045
License number	2757681293725
License date	Sep 28, 2011
Licensed content publisher	Elsevier
Licensed content publication	Biophysical Journal
Licensed content title	Revisiting Hydrophobic Mismatch with Free Energy Simulation Studies of Transmembrane Helix Tilt and Rotation
Licensed content author	Taehoon Kim,Wonpil Im
Licensed content date	7 July 2010
Licensed content volume number	99
Licensed content issue number	1
Number of pages	9
Start Page	175
End Page	183
Type of Use	reuse in a thesis/dissertation
Portion	full article
Format	both print and electronic
Are you the author of this Elsevier article?	Yes
Will you be translating?	No
Order reference number	
Title of your thesis/dissertation	The Influence of Hydrophobic Mismatch on Structure and Dynamics of Transmembrane Helices and Lipid Bilayers
Expected completion date	Oct 2011
Estimated size (number of pages)	200
Elsevier VAT number	GB 494 6272 12

Permissions price	0.00 USD
VAT/Local Sales Tax	0.00 USD / GBP
Total	**0.00 USD**

Terms and Conditions

INTRODUCTION

1. The publisher for this copyrighted material is Elsevier. By clicking "accept" in connection with completing this licensing transaction, you agree that the following terms and conditions apply to this transaction (along with the Billing and Payment terms and conditions established by Copyright Clearance Center, Inc. ("CCC"), at the time that you opened your Rightslink account and that are available at any time at http://myaccount.copyright.com).

GENERAL TERMS

2. Elsevier hereby grants you permission to reproduce the aforementioned material subject to the terms and conditions indicated.
3. Acknowledgement: If any part of the material to be used (for example, figures) has appeared in our publication with credit or acknowledgement to another source, permission must also be sought from that source. If such permission is not obtained then that material may not be included in your publication/copies. Suitable acknowledgement to the source must be made, either as a footnote or in a reference list at the end of your publication, as follows:
"Reprinted from Publication title, Vol /edition number, Author(s), Title of article / title of chapter, Pages No., Copyright (Year), with permission from Elsevier [OR APPLICABLE SOCIETY COPYRIGHT OWNER]." Also Lancet special credit - "Reprinted from The Lancet, Vol. number, Author(s), Title of article, Pages No., Copyright (Year), with permission from Elsevier."
4. Reproduction of this material is confined to the purpose and/or media for which permission is hereby given.
5. Altering/Modifying Material: Not Permitted. However figures and illustrations may be altered/adapted minimally to serve your work. Any other abbreviations, additions, deletions and/or any other alterations shall be made only with prior written authorization of Elsevier Ltd. (Please contact Elsevier at permissions@elsevier.com)
6. If the permission fee for the requested use of our material is waived in this instance, please be advised that your future requests for Elsevier materials may attract a fee.
7. Reservation of Rights: Publisher reserves all rights not specifically granted in the combination of (i) the license details provided by you and accepted in the course of this licensing transaction, (ii) these terms and conditions and (iii) CCC's Billing and Payment terms and conditions.
8. License Contingent Upon Payment: While you may exercise the rights licensed immediately upon issuance of the license at the end of the licensing process for the transaction, provided that you have disclosed complete and accurate details of your proposed use, no license is finally effective unless and until full payment is received from you (either by publisher or by CCC) as provided in CCC's Billing and Payment terms and conditions. If full payment is not received on a timely basis, then any license preliminarily granted shall be deemed automatically revoked and shall be void as if never granted. Further, in the event that you breach any of these terms and conditions or any of CCC's Billing and Payment terms and conditions, the license is automatically revoked and shall be void as if never granted. Use of materials as described in a revoked license, as well as any use of the materials beyond the scope of an unrevoked license, may constitute copyright infringement and publisher reserves the right to take any and all action to protect its copyright in the materials.
9. Warranties: Publisher makes no representations or warranties with respect to the licensed material.
10. Indemnity: You hereby indemnify and agree to hold harmless publisher and CCC, and their respective officers, directors, employees and agents, from and against any and all claims arising out of your use of the licensed material other than as specifically authorized pursuant to this license.
11. No Transfer of License: This license is personal to you and may not be sublicensed, assigned, or transferred by you to any other person without publisher's written permission.
12. No Amendment Except in Writing: This license may not be amended except in a writing signed by both parties (or, in the case of publisher, by CCC on publisher's behalf).
13. Objection to Contrary Terms: Publisher hereby objects to any terms contained in any purchase order, acknowledgment, check endorsement or other writing prepared by you, which terms are inconsistent with these terms and conditions or CCC's Billing and Payment terms and conditions. These terms and conditions, together with CCC's Billing and Payment terms and conditions (which are incorporated herein), comprise the entire agreement between you and publisher (and CCC) concerning this licensing transaction. In the event of any conflict between your obligations established by these terms and conditions and those established by CCC's Billing and Payment terms and conditions, these terms and conditions shall control.
14. Revocation: Elsevier or Copyright Clearance Center may deny the permissions described in this License at their sole discretion, for any reason or no reason, with a full refund payable to you. Notice of such denial will be made using the contact information provided by you. Failure to receive such notice will not alter or invalidate the denial. In no event will Elsevier or Copyright Clearance Center be responsible or liable for any costs, expenses or damage incurred by you as a result of a denial of your permission request, other than a refund of the amount(s) paid by you to Elsevier and/or Copyright Clearance Center for denied permissions.

LIMITED LICENSE

The following terms and conditions apply only to specific license types:
15. **Translation**: This permission is granted for non-exclusive world **English** rights only unless your license was granted for translation rights. If you licensed translation rights you may only translate this content into the languages you requested. A professional translator must perform all translations and reproduce the content word for word preserving the integrity of the article. If this license is to re-use 1 or 2 figures then permission is granted for non-exclusive world rights in all languages.
16. **Website**: The following terms and conditions apply to electronic reserve and author websites:
Electronic reserve: If licensed material is to be posted to website, the web site is to be password-protected and made available only to bona fide students registered on a relevant course if:
This license was made in connection with a course,
This permission is granted for 1 year only. You may obtain a license for future website posting,
All content posted to the web site must maintain the copyright information line on the bottom of each image,
A hyper-text must be included to the Homepage of the journal from which you are licensing at http://www.sciencedirect.com /science/journal/xxxxx or the Elsevier homepage for books at http://www.elsevier.com , and
Central Storage: This license does not include permission for a scanned version of the material to be stored in a central repository such as that provided by Heron/XanEdu.
17. **Author website** for journals with the following additional clauses:
All content posted to the web site must maintain the copyright information line on the bottom of each image, and
he permission granted is limited to the personal version of your paper. You are not allowed to download and post the published electronic version of your article (whether PDF or HTML, proof or final version), nor may you scan the printed edition to create an electronic version,
A hyper-text must be included to the Homepage of the journal from which you are licensing at http://www.sciencedirect.com /science/journal/xxxxx , As part of our normal production process, you will receive an e-mail notice when your article appears on Elsevier's online service ScienceDirect (www.sciencedirect.com). That e-mail will include the article's Digital Object Identifier (DOI). This number provides the electronic link to the published article and should be included in the posting of your personal version. We ask that you wait until you receive this e-mail and have the DOI to do any posting.
Central Storage: This license does not include permission for a scanned version of the material to be stored in a central repository such as that provided by Heron/XanEdu.
18. **Author website** for books with the following additional clauses:
Authors are permitted to place a brief summary of their work online only.
A hyper-text must be included to the Elsevier homepage at http://www.elsevier.com
All content posted to the web site must maintain the copyright information line on the bottom of each image
You are not allowed to download and post the published electronic version of your chapter, nor may you scan the printed edition to create an electronic version.
Central Storage: This license does not include permission for a scanned version of the material to be stored in a central repository such as that provided by Heron/XanEdu.

19. **Website** (regular and for author): A hyper-text must be included to the Homepage of the journal from which you are licensing at http://www.sciencedirect.com/science/journal/xxxxx. or for books to the Elsevier homepage at http://www.elsevier.com
20. **Thesis/Dissertation**: If your license is for use in a thesis/dissertation your thesis may be submitted to your institution in either print or electronic form. Should your thesis be published commercially, please reapply for permission. These requirements include permission for the Library and Archives of Canada to supply single copies, on demand, of the complete thesis and include permission for UMI to supply single copies, on demand, of the complete thesis. Should your thesis be published commercially, please reapply for permission.
21. **Other Conditions**:

v1.6

If you would like to pay for this license now, please remit this license along with your payment made payable to "COPYRIGHT CLEARANCE CENTER" otherwise you will be invoiced within 48 hours of the license date. Payment should be in the form of a check or money order referencing your account number and this invoice number RLNK0.
Once you receive your invoice for this order, you may pay your invoice by credit card. Please follow instructions provided at that time.

Make Payment To:
Copyright Clearance Center
Dept 001
P.O. Box 843006
Boston, MA 02284-3006

For suggestions or comments regarding this order, contact RightsLink Customer Support: customercare@copyright.com or +1-877-622-5543 (toll free in the US) or +1-978-646-2777.

Gratis licenses (referencing $0 in the Total field) are free. Please retain this printable license for your reference. No payment is required.

ELSEVIER LICENSE
TERMS AND CONDITIONS

Oct 17, 2011

This is a License Agreement between Taehoon Kim ("You") and Elsevier ("Elsevier") provided by Copyright Clearance Center ("CCC"). The license consists of your order details, the terms and conditions provided by Elsevier, and the payment terms and conditions.

All payments must be made in full to CCC. For payment instructions, please see information listed at the bottom of this form.

Supplier	Elsevier Limited The Boulevard,Langford Lane Kidlington,Oxford,OX5 1GB,UK
Registered Company Number	1982084
Customer name	Taehoon Kim
Customer address	2030 Becker Drive Room 260E Lawrence, KS 66045
License number	2757681412100
License date	Sep 28, 2011
Licensed content publisher	Elsevier
Licensed content publication	Biophysical Journal
Licensed content title	Solid-State NMR Ensemble Dynamics as a Mediator between Experiment and Simulation
Licensed content author	Taehoon Kim,Sunhwan Jo,Wonpil Im
Licensed content date	22 June 2011
Licensed content volume number	100
Licensed content issue number	12
Number of pages	7
Start Page	2922
End Page	2928
Type of Use	reuse in a thesis/dissertation
Intended publisher of new work	other
Portion	full article
Format	both print and electronic
Are you the author of this Elsevier article?	Yes
Will you be translating?	No
Order reference number	
Title of your thesis/dissertation	The Influence of Hydrophobic Mismatch on Structure and Dynamics of Transmembrane Helices and Lipid Bilayers
Expected completion date	Oct 2011
Estimated size (number of pages)	200

Elsevier VAT number	GB 494 6272 12
Permissions price	0.00 USD
VAT/Local Sales Tax	0.00 USD / GBP
Total	**0.00 USD**
Terms and Conditions	

INTRODUCTION

1. The publisher for this copyrighted material is Elsevier. By clicking "accept" in connection with completing this licensing transaction, you agree that the following terms and conditions apply to this transaction (along with the Billing and Payment terms and conditions established by Copyright Clearance Center, Inc. ("CCC"), at the time that you opened your Rightslink account and that are available at any time at http://myaccount.copyright.com).

GENERAL TERMS

2. Elsevier hereby grants you permission to reproduce the aforementioned material subject to the terms and conditions indicated.
3. Acknowledgement: If any part of the material to be used (for example, figures) has appeared in our publication with credit or acknowledgement to another source, permission must also be sought from that source. If such permission is not obtained then that material may not be included in your publication/copies. Suitable acknowledgement to the source must be made, either as a footnote or in a reference list at the end of your publication, as follows:
"Reprinted from Publication title, Vol /edition number, Author(s), Title of article / title of chapter, Pages No., Copyright (Year), with permission from Elsevier [OR APPLICABLE SOCIETY COPYRIGHT OWNER]." Also Lancet special credit - "Reprinted from The Lancet, Vol. number, Author(s), Title of article, Pages No., Copyright (Year), with permission from Elsevier."
4. Reproduction of this material is confined to the purpose and/or media for which permission is hereby given.
5. Altering/Modifying Material: Not Permitted. However figures and illustrations may be altered/adapted minimally to serve your work. Any other abbreviations, additions, deletions and/or any other alterations shall be made only with prior written authorization of Elsevier Ltd. (Please contact Elsevier at permissions@elsevier.com)
6. If the permission fee for the requested use of our material is waived in this instance, please be advised that your future requests for Elsevier materials may attract a fee.
7. Reservation of Rights: Publisher reserves all rights not specifically granted in the combination of (i) the license details provided by you and accepted in the course of this licensing transaction, (ii) these terms and conditions and (iii) CCC's Billing and Payment terms and conditions.
8. License Contingent Upon Payment: While you may exercise the rights licensed immediately upon issuance of the license at the end of the licensing process for the transaction, provided that you have disclosed complete and accurate details of your proposed use, no license is finally effective unless and until full payment is received from you (either by publisher or by CCC) as provided in CCC's Billing and Payment terms and conditions. If full payment is not received on a timely basis, then any license preliminarily granted shall be deemed automatically revoked and shall be void as if never granted. Further, in the event that you breach any of these terms and conditions or any of CCC's Billing and Payment terms and conditions, the license is automatically revoked and shall be void as if never granted. Use of materials as described in a revoked license, as well as any use of the materials beyond the scope of an unrevoked license, may constitute copyright infringement and publisher reserves the right to take any and all action to protect its copyright in the materials.
9. Warranties: Publisher makes no representations or warranties with respect to the licensed material.
10. Indemnity: You hereby indemnify and agree to hold harmless publisher and CCC, and their respective officers, directors, employees and agents, from and against any and all claims arising out of your use of the licensed material other than as specifically authorized pursuant to this license.
11. No Transfer of License: This license is personal to you and may not be sublicensed, assigned, or transferred by you to any other person without publisher's written permission.
12. No Amendment Except in Writing: This license may not be amended except in a writing signed by both parties (or, in the case of publisher, by CCC on publisher's behalf).
13. Objection to Contrary Terms: Publisher hereby objects to any terms contained in any purchase order, acknowledgment, check endorsement or other writing prepared by you, which terms are inconsistent with these terms and conditions or CCC's Billing and Payment terms and conditions. These terms and conditions, together with CCC's Billing and Payment terms and conditions (which are incorporated herein), comprise the entire agreement between you and publisher (and CCC) concerning this licensing transaction. In the event of any conflict between your obligations established by these terms and conditions and those established by CCC's Billing and Payment terms and conditions, these terms and conditions shall control.
14. Revocation: Elsevier or Copyright Clearance Center may deny the permissions described in this License at their sole discretion, for any reason or no reason, with a full refund payable to you. Notice of such denial will be made using the contact information provided by you. Failure to receive such notice will not alter or invalidate the denial. In no event will Elsevier or Copyright Clearance Center be responsible or liable for any costs, expenses or damage incurred by you as a result of a denial of your permission request, other than a refund of the amount(s) paid by you to Elsevier and/or Copyright Clearance Center for denied permissions.

LIMITED LICENSE

The following terms and conditions apply only to specific license types:

15. **Translation**: This permission is granted for non-exclusive world **English** rights only unless your license was granted for translation rights. If you licensed translation rights you may only translate this content into the languages you requested. A professional translator must perform all translations and reproduce the content word for word preserving the integrity of the article. If this license is to re-use 1 or 2 figures then permission is granted for non-exclusive world rights in all languages.

16. **Website**: The following terms and conditions apply to electronic reserve and author websites:

Electronic reserve: If licensed material is to be posted to website, the web site is to be password-protected and made available only to bona fide students registered on a relevant course if:

This license was made in connection with a course,

This permission is granted for 1 year only. You may obtain a license for future website posting,

All content posted to the web site must maintain the copyright information line on the bottom of each image,

A hyper-text must be included to the Homepage of the journal from which you are licensing at http://www.sciencedirect.com /science/journal/xxxxx or the Elsevier homepage for books at http://www.elsevier.com , and

Central Storage: This license does not include permission for a scanned version of the material to be stored in a central repository such as that provided by Heron/XanEdu.

17. **Author website** for journals with the following additional clauses:

All content posted to the web site must maintain the copyright information line on the bottom of each image, and

he permission granted is limited to the personal version of your paper. You are not allowed to download and post the published electronic version of your article (whether PDF or HTML, proof or final version), nor may you scan the printed edition to create an electronic version,

A hyper-text must be included to the Homepage of the journal from which you are licensing at http://www.sciencedirect.com /science/journal/xxxxx , As part of our normal production process, you will receive an e-mail notice when your article appears on Elsevier's online service ScienceDirect (www.sciencedirect.com). That e-mail will include the article's Digital Object Identifier (DOI). This number provides the electronic link to the published article and should be included in the posting of your personal version. We ask that you wait until you receive this e-mail and have the DOI to do any posting.

Central Storage: This license does not include permission for a scanned version of the material to be stored in a central repository such as that provided by Heron/XanEdu.

18. **Author website** for books with the following additional clauses:

Authors are permitted to place a brief summary of their work online only.

A hyper-text must be included to the Elsevier homepage at http://www.elsevier.com

All content posted to the web site must maintain the copyright information line on the bottom of each image

You are not allowed to download and post the published electronic version of your chapter, nor may you scan the printed edition to create an electronic version.

Central Storage: This license does not include permission for a scanned version of the material to be stored in a central repository such as that provided by Heron/XanEdu.

19. **Website** (regular and for author): A hyper-text must be included to the Homepage of the journal from which you are licensing at http://www.sciencedirect.com/science/journal/xxxxx. or for books to the Elsevier homepage at http://www.elsevier.com

20. **Thesis/Dissertation**: If your license is for use in a thesis/dissertation your thesis may be submitted to your institution in either print or electronic form. Should your thesis be published commercially, please reapply for permission. These requirements include permission for the Library and Archives of Canada to supply single copies, on demand, of the complete thesis and include permission for UMI to supply single copies, on demand, of the complete thesis. Should your thesis be published commercially, please reapply for permission.

21. **Other Conditions**:

v1.6

If you would like to pay for this license now, please remit this license along with your payment made payable to "COPYRIGHT CLEARANCE CENTER" otherwise you will be invoiced within 48 hours of the license date. Payment should be in the form of a check or money order referencing your account number and this invoice number RLNK0.
Once you receive your invoice for this order, you may pay your invoice by credit card. Please follow instructions provided at that time.

Make Payment To:
Copyright Clearance Center
Dept 001
P.O. Box 843006

Boston, MA 02284-3006

For suggestions or comments regarding this order, contact RightsLink Customer Support: customercare@copyright.com or +1-877-622-5543 (toll free in the US) or +1-978-646-2777.

Gratis licenses (referencing $0 in the Total field) are free. Please retain this printable license for your reference. No payment is required.